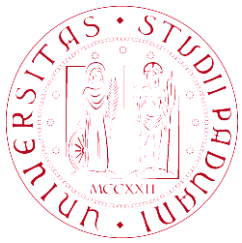

UNIVERSITÀ DEGLI STUDI DI PADOVA

DIPARTIMENTO DI INGEGNERIA INDUSTRIALE

SCUOLA DI DOTTORATO DI RICERCA IN INGEGNERIA INDUSTRIALE

INDIRIZZO: INGEGNERIA CHIMICA, DEI MATERIALI E MECCANICA

CICLO XXVIII

IDENTIFICATION AND IMPROVEMENT OF THE DYNAMIC PROPERTIES OF THE COMPONENTS OF TWO-WHEELED VEHICLES

Coordinatore d'indirizzo: Ch.mo Prof. Enrico Savio

Direttore della Scuola: Ch.mo Prof. Paolo Colombo

Supervisore: Ch.mo Prof. Alberto Doria

Dottorando: Luca Taraborrelli

Abstract

Single track vehicles dynamic is a very complex topic that involves many different branches of the scientific knowledge, such as vibration mechanics, stability and control, materials science and biomechanics. Although the first studies on the stability of a single track vehicle were carried out at the end of the XIX century, the technological progress that has improved the properties of the employed materials and the craving for better performances oblige the scientific world to an everlasting research activity, carried out both on whole vehicles and on single components.

This Ph. D. thesis summarizes the research activities carried out at the Motorcycle Dynamics Research Group of the University of Padova and describes the tested mechanical components, the testing equipments, the experimental data, the elaboration criteria and the final results obtained after a three years work.

The experimental methodologies employed in order to carry out the research activities are presented in the first chapter. Both the hardware and the software of each experimental bench will be described. In addition, the theoretical principles on which the testing rigs are based and the principles with which it processes the output of the measuring sensors will be illustrated.

Subsequent chapters shift the focus on the results obtained on the various analyzed components. The second chapter presents the results of the tests carried out on motorcycles frames , with or without engine; the third chapter describes the results of the measurements made on motorcycles swingarms; the fourth chapter describes the results of tests performed on motorcycle front forks; the fifth chapter presents the results of tests conducted on front and rear motorcycle and scooter tires; shifting the attention to another type of two-wheeled vehicle, the sixth chapter presents the results of the tests carried out on bicycles and bicycle components. Finally, the seventh chapter describes the results of measurements conducted on tires typically used for wheelchairs.

Sommario

La dinamica dei veicoli a due ruote è un campo di studio molto complesso poiché interessa numerosi ambiti del sapere scientifico, dalla meccanica delle vibrazioni al controllo dei sistemi, dalla biomeccanica all'ingegneria dei materiali. Nonostante i primi studi siano stati condotti già sul finire del XIX secolo, il progresso tecnologico che negli anni ha stravolto la natura dei materiali utilizzati e il desiderio di prestazioni sempre più "al limite" impongono una incessante attività di ricerca, condotta sia su veicoli interi che su loro singoli componenti.

Questa tesi di dottorato raccoglie le attività di ricerca condotte nel Motorcycle Dynamics Research Group dell'Università degli Studi di Padova, descrivendo i componenti meccanici analizzati, i banchi di misura, i dati sperimentali, i criteri di elaborazione e i risultati a cui si è arrivati in tre anni di lavoro.

Nel primo capitolo sono descritte tutte le metodologie sperimentali che sono state adottate nel condurre le attività di ricerca in laboratorio. Per ogni banco di misura, verrà fornita una descrizione dei componenti fisici e dei programmi informatici. Inoltre, verranno descritti i principi teorici alla base del funzionamento del banco e i principi con cui si elaborano i dati in uscita dai sensori di misura.

I successivi capitoli spostano l'attenzione sui risultati ottenuti sui vari componenti analizzati. Il secondo capitolo raccoglie i risultati dei test condotti su telai da motociclette, con e senza motore; il terzo capitolo descrive i risultati delle misurazioni effettuate su forcelloni di motociclette; il quarto capitolo descrive i risultati dei test condotti su forcelle anteriori da motocicletta; nel quinto capitolo sono presentati i risultati dei test condotti su pneumatici anteriori e posteriori di motocicletta e da scooter; spostando l'attenzione su un altro tipo di veicolo a due ruote, il sesto capitolo raccoglie i risultati dei test condotti su biciclette e su loro componenti. Per ultimo, il settimo capitoli descrive i risultati delle misure condotte su tipici pneumatici usati per sedie a rotelle.

Introduction

"As I rode, curve after curve, the engine pushed on almost as if it was a hammer strong enough to forge any type of steel with violent blows of metal on metal" [1]. As one would imagine from this quote by Professor Vittore Cossalter, the world of motorcyclism is rich of art and passion, and enthralls customers from every corner of the planet. For this reason, designers and manufacturers are never satisfied by the improvements achieved in order to fulfill the customers' wishes: some of them prefer to count on a fiery power guaranteed by engines with thousands of horse powers, some prefer to rely on other qualities, such as maneuverability, style and nimbleness, that highlight the beauty of the vehicle and exalt the rider technical abilities. From a scientific point of view, the craving for better performances in the motorsports world and the demand of some properties (such as safety, stability, comfort, cost, etc.) from ordinary customers oblige the industries and the universities to carry out an everlasting activity of research both on whole vehicles and on single components. This Ph. D. thesis summarizes the research activities carried out at the Motorcycle Dynamics Research Group (MDRG) of the University of Padova. It will describe the tested mechanical components, the testing equipments, the experimental data, the elaboration criteria and the final results obtained after a three years work.

The study of vehicle stability is one of the most important research topic in the field of single track vehicles and it is deeply investigated in the MDRG of the University of Padova. If, on one hand, the natural instabilities of two-wheeled vehicles can suggest an advantage in terms of maneuverability and quickness, on the other hand they can lead to dangerous circumstances. And, even if the study of stability has experienced much advancement over the last years, it still presents some phenomena that require further research and remains one of the most important aspects in the design of safe and powerful vehicles.

Early researchers and motorcycle designers discovered that the flexibility of a mechanical component plays an important role in motorcycle dynamics and may alter the stability properties of the vehicle. However, the optimal flexibility of a motorcycle remains nowadays an open research topic. An established method for flexibility measurement has still to be defined and manufacturers generally use different measurement approaches. Moreover, there are different measurement methods depending on the components that are tested.

As an example, it is well known that the flexibility of a motorcycle front fork can have a significant effect on motorcycle stability. Front forks properties are involved in ordinary operations of riding, such as braking and steering. In addition, some of the most common and dangerous modes of vibration that determine a motorcycle instability (wobble, weave) involve a vibration of the front fork. Also the chassis of a single-track vehicle is a very interesting structural element, because it determines the relative position between the two wheels and for this reason it has a deep influence on the dynamic stability of the vehicle: in the case of a motorcycle, the stability of the front wheel, which can be considered a castor with short trail, is influenced by the lateral compliance of the front fork and of the steering head of the frame; the stability of the rear wheel, which can be considered a castor with long trail, is influenced both by bending flexibility of the rear frame and by torsion deformability of the rear frame with respect to the steering head. Some studies [1] [2] highlighted that the compliances of these elements influence significantly the stability and in particular the weave and wobble modes [1]. These are the most important modes that affect the vehicle stability. Wobble consists mainly in oscillations of the front frame and has frequencies in the range 6-7 Hz. Weave is a fishtail-like motion of the whole vehicle with frequencies rising with speed, in this case up to 4Hz, and as usual is unstable at very low speeds (below 6-7 m/s) and weakly damped at high speed.

Another merit of the early studies on motorcycle stability has been the introduction of a lumped element approach in order to represent the critical compliances of the structural elements of a motorcycle [3]. This approach is still in use with advanced multibody codes [4]. Nevertheless, up to now very few scientific studies have been carried out to identify the parameters of the lumped elements that account for the stiffness and damping properties of two wheeled vehicles components.

The first specific research on this topic was carried out in 1983 [5], when the front and rear frames of a motorcycle were anchored to a stiff structure, static and dynamic forces were applied to the wheels in order to identify stiffness properties. The deformation of frames was represented by means of the twist axis, which was defined as the intersection between the symmetry plane of the motorcycle and the plane of the wheel in loaded condition. In 1986, another group of scientists investigated the effect of static properties and in particular torsion stiffness of motorcycle frames [6]. With reference to a framework of tubes (like some motorcycle chassis), they defined the twist axis as an axis along which no lateral displacement takes place when a torque is applied about it.

Recent experimental tests on motorcycle components compliance are reported in [7] (only chassis) e [8]. The latter paper employed the method of modal analysis for studying the vibrations of the whole motorcycle. Results have shown the existence of various out-of-plane modes of vibration in the range of frequency below 50 Hz. It is worth remembering that the static compliance is a combination of the modal compliances of various modes of vibration [9],[10].

One of the aims of this research has been the characterization of an experimental procedure that allows the measurement and the identification of some mechanical parameters of different motorcycle components and makes it possible to introduce those parameters in multibody models. In other words, the

original path explored by early researchers has been followed using the same scientific parameters (e.g. the twist axis), but the endeavor has been focused on the possibility of introducing the identified parameters in mathematical models that could offer some information about the vehicle stability.

An original definition of the twist axis is included in this thesis: in general, the twist axis of a single track vehicle component is a property that gives information about the deformability of the component and depends on its stiffness characteristics. Nevertheless, it has been measured and analyzed for two different vehicles (motorcycles and bicycles) and two different types of tests (static and dynamic), so that each type of analysis is described individually. Moreover, an interesting correlation between the twist axis and the Mozzi axis has been studied and properly described in a paragraph of Chapter 1. Chapters 2, 3 and 4 collect the results of the experimental tests carried out on three types of motorcycle components: frames, swing-arms and front forks respectively.

After the study of the properties of some motorcycle structural components, the attention has been focused on the dynamic properties of the tires. It is well known that static and dynamic properties of tires have a large influence on single-track vehicles stability. The first model for the study of the dynamics of a single-track vehicle was developed by Whipple and Carvallo in 1899 [11] and it included the rear and the front wheel (in addition to a rear frame and a front frame). The four rigid bodies were connected by means of kinematic joints and the disk wheels were in rolling contact with the road without any slip. This model had three degrees of freedom and it was able to predict only the capsize and weave modes. Further research carried out with the aid of computer simulation showed that a more detailed tire model was needed to study high speed dynamics and in particular the wobble mode [12]. Several researchers [1],[12] proved that, in order to study wobble stability, both slip phenomena in the contact patch and lateral compliance of the tire's carcass have to be taken into account.

It is well known that the tire is a dynamic system which does not respond instantaneously to variation in the side-slip angle but shows a transient. Döhring was the first to introduce in 1956 a phase lag between the instantaneous inclination of the wheel (roll and yaw angles) and the generated tire forces. The merit of the first analysis of motorcycle stability is owned to Sharp [12]. His paper is a milestone in the history of motorcycle dynamics. The equations of motion are derived with a Lagrange method and a first order differential equation takes into account the abovementioned phase lag of the tire forces. The analysis of the eigenvalues and eigenvectors of the system allows to identify three typical vibration modes of the out-of-plane of the vehicle: capsize (not oscillating and stable up to about 10 m/s), wobble (oscillating with a frequency of about 6-10 Hz, not depending on speed) and weave (oscillating and stable over 7 m/s, with frequencies increasing from 0 Hz to 3-4 depending on speed).

For modest frequencies (below 5÷10 Hz in motorcycle tires), during the transient the tire can be modelled as a first order system characterized by a time lag [13]. When the vehicle travels with constant forward speed V, the time lag corresponds to a travelled distance which is named relaxation length σ. Tire forces and torques due to camber are characterized by a significant non-lagging part [14]. The dynamic properties of tires are generally expressed in terms of relaxation length. Relaxation length is often studied by means of rigid ring models [14], [15], in which the belt of the tire is modeled as a rigid ring elastically connected to the rim and the contact patch is connected to the belt by means of residual springs. Actually these models are able to take into account the lateral and the diametrical modes of vibration of the rigid belt with respect to the rim and to represent in a simplified way the modes with belt deformation by means of the residual stiffness. In the literature, there are few data about the stiffness and damping properties of the

carcass of the tire, some rules of thumb are given in [14]. This lack of information is even worse when tires for single-track vehicles are studied.

The research activities carried out on motorcycle tires, collected in Chapter 6, are divided in two sections: the first section shows the relaxation lengths measured by means of experimental tests performed on the rotating disk machine of MDRG; the second section focuses on the characterization of a method that allows to predict the relaxation length according to a first order model of the tire. The experimental equipment and the identification methods are presented in Chapter 1.

Some research has been focused also on bicycles and bicycle components. The study of bicycles and bicycle frames has been focused on the analysis of their dynamic properties, with a specific interest in their modes of vibration: in fact, the vibrations occurring in a bicycle can affect not only comfort, but also stability. For this reason, research in the field of bicycles dynamics, which started in the last years of 19th century, has principally addressed to the problems of auto-stabilization and cyclist control. In recent years the interest in this field is increased owing to the development of advanced materials, electrical bicycles, ecological issues and owing to the possibilities of analysis and simulation offered by numerical methods.

Stability of bicycles is often studied starting from the benchmark model developed in 1899 by Whipple and Carvallo, mentioned before for motorcycles. In recent years significant improvements have been made to the basic Carvallo and Whipple bicycle model to overcome its limits and to allow the possibility of simulation of modern bicycles. Actually, in bicycles the mass of the cyclist is much larger than the mass of the vehicle and the rider's body is not a rigid extension of the rear frame, but it vibrates if vehicle oscillations occur, even without any control of the cyclist. Schwab et alii [16] have added two different cyclist models without introducing further degrees of freedom; their results show that the motion of the cyclist's body can alter the stability characteristics especially in the case of cyclist with upright body and flexed arms.

Other improvements are due to the introduction of tire mechanics [17][18] and the modeling of frame and fork flexibility [19]. Actually, mechanical structural properties of bicycle and bicycles components have been studied mostly in relation with comfort properties [20] [21] and vibration analysis has been focused on in-plane modes. Only in recent years specific results dealing with out-of-plane modes have been presented [22]. When a bicycle is running on the road, there is an interaction between the typical bicycle modes (capsize, weave and wobble) and the structural modes of frame and fork, hence a deep knowledge of the modal properties of the bicycle's structural elements is the first step for a realistic description of flexibility properties in simulation models.

The analysis of bicycle forks has been focused on the identification of their static and dynamic properties and on the study of the effect of front fork compliance on the stability of bicycles. Mechanical flexibility is usually taken into account by introducing lumped stiffness and damping elements that represent in a simplified way the properties of (frames and) front forks. However, the manner in which the positions and values of the lumped stiffness elements is identified is not addressed in literature.

In the framework of this research, the benchmark bicycle model has been improved to take into account either bending compliance or torsion compliance of front fork. Only the front fork model has been modified introducing additional generalized coordinates and lumped elements that represent the relevant stiffness and damping properties. This approach, which holds true in the framework of linear analysis, makes it possible to separate the influence of front fork compliance from other effects, like side-slip and relaxation

length of tires. A series of experimental tests has been carried out with the modal analysis approach. Successively, a specific method has been developed for evaluating the stiffness and damping properties from the bending and torsion modes of the forks. Finally, the identified stiffness and damping parameters have been implemented in the simulation codes and some numerical simulations have been carried out.

The last chapter of the thesis is focused on the research activities carried out on wheelchairs and wheelchair tires. Two wheelchair tires have been tested on the same testing machine usually employed for motorcycle and bicycle tires, the measurements aiming to obtain a characterization of the steady-state properties of the tires. The interest in the research is due to the fact that very few studies have been carried out on wheelchair tires. The two tires have been tested for their nominal inflation pressure (2 bar) and for a reference load of 400 N. The effects of variations in inflation pressure, vertical load and traveling speed have been studied as well.

Finally, a model of a wheelchair based on the dynamic of a four-wheeled vehicle has been developed. The equations of the model have been implemented in a MATLAB code and some numerical simulations of two typical wheelchair maneuvers (steady-turning and slalom) have been carried out. The values of stiffness an rolling resistance measured by means of laboratory tests have been used as realistic parameters in the wheelchair model. An analysis of the effect of a variation of these parameters on the dynamics of the vehicle has been carried out in MATLAB as well.

Chapter 1 – Experimental equipment and methods

According to the experimental method illustrated in the XVII century by the Italian physicist and astronomer Galileo Galilei, on which modern science is based, experimental activities play a fundamental role in the development of a scientific theory. Every scientific hypothesis must be deeply checked by means of experimental tests and also an engineering study should be accompanied by the collection of laboratory data. Considerable attention has to be paid in the design of the experimental rigs and in the accuracy of data processing in order to acquire consistent data and obtain realistic results. The measurement of the properties of similar objects (two frames, two front forks, etc.) by means of experimental tests can be useful for manufacturers and designers for making comparisons and comprehend which element plays the most important role from the point of view of the component's quality and efficiency.

Experimental data have been collected for every tested motorcycle and bicycle component, so that many experimental tests have been carried out. Chapter 1 aims to take into account those issues. First, it describes the experimental rigs and the techniques that have been used for carrying out the experimental tests. Moreover, it illustrates the elaboration criteria that have been employed for the identification of the static and dynamic properties of two-wheeled vehicle components.

In the framework of this research many different types of tests (modal analysis, static tests, etc.) have been performed, the aim of the measurements has been the identification of a models that could describe the static and dynamic mechanical properties of the tested component. From modal analysis, a specific modal model is identified, the model being based on the dynamic characteristics of the system; from static tests, it is possible to acquire interesting information on the static properties of the system that can be used for developing a static model. It is worth remembering that from a theoretical point of view it is possible to switch from one model to another by means of mathematic equations, which makes it possible to make comparisons between the models and obtain the characteristics of a model from the characteristics of another one.

In general, the dynamic properties of a system with N degrees of freedom may be described by three different types of complete models: the spatial model, the modal model and the response model. In the first case, the system dynamic characteristics are expressed in terms of its mass, stiffness and damping properties, described by the NxN mass, stiffness and damping matrices, respectively. The spatial model given by [M], [K] and [D] (or [C]) leads to an eigenproblem which, having been solved, yield the modal model constituted by the modal properties (N natural frequencies, N modal damping values and N mode shapes vectors). The modal properties are contained in matrices $[\omega_r^2]$ and $[\phi]$.

If we take the modal model and refer to the orthogonal properties of the modal matrix (in case of hysteretic damping), we have:

$$\begin{aligned} &[\Phi]^T[M][\Phi]=[I] \\ &[\Phi]^T\left[[K]+i[D]\right][\Phi]=[\lambda_r^2]=[\omega_r^2(1+i\eta_r)] \end{aligned} \qquad (1)$$

and therefore:

$$\begin{aligned} &[\Phi]^T[\Phi]^{-1}=[M] \\ &[\Phi]^T[\omega_r^2(1+i\eta_r)][\Phi]^{-1}=[K]+i[D] \end{aligned} \qquad (2)$$

Equations (1) and (2) show that, in principle, it is possible to obtain a spatial model from the knowledge of the modal model. This may be an important conclusion if one thinks that it is the modal model that is initially derived from the experimental FRF data. Furthermore, it is possible to show that the modal model yields the response model. Thus, starting from the spatial model, we have ended with a response model after going through an intermediate modal model. This sequence in commonly performed when the starting point is a theoretical analysis. However, if a system is too complex and cannot be modelled analytically, the starting point is the experimental measurement of the system frequency response functions, that is, the system is described by means of a response model. The modal model can be easily derived with specific algorithms for the modal identification. Finally, one may apply equations (1) and (2) and obtain the spatial model. Figure 1 shows the above discussed models interrelation, based on the undamped case.

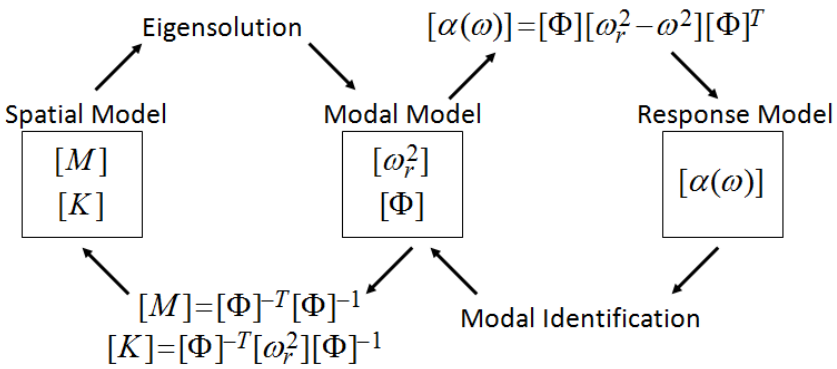

Figure 1 Dynamic models interrelation (case with no damping)

Up to now, complete models of the system have been assumed, that is all the mass, stiffness and damping properties of the spatial model are known, all the elements in the eigenvectors are known, etc. However, this approach is valid only from a theoretical point of view. The knowledge that any real system has an infinite number of DOFs is sufficient for understanding the practical impossibility of the approach.

Moreover, even if a system with a finite number of DOFs is taken into account, there are further forms of incompleteness due to the experimental techniques. The frequency range of an experimental modal analysis, for example, is limited, and therefore at least the high frequency modes will be omitted.

For example, the case of a beam discretised as a 6 DOFs model (3 rotations and 3 translations) is taken into account, and we want to identify the response model of the beam. The receptance matrix is of order 6x6 and includes both translation and rotation coordinates. Yet, the measurement of rotational responses is a very difficult experimental task and torque excitation is almost impossible with ordinary experimental means. The model is therefore limited to include only the translation coordinates and the resulting reduced FRF matrix will be of order 3x3. Even if we ceased to be able to describe all the initial DOFs of the system, we did not alter the basic system which still has 6 DOFs. In a response model, reducing the coordinates of interest from N to p is a simple operation of elimination of the N-p rows and columns of the frequency response matrix.

Similar approaches are used for the cases of modal model and spatial model. Usually, in order to take into account the limited number of modes that can be identified, in the response equation of a modal model a complex, residual extra term that accounts for the contribution of the out-of-range modes is introduced. In the case of a spatial model, reducing the number of coordinates entails reducing the mass, stiffness and damping matrices. Such a reduction cannot be performed by simply eliminating rows and columns, but one must use specific techniques for redistribution of the system mass, stiffness and damping properties amongst the retained coordinates. It is better to speak in terms of matrix condensation instead of matrix reduction.

1.1 The Motostiffmeter

The *Motostiffmeter* equipment was mostly designed and assembled in the laboratory of Mechanical Engineering of the University of Padova according to the research project of Eng. Mauro Tognazzo as one of his Ph. D. research activities [23]. The experimental bench was developed in order to identify the structural stiffness properties of typical motorcycle components in static and dynamic conditions and is shown in Figure 2. The rig consists of a very stiff column, a servo-hydraulic actuator and a system of sensors. The column is equipped with two stiff metal jaws that make it possible to lock the tested component and eliminate some degrees of freedom according to the aim of the measurement.

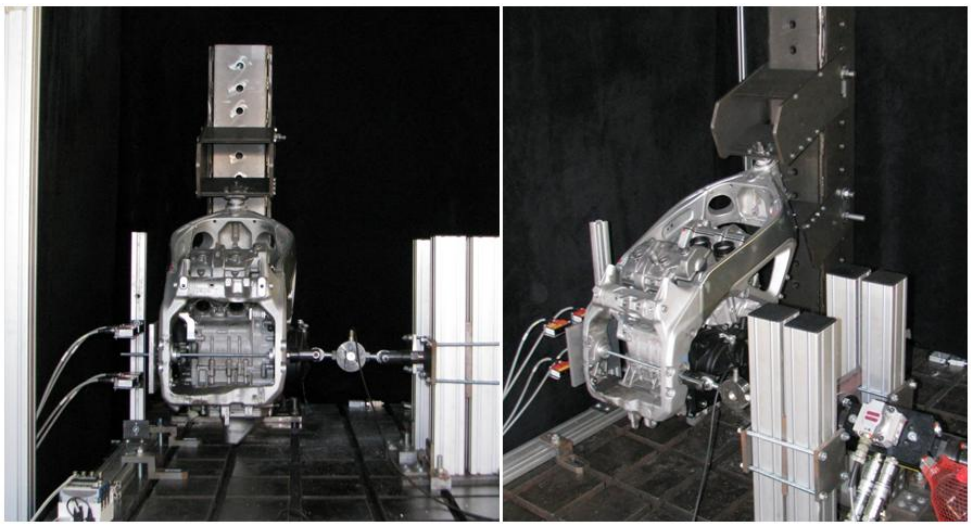

Figure 2 The *Motostiffmeter*

The actuator is powered by a hydraulic unit and can apply a static load up to 5000 N. In addition, the actuator can be controlled also in frequency in order to apply a dynamic excitation up to 45 Hz, but the amplitude of vibration decreases logarithmically as the excitation frequency increases. The system of sensors includes a load cell and three laser sensors. The load cell is aligned with the actuator axis and is employed for the measurement of the force applied by the actuator. The cell is designed for tension and compression tests with maximum load of ±200 kg and is mounted with two ball-and-socket joints in order to apply the load in one direction only. The laser sensors are employed for measuring the deformation of the component under test. Actually, the sensors are mounted on the platform of the testing rig in order to measure the displacement of a small metal plate that is stiffly attached to the loaded end of the tested component. The laser sensors have a measurement range of 20 mm and a max resolution of 4 µm.

1.2 Identification of the static twist axis

The twist axis of a rigid body is a complex but very useful parameter for characterizing the static mechanical properties of the body and many researchers have proposed a specific definition of this axis [3],[6]. It encloses important information about the torsion and the bending stiffness of the body and can be used for developing a lumped element model of the body in a multi-body code. In general, when an almost two-dimensional structure (e.g. a motorcycle frame) has a polygonal shape with an end locked to a very stiff constrain and an end loaded by a static force, the deformation of the loaded end (e.g. the swing arm pivot) can be studied taking into account the motion of a reference plate attached to the loaded end. According to the nomenclature adopted in this thesis, *the twist axis is identified by the intersection between the plane defined by the reference plate in unloaded condition and the plane defined by the reference plate in loaded condition*.

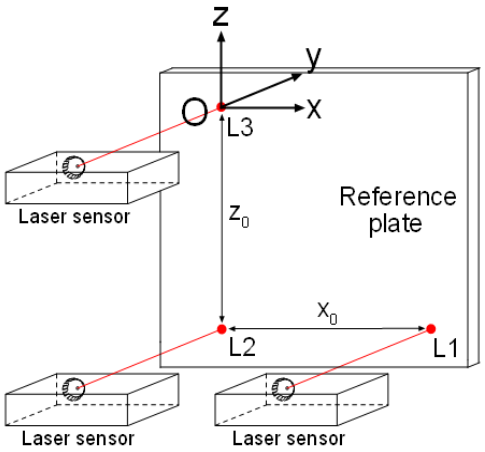

Figure 3 The arrangement of the laser sensors on the reference plate

In order to identify the twist axis, the component under testing is locked on one end to the stiff column of the *Motostiffmeter* (Figure 2). The opposite end is loaded by the actuator while some laser sensors monitor the displacement of the reference plate attached on the loaded end, as shown in Figure 3. If, for example, the case of a motorcycle front fork with a wheel is taken into account, the twist axis will be identified by the intersection of two planes, one parallel to the symmetry plane of the wheel in unloaded conditions, the other parallel to the symmetry plane of the wheel in loaded conditions.

In general, the planes are identified from the coordinates of the three points on the reference plate, which are named L1, L2 and L3. These coordinates are measured when the structure is unloaded (subscript *u*) and when the structure is loaded (subscript *l*), and are given by:

$$\begin{cases} L_{1u} = (x_0, 0, -z_0) \\ L_{2u} = (0, 0, -z_0) \\ L_{3u} = (0, 0, 0) \end{cases} \quad (3)$$

$$\begin{cases} L_{1l} = (x_0, \Delta y_1, -z_0) \\ L_{2l} = (0, \Delta y_2, -z_0) \\ L_{3l} = (0, \Delta y_3, 0) \end{cases} \quad (4)$$

Points 3 is conventionally defined as the origin of the system of coordinates. Constant lengths x_o and z_o define the position of points 1 and 2 with respect to point 3 and Δy_1, Δy_2 and Δy_3 are the displacements measured by the laser sensors in the direction perpendicular to the plate.

In the elaboration process, it is assumed that the reference plane in unloaded condition coincides with the plane x-z, while the reference plane in loaded condition is defined by the following constants:

$$\begin{cases} d = 1 \\ b = -d / \Delta y_3 \\ c = (b\Delta y_2 - d) / z_0 \\ a = (z_0 c - b\Delta y_1 - d) / x_0 \end{cases} \quad (5)$$

As state before, the twist axis is identified by the intersection of the two planes:

$$\begin{cases} ax + by + cz + d = 0 \\ y = 0 \end{cases} \quad (6)$$

A fourth laser sensor has been added to the measurements in order to improve the accuracy of the twist axis identification. The four laser outputs are processed at the same time and the deformed plane is identified by the particular coefficients *a*, *b*, *c* and *d* that minimize the sum of the squares of the errors between the measurement points and the identified plane.

1.3 Identification of the dynamic twist axis with actuator excitation

Up to now the twist axis has been used for describing the static deformation of a 2D structure. However, the same concept can be adopted for defining the dynamic deformability properties of the structure due to the effect of an harmonic excitation at assigned frequency. It is well-known in the field of solid mechanics and aero-elasticity that the twist axis moves when the frequency of excitation changes. In general, also when the structure is stimulated by a dynamic force the dynamic twist axis is result of a generic deformation of the structure that includes both bending and torsion effects. However, it is worth highlighting that if the frequency of excitation coincides with the natural frequency of the system and there is a sufficient frequency interval between adjacent modes, the dynamic deformed shape of the structure

actually is dominated by the mode of vibration in resonance condition and the corresponding dynamic twist axis is named modal twist axis.

In the framework of this research, two experimental methods have been developed in order to identify the position of the dynamic twist axis. The first method is very similar to the one presented in the previous paragraph, since it involves the use of the hydraulic actuator and the system of laser sensors. The tests differ from the static ones in the fact that the actuator is controlled in order to apply a harmonic load to the tested component. In this case, the displacements Δy_i measured on the metal plate have the meaning of amplitudes of displacement at the assigned frequency. For each test, a sine-wave fitting has been carried out on the laser outputs, that are shown in Figure 4. Then, the identification of the reference plane in loaded condition is carried out with the same formulas of equation (3), but in this case displacements Δy_i are calculated as the half amplitude of the sine waves (that is, as the difference between the mean value and the maximum value of the fitted sinusoid).

The main drawbacks of this testing method are connected to the possibility of investigating a narrow range of frequencies (1-45 Hz) due to the mechanical limits of the actuator and of acquiring information only for the specific frequency of excitation. Moreover, the connection between the stem of the hydraulic actuator and the structure alters the behavior of the structure and the tests require a large amount of time. The first drawback is particularly restricting because it is not uncommon for the most interesting modes of vibration to occur at frequencies higher than 45 Hz.

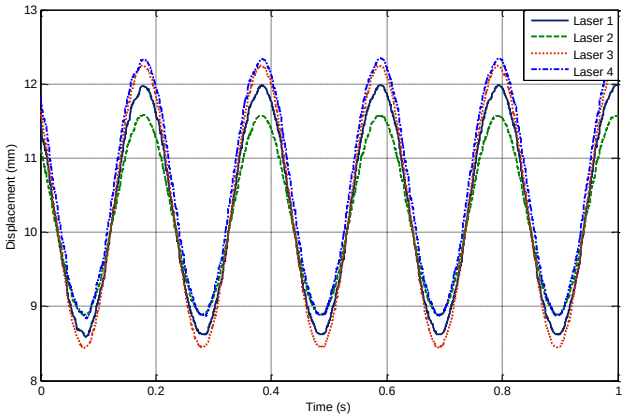

Figure 4 Laser outputs measured during a dynamic test carried out at 5 Hz

1.4 Identification of the dynamic (modal) twist axis with hammer excitation

The second method for identifying the modal twist axis employs a modal testing approach. In order to perform dynamic tests, the structure is excited by means of a hammer for modal analysis and the motion of the reference plate is measured by three accelerometers, which are attached to the metal plate as shown in Figure 5. In the framework of this research a PCB 086C03 impact hammer and three PCB M352C65 piezoelectric accelerometers (sensitivity 10 mV/m/s^2, range 2-6000 Hz) were used.

Three inertance Frequency Response Functions are measured at the same time. Then, dividing by $-\omega^2$ receptance FRFs are calculated, according to the following equation:

$$y(t) = -\ddot{y}(t) / \omega^2 \qquad (7)$$

For an assigned frequency of the measured FRFs, it is possible to calculate the vibration function of the three points of the metal plate, according to the following equation:

$$y_i(t) = \left|FRF_i(\omega)\right| \cos(\omega t + \varphi_i(\omega)) \quad (8)$$

In which $\left|FRF_i(\omega)\right|$ is the modulus and $\varphi_i(\omega)$ the phase of the three FRFs. Referring to the system of coordinates shown in Figure 5, at the instant *t* the three points of the plate have the following coordinates:

$$\begin{cases} A_1 = (x_0, \left|FRF_1(\omega)\right| \cos(\omega t + \varphi_1(\omega)), -z_0) \\ A_2 = (0, \left|FRF_2(\omega)\right| \cos(\omega t + \varphi_2(\omega)), -z_0) \\ A_3 = (0, \left|FRF_3(\omega)\right| \cos(\omega t + \varphi_3(\omega)), 0) \end{cases} \quad (9)$$

Constants x_o and z_o define the position of measurement points 1 and 2 with respect to point 3. Then two planes are defined: the former is defined by the three points of equation (9), the latter by equation (9) when no vibration is present (un-deformed plane). The intersection of two planes makes it possible to identify the modal twist axis for the assigned frequency.

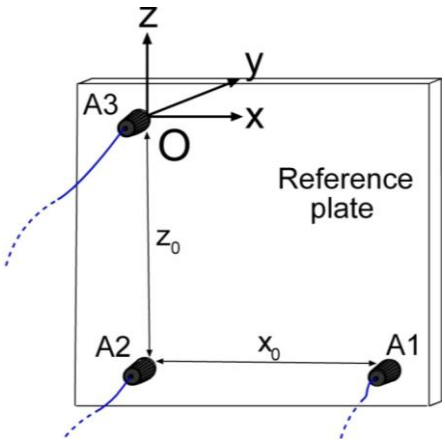

Figure 5 The arrangement of the mono-axial accelerometers on the reference plate

Equation (9) clearly shows that for a given frequency *ω* the coordinates of the three points depend on time and therefore the twist axis depends on time. This property appears a limit of the proposed method, since a twist axis depending on time is not very useful for the interpretation of the deformation characteristics of a structure. Actually a closer inspection of equation (9) reveals that, if phases $\varphi_i(\omega)$ are *0* or π, time dependence in equation (9) disappears and the twist axis is unambiguously defined. This favorable condition takes place because the three measurement points arrive at the maximum positive or negative displacement at the same time. Twist axis is not well defined only when there is a generic phase shift between the FRFs at the assigned frequency.

Phase shift between the FRFs can be easily checked from measured data, by selecting a specific frequency *ω* and plotting in the complex plane the three vectors having lengths equal to the moduli of the FRFs and angles equal to the phases of the FRFs. Results obtained for metallic structures (motorcycle forks and frames) have shown that in the bands of frequency around the first resonance peaks the phase shifts between the FRFs are close *0* or π, hence the modal twist axis calculated considering the maximum positive and negative displacement is well defined. In the rare cases in which the FRFs show more general phase shifts (like the ones of Figure 6), a practical method has been adopted to define the twist axis. Time domain

data are elaborated considering vibrations of the three reference points of the plate in the three instants in which each point arrives at the maximum amplitude (positive or negative). Three twist axis are calculated and the axis with average inclination and intercept with *y* axis is calculated.

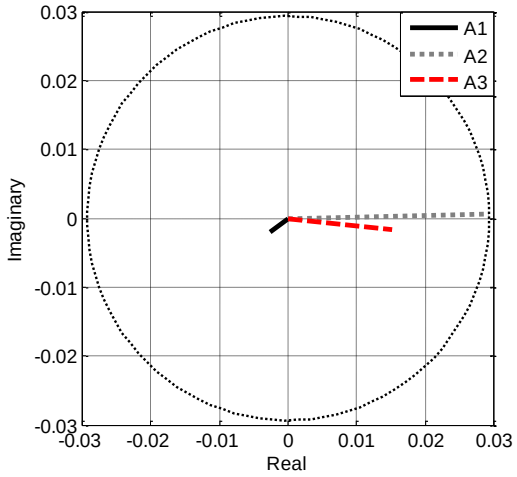

Figure 6 Phase shift occurring at 67 Hz in a measurement on front fork A

1.5 Twist axis and Mozzi axis

This section will introduce the concept of "Mozzi" or instantaneous screw axis, which can be used for analyzing results of the twist axes obtained from both static and dynamic tests. As already expressed in paragraph 2, the deformation of the loaded end of an almost two dimensional structure can be studied taking into account the motion of a reference plate attached to the loaded end. The reference plate is unloaded and follows rigidly the motion of the loaded end of the structure, hence the basic concepts of rigid body mechanics can be adopted for describing its motion.

Giulio Giuseppe Mozzi del Garbo, an Italian mathematician, in 1763 published the book *Discorso matematico sopra il rotolamento dei corpi* ("Mathematic Discourse on the Roll of Bodies") in which he stated that a generic differential spatial rigid motion can be considered a helical motion around a line, which is called the Mozzi axis [24]. In other words, the rigid motion of a body is represented in every instant by rotation about, and translation along, the Mozzi axis, which is also known as the instantaneous screw axis. The direction of the Mozzi axis coincides with the instantaneous direction of the angular velocity vector. The ideas of Mozzi were then developed by Cauchy in 1827, Poinsot in 1834, Chasles in 1878 [25] and Ball in 1900 [26] [27]. The Mozzi axis concept is useful for defining the deformability of those structures in which the most important characteristic is the motion of the loaded end with respect to the fixed end, like motorcycles and bicycles frames and forks.

Figure 7 shows the loaded end of a 2D structure with the reference plate. A fixed system of coordinates (origin O and axes x_f, y_f and z_f) and a system of coordinates that moves with the plate (origin Q and axes x_f, y_f and z_f) are defined. The basic equation for the study of the rigid motion of the reference plate is:

$$\begin{Bmatrix} v_{x_P} \\ v_{y_P} \\ v_{z_P} \end{Bmatrix}^f = \begin{Bmatrix} v_{x_Q} \\ v_{y_Q} \\ v_{z_Q} \end{Bmatrix}^f + {}^f_m[R] \begin{bmatrix} 0 & -\omega_z & \omega_y \\ \omega_z & 0 & -\omega_x \\ -\omega_y & \omega_x & 0 \end{bmatrix}^m \begin{Bmatrix} x_P \\ y_P \\ z_P \end{Bmatrix}^f \quad (10)$$

In which P is a point belonging to the rigid space moving with plate, ${}^{f}v_{xP}$ ${}^{f}v_{yP}$ ${}^{f}v_{zP}$ and ${}^{f}v_{xQ}$ ${}^{f}v_{yQ}$ ${}^{f}v_{zQ}$ are the components of the velocities of points P and Q in the fixed reference frame, ω_f , ω_f , ω_f the components of angular velocity and ${}^{m}x_P$ ${}^{m}y_P$ ${}^{m}z_P$ the coordinates of point P with respect to point Q in the moving reference frame. ${}^{f}_{m}[R]$ is the rotation matrix from the mobile to the fixed reference frame. If only small displacements are considered, the two coordinate systems are almost parallel and the rotation matrix can be considered a unit matrix. If point *P* belongs to the Mozzi axis, its velocity is aligned with the angular velocity vector and the cross product of angular velocity and linear velocity is zero:

$$\vec{\omega}\times\vec{v}_P = 0 \qquad (11)$$

In matrix form:

$$\begin{bmatrix} 0 & -\omega_z & \omega_y \\ \omega_z & 0 & -\omega_x \\ -\omega_y & \omega_x & 0 \end{bmatrix} \left(\begin{Bmatrix} vx_Q \\ vy_Q \\ vz_Q \end{Bmatrix} + \begin{bmatrix} 0 & -\omega_z & \omega_y \\ \omega_z & 0 & -\omega_x \\ -\omega_y & \omega_x & 0 \end{bmatrix} \begin{Bmatrix} x_P \\ y_P \\ z_p \end{Bmatrix} \right) = \begin{Bmatrix} 0 \\ 0 \\ 0 \end{Bmatrix} \qquad (12)$$

The matrix of this linear system has not full rank, hence equation (12) can be solved taking one of the coordinates (z_P) as an independent parameter. Thus the parametric equation of the Mozzi axis is obtained.

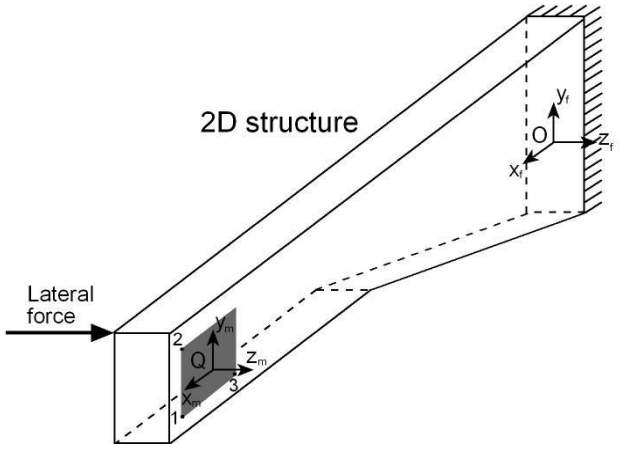

Figure 7 Loaded end of a 2D structure with the reference plate.

The case of a structure that does not bend in x-y plane is here taken into account considered, because out-of-plane compliance is the most interesting from the point of view of single track vehicle stability. Since in this case $\omega_x = 0$, the solution of equation (12) gives:

$$x_P = 0 \quad y_P = \frac{vx_Q}{\omega_z} + \frac{\omega_y}{\omega_z} z_P \qquad (13)$$

If an interval of time *dt* is considered, equation (13) can be written in terms of differential displacements and rotations:

$$x_P = 0 \quad y_P = \frac{dx_Q}{d\theta_z} + \frac{d\theta_y}{d\theta_z} z_P \qquad (14)$$

Since rotations $d\theta_y$ $d\theta_z$ cannot be measured in easy way, they can derived from the lateral displacements (*x* direction) of the three points of the reference plate.

The basic equation for the calculation of lateral displacements derives from:

$$\begin{Bmatrix} dx_i \\ dy_i \\ dz_i \end{Bmatrix} = \begin{Bmatrix} dx_Q \\ dy_Q \\ dz_Q \end{Bmatrix} + \begin{bmatrix} 0 & -d\theta_z & d\theta_y \\ d\theta_z & 0 & -d\theta_x \\ -d\theta_y & d\theta_x & 0 \end{bmatrix} \begin{Bmatrix} x_i \\ y_i \\ z_i \end{Bmatrix} \quad i = 1,2,3 \tag{15}$$

In which dx_i dy_i dz_i are the displacements of reference point *i* and x_i y_i z_i the coordinates of this point with respect to the reference system. Since only lateral displacements are relevant and can be measured, the three scalar equations are:

$$dx_i = dx_Q - d\theta_z y_i + d\theta_y z_i \quad i = 1,2,3 \tag{16}$$

$d\theta_y$ $d\theta_z$ and dx_Q can be calculated solving linear system (16) and then they are introduced into the equation that gives the Mozzi axis:

$$x_P = 0$$
$$y_P = \frac{(y_2 z_3 - y_1 z_1)dx_1 + (z_1 - z_3)dx_2 y_1 + (y_1 - y_2)dx_3 z_1}{(dx_2 - dx_1)(z_1 - z_3)} - z_P \frac{(dx_3 - dx_1)(y_1 - y_2)}{(dx_2 - dx_1)(z_1 - z_3)} \tag{17}$$

Figure 8 shows the reference plate in the unloaded and loaded configurations and the definition of the Mozzi (or instantaneous screw) axis.

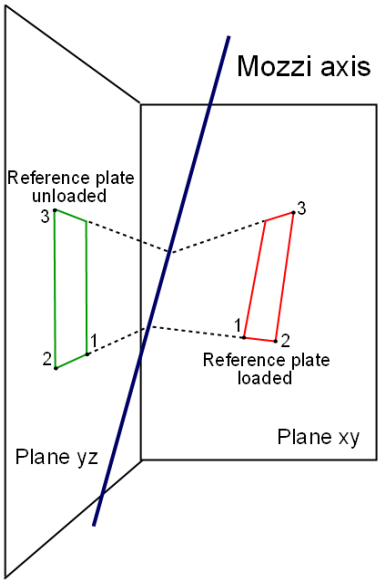

Figure 8 Definition of Mozzi (or instantaneous screw) axis.

Up to now the Mozzi axis has been used for describing the static deformation of a 2D structure. The same concepts can be adopted for defining dynamic deformation in the presence of an harmonic excitation at assigned frequency. In this case displacements dx_i have the meaning of amplitudes of displacement at the

assigned frequency. If the frequency of excitation is equal to the natural frequency of the system and there is a sufficient frequency interval between adjacent modes, the dynamic deformed shape of the structure actually is dominated by the mode of vibration in resonance condition and the corresponding twist axis is named the modal twist axis.

1.6 Modal analysis

The dynamic behaviour of the motorcycle and bicycle components tested in the framework of this Ph. D. was investigated also by means of a modal analysis approach. This paragraph describes some of the most important concepts of modal analysis and addresses to the most common issues that should be taken into account during laboratory tests. For a more detailed investigation of modal analysis techniques, the reading of more renowned and illustrious books [9] [10] is strongly suggested.

Modal analysis is an experimental technique that allows to measure the frequency response functions (FRF) of a mechanical system, starting from the measurements of the dynamic input and output of the system. The measured FRFs are generally processed in specific software codes, the processing aims to the identification of the dynamic properties of the mechanical system, expressed in terms of modes of vibration, natural frequencies and damping coefficients.

Modal analysis had its first taste of success about fifty years ago, when it was applied to the field of aerospace engineering in order to study the dynamic behavior of wings and airplanes under vibrational excitation. The interest in modal analysis was due to the firm idea that the measured dynamic properties do not depend on the characteristics of the excitation, but depend only on the innate characteristics of the mechanical system (mass, stiffness, damping coefficients, etc), so that these properties are a sort of a "fingerprint" of the mechanical system. Therefore, modal analysis was generally employed for the monitoring and the diagnostics of mechanical damages in structural components. If no damage occurs in the structure, the frequency response function will show no variations with the respect to the ones measured on the intact structure; otherwise, a variation of the natural frequencies or the modes of vibration will appear in the measurements.

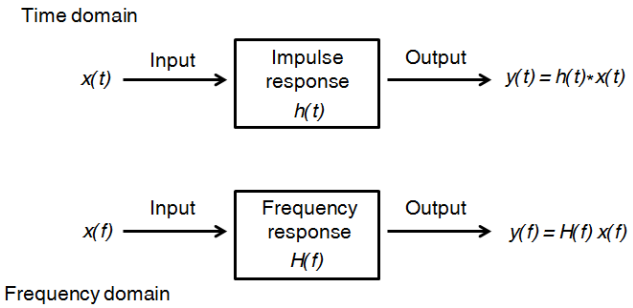

Figure 9 Impulse and frequency response of a system in time and frequency domains.

In general, the dynamic behavior of a mechanical system can be described by means of the impulsive response h(t) in the time domain, or by means of the frequency response function H(f) in the frequency domain (Figure 9). Depending on the selected domain, there are two sets of identification techniques: the time domain techniques are based on solving the following system of differential equations:

$$[M]\{\ddot{x}(t)\}+[C]\{\dot{x}(t)\}+[K]\{x(t)\}=\{F(t)\} \quad (18)$$

The frequency domain techniques base the identification of the dynamic properties on the measurement of the frequency response functions, which implicitly include all the information about the dynamic properties of the mechanical system. According to these techniques, equation (18) is solved in the frequency domain using the Fourier transform. The advantage of these techniques is the shifting from a system of differential equations to a simpler system of algebraic equations:

$$\left(M\omega^2 + C\omega + K\right)\cdot X(\omega) = F(\omega) \qquad (19)$$

The frequency response function (FRF) is defined as the ratio between the cross spectrum between a displacement component (output) and hammer force (input) and the autospectrum of the hammer force:

$$H(j\omega) = \frac{X(j\omega)}{F(j\omega)} \qquad (20)$$

Although the response variable for the previous equations was displacement, it could also have been velocity or acceleration (acceleration is currently the most accepted method).

Because it is a complex quantity, the FRF cannot be fully displayed on a single two-dimensional graph. It can, however, be presented in several forms, each of which has its own uses. One method for presenting the data is the Bode diagram, which is to plot the magnitude and phase versus frequency. At resonance, the magnitude reaches a peak and is limited only by the damping of the system; the phase ranges from 0 to 180° and the response lags the input by 90° at resonance. The magnitude can be expressed in linear scale or logarithmic scale (decibels). A linear scale is more useful for distinguish the major peaks in the frequency domain, a logarithmic scale is more useful for evaluating frequency components with small amplitudes (e.g. noise). Another method of presenting the data is to plot the rectangular coordinates, the real part and the imaginary parts versus frequency. For a proportional damped system, the imaginary part is maximum at resonance and the real part is 0. A third method of presenting the data is to plot the real part versus the imaginary part, which is often called a Nyquist plot.

Now, if a generic mechanical system with n-degrees of freedom is taken into account, the frequency response function matrix is introduced (Figure 10):

$$\begin{Bmatrix} x_1 \\ x_2 \\ x_n \end{Bmatrix} = \begin{bmatrix} H_{1,1}...H_{1,n} \\ \\ H_{n,1}...H_{n,n} \end{bmatrix} \begin{Bmatrix} F_1 \\ F_2 \\ F_n \end{Bmatrix} \qquad (21)$$

Under the hypothesis of linear system, the measurement of one row or one column of the FRF matrix is enough to carry out a thorough modal analysis of the mechanical system. One column of the FRF matrix is identified, if you have a roving response transducer and a fixed excitation point; otherwise, one row is identified with a roving excitation and a fixed response transducer. Usually, FRFs are measured exciting the mechanical systems by means of a shaker excitation or a hammer impact. From a theoretical point of view, it doesn't matter whether the measured FRFs have been acquired by means of a shaker tests or an impact test. Nevertheless, for real laboratory tests each technique shows some advantages and disadvantages, as summarized in Table 1. Table 2 shows the advantages and disadvantages of different types of constraints, which is another thorny issue when performing modal analysis. Sometimes it is not possible to choose *ad libitum* the types of excitation and constraint: the analysis of an aircraft, for example, is generally carried out with shaker excitation (more often, with many shakers at the same time) with the aircraft resting on its landing gear wheels. In other cases, the scientist can select the combination that best fits his purposes: the

testing constraints must be as similar as possible to reality, the measuring system must be easily recreated, portable, not expensive, etc.

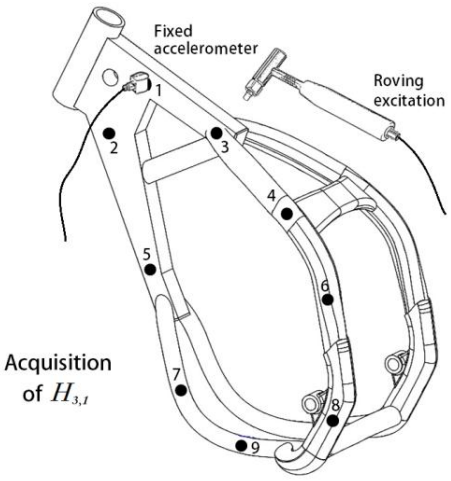

Figure 10 Acquisition of the FRFs matrix

In the framework of this Ph. D. the excitation has been exerted by means of a modally tuned hammer PCB 086C03 and the response has been measured by means of a tri-axial accelerometer PCB 356A16. In order to indentify the modal properties of the tested components, FRFs have been analyzed with the ICATS software, which allows the identification of the modal parameters (natural frequencies, modal dampings and modes of vibration) and the animation of the modes of vibration.

Excitation technique	Advantages	Disadvantages
Shaker	• Huge transfer of input energy (necessary for the analysis of bridges, houses, etc.)	• The equipment is not portable. • Not easy to connect to the structure. • Effect of the connection on the structure. • Low cut-off frequency. • Time demanding analysis.
Hammer	• The equipment is portable. • High cut-off frequency. • All frequencies excited at the same time.	• Hammers are more suitable for modal analysis of small or medium sized objects.

Table 1 Advantages and disadvantages of different excitation techniques

Constrain methods	Advantages	Disadvantages
Free-free	• Easy to be replicated.	• It does not match with the realistic operating conditions of the object.
Locked	• The object is studied in a more realistic condition.	• Hard to be replicated • The constrain can affect the consistency of the measurements.

Table 2 Advantages and disadvantages of different constrain methods

1.7 Stiffness decomposition

The aim of this section is to describe the method that allows to decompose the stiffness about the twist axis obtained from static tests in the bending and torsion stiffness of a motorcycle component making use of the results of dynamic tests (modal analysis and dynamic twist axes). According to this method, the measurement of the static twist axis and the dynamic twist axes (measured for the natural frequencies of the bending and torsional modes) is enough to identify the bending and torsion stiffness of a motorcycle component.

Stiffness decomposition is carried out considering two basic properties of the component under testing:

a) The lateral displacement of the point in which the force is applied during static tests, which is due to rotation about the twist axis, is equal to the sum of the displacements caused by the rotations about the bending and torsion axis respectively.

b) The rotation of the reference plate about twist axis is equal to the sum of rotations of this rigid body about bending and torsion axis respectively.

It is worth highlighting that the assumption of small rotations is made. This assumption makes it possible to consider the resultant rotation as the vector sum of components without considering the order in which they are performed. Property a) leads to the following equation:

$$x_{lat} = \vartheta_{tw} a_{tw} = \vartheta_{bend} a_{bend} + \vartheta_{tors} a_{tors} \quad (22)$$

in which, ϑ_{tw}, ϑ_{bend} and ϑ_{tors} are twist, bending and torsion angles, a_{tw}, a_{bend} and a_{tors} are twist, bending and torsion arms, which can be calculated from the measured positions of the twist axes. Since twist, bending and torsion angles are given by:

$$\vartheta_{tw} = F\frac{a_{tw}}{k_{tw}} \qquad \vartheta_{bend} = F\frac{a_{bend}}{k_{bend}} \qquad \vartheta_{tors} = F\frac{a_{tors}}{k_{tors}} \quad (23)$$

equation (22) becomes:

$$\frac{a_{tw}^{\,2}}{k_{tw}} = \frac{a_{bend}^{\,2}}{k_{bend}} + \frac{a_{tors}^{\,2}}{k_{tors}} \quad (24)$$

Property b) leads to the following equations:

$$\vartheta_{tw}\cos(\beta) = \vartheta_{bend}\cos(\beta_{bend}) + \vartheta_{tors}\cos(\beta_{tors}) \quad (25)$$

$$\vartheta_{tw}\sin(\beta) = \vartheta_{bend}\sin(\beta_{bend}) + \vartheta_{tors}\sin(\beta_{tors}) \quad (26)$$

In which β is the angle from *z* axis to static twist axis, β_{bend} is the angle from *z* axis to bending modal twist axis and β_{tors} is the angle from *z* axis to torsion modal twist axis. If equations (23) are introduced into equations (25) and (26) and the ratio between these equations is calculated, equation (27) is obtained, which correlates the angle of the static twist axis with the angles of the modal twist axes:

$$\tan(\beta) = \frac{\frac{a_{bend}}{k_{bend}}\sin(\beta_{bend}) + \frac{a_{tors}}{k_{tors}}\sin(\beta_{tors})}{\frac{a_{bend}}{k_{bend}}\cos(\beta_{bend}) + \frac{a_{tors}}{k_{tors}}\cos(\beta_{tors})} \quad (27)$$

Bending and torsion stiffness can be calculated solving the system of equations (24) and (27).

1.8 The Mototiremeter

In the framework of this research the measurement of tires static and dynamic properties have been performed on the *Mototiremeter*, a rotating disk tester machine developed in the last fifteen years at the University of Padova. The machine is equipped with a disk (diameter 3 m) that rotates about a vertical axis at a maximum speed of 50 km/h. The outermost part of the disk is covered by high friction material (sandpaper) and is the rolling track of the wheel. The wheel under testing is held in position on the rolling track by means of a hinged arm, which makes it possible to set side-slip and camber angles at assigned values. A brushless servomotor drives the camber rotation of the whole arm, the range is ±54°. A second brushless servomotor drives the rotation of the fork that sustains the wheel about the axis parallel to the stems and intersecting the contact patch, this rotation is named yaw rotation and its range is ±10°. The machine allows the tester to add extra-weights on the tip of the arm for simulating the mass of the rider and the motorcycle. Generally, the camber and side-slip maximum angles are limited to ±45° and ±6° respectively depending on the tire and on the load, in order to avoid dangerous oscillations of the whole arm. The yaw motion of the fork changes the attitude of the tire with respect to the track and generates the side-slip angle of the contact patch. These load cells are connected to the computer through some specific modules that read the signals.

Figure 11 The *Mototiremeter*

The tester machine is also equipped with three load cells. In particular, the first load cell locks the hinged arm in the lateral direction and measures the lateral force. The second load cell makes it possible the measurement of the moment around the diametrical axis that passes through the contact patch. The third load cell makes it possible the measurement of the moment about the wheel spin axis.
The identification of tires static tires properties is performed acquiring the outputs of the three load cells for specific camber and slip angles.

The identification of tires transient properties need the generation of variable slip-angles and the measurement of the lateral force. It can be carried out controlling the slip servomotor with different inputs, typically step inputs and harmonic inputs are used.

1.9 Tires relaxation length

The measurement of tires dynamic properties (i.e. relaxation length) has been carried out on the specific *Mototiremeter* specific machine of the MDRG. In this research, the slip (yaw) servomotor of the tester machine generates harmonic inputs of constant amplitude (1.5°) and variable frequency (from 0.42 to 2.10 Hz). With this excitation the transient properties of tires generate a phase lag between the input motion and the measured lateral force. The input motion is measured placing a rate gyro on the fork that holds the wheel under testing. The measured angular velocity (yaw rate) is fitted with a sine function and the phase of the enforced yaw oscillation is calculated simply s that in harmonic motion the velocity signal leads $\pi/2$ the displacement signal. The lateral force is measured by the load cell of the tester machine and it is fitted with a sine function. The phase lag between the fitted signals is calculated, elaborations are carried out by means of a MATLAB code. Relaxation length is calculated from the measured phase lag (φ) according to the following equation:

$$\sigma = C_{bF\alpha} \frac{\tan(\varphi) + a\frac{\omega}{V}}{a\left(\frac{\omega}{V}\right)^2 \tan(\varphi) - \frac{\omega}{V}} \qquad (28)$$

in which $C_{bF\alpha}$ is the cornering stiffness of the tire, ω is the yaw excitation frequency, *V* is the forward speed and *a* is half of the length of the contact patch. Tests have been carried out for a forward speed of the wheel of V=5 km/h.

Chapter 2 – Identification of the structural properties of motorcycle frames in static and dynamic conditions

In the framework of this research, three motorcycle frames have been tested. The first two frames (A and B) that are presented in this chapter have been submitted to a huge number of tests and their analysis will be shown in the same paragraph. The test aim was the characterization of the stiffness properties of the motorcycle frames by means of the experimental technique developed in the framework of this research, which consists in the identification of the bending and torsional stiffness and combines the results of static and dynamic measurements. Moreover, for these two frames, the effect of different constraint solutions has been studied: a first series of tests has been carried out in a front constrained condition, that is locking the frame at the steering head and applying the excitation to the swingarm pivot; then, a second series of tests has been carried out in the rear constrained condition, that is locking the frame swingarm pivot and applying the excitation to the steering head.

The third motorcycle frame (frame C) has been used for studying the effect of the engine on the stiffness properties of the frame.

2.1 Frame A and Frame B

The frames (Figure 12) are two steel frames designed for enduro and moto-cross applications and have a limited mass: frame A weights 11.1 kg, frame B weights 11.4 kg. Frame A is characterized by a more compact design, in which the front part is stiffened by a heavy steel block that joints the steering head and the four tubes for the housing of the engine. Frame B shows a very thick and stiff square tube on the upper part, and the lower part is characterized by a series of tubes whose cross circular section varies from 20 to 35 mm. A long tail for the saddle and the exhaust support is welded to the frame.

Figure 12 Frame A and Frame B

Static tests of frames A and B for the identification of the static twist axis have been carried out applying a slowly varying force (range ± 300 N) both locking the steer tube to the jaws of the testing rig (front-constrained condition) and locking the swing arm pivot to the jaws (rear-constrained condition). The former test is useful for evaluating the displacement of the rear wheel with respect to the steering head that is due to bending and torsion compliance of the frame. The latter test is useful for evaluating the displacement of the front wheel that is caused by bending and torsion compliance of the steering head.

Preliminarily to the identification of the static and dynamic Mozzi axes, however, a modal analysis of the frames has been carried out. In the case of front-constrained condition, the modally tuned hammer has been used for producing an impact to the swing arm pivot of the frames and the tri-axial accelerometer has been moved to 20 (frame A) and 26 (frame B) different points of the frames. The three axes of the accelerometer were oriented as follows: x-axis in the vertical direction, y axis in the traveling direction and z axis (lateral direction) as the vector product between x and y. In the case of rear-constrained condition, the frames have been excited applying an impact on the steering head and moving the accelerometer to the same points of the previous constrain condition.

Figure 13 deals with the results obtained on frame A. In front-constrained conditions, three different modes have been identified from 0 to 100 Hz: the first mode at 26.5 Hz is a lateral mode (z axis), the second mode at 56.8 is a longitudinal mode (y axis, not displayed) and the third mode at 77.0 Hz is a torsional mode. The pictures of Figure 13 show the maximum displacements of the points of frame A for the lateral and torsional modes with respect to their equilibrium position. For the rear-constrained condition, the mode at 43.0 Hz is a lateral mode of the frame (z direction), in which the steering head exhibits the maximum displacement. The mode at 109.8 Hz is a torsional mode, in which the points of the upper part and the points of the lower part of the frame move in opposition.

The same analysis has been carried out for frame B (Figure 14). In the front-constrained condition, the mode in the lateral direction at 35.0 Hz is similar to the one measured for frame A. The torsional mode of frame B, on the contrary, is very different: owing to the tail moment of inertia, the natural frequency is much lower (about 42 Hz); moreover, the thick and stiff upper tube of the frame is almost motionless, and vibrations occur in the lower part of the frame and in the tail (which move in opposition). In the rear-constrained configuration, the resonance peak at 36.2 Hz corresponds to the lateral bending mode, in which the frame deflects mainly in the z direction. The resonance peak at 116 Hz corresponds to the torsional mode, in which the lower part of the frame and the tail move in opposition.

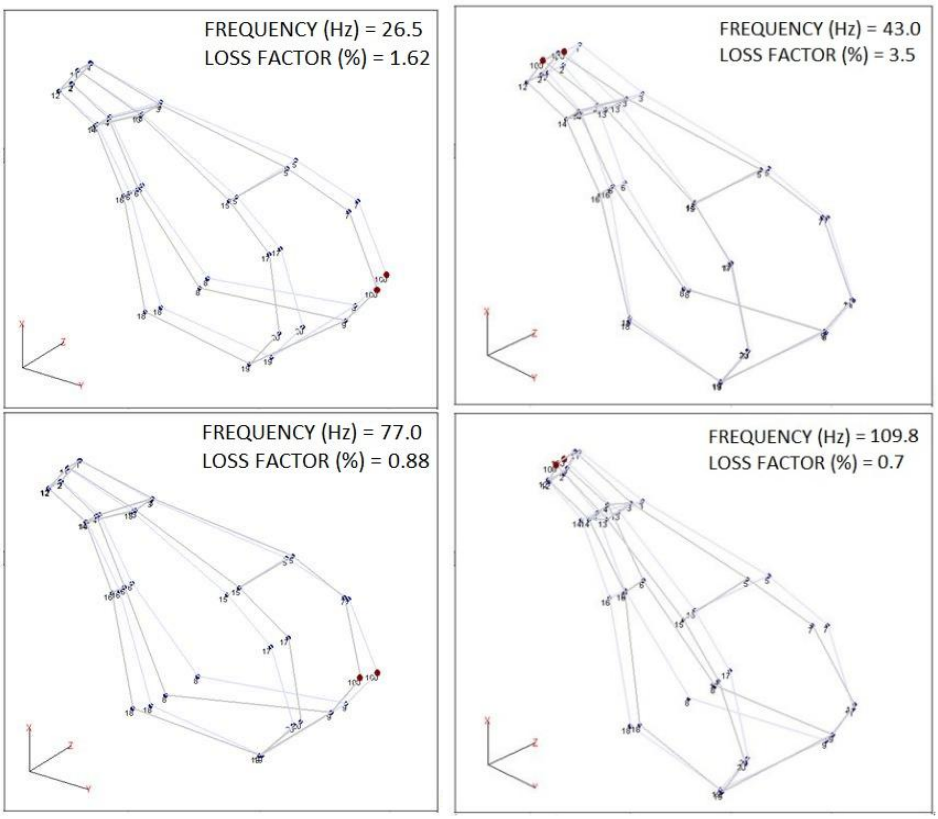

Figure 13 Displacements of nodes in the lateral and the torsional modes of frame A, front (left) and rear (right) constrained conditions.

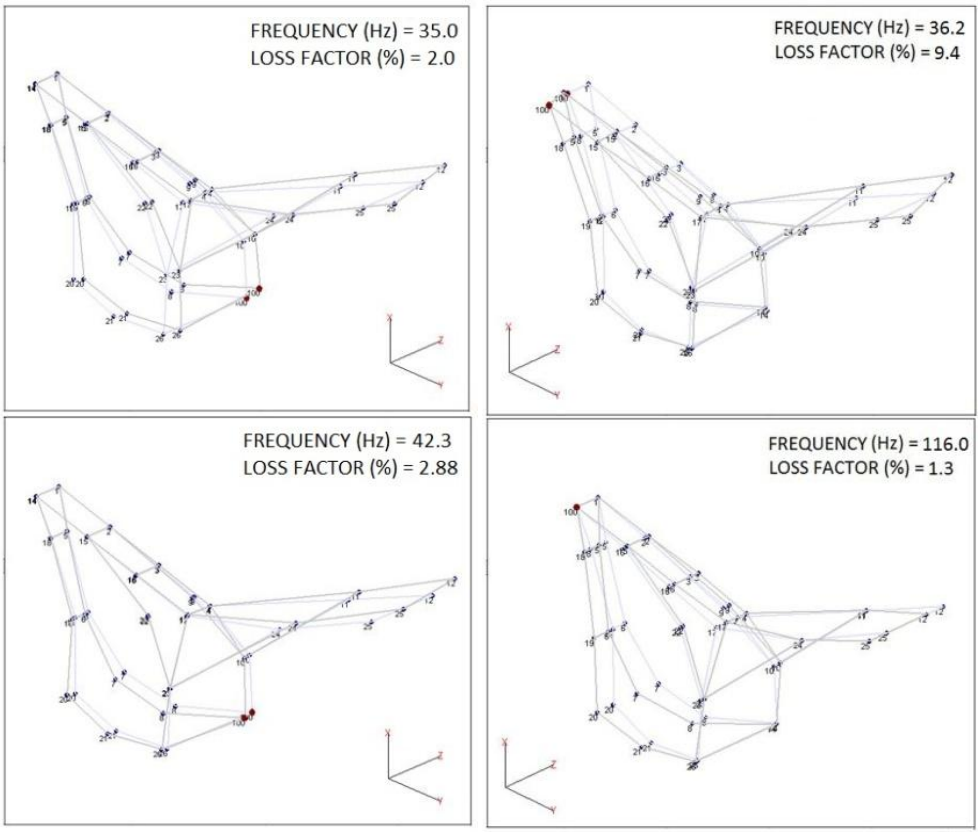

Figure 14 Displacements of nodes in the lateral and the torsional modes of frame B, front (left) and rear (right) constrained conditions.

Having performed modal analysis, it is now possible to examine the results of the identification of the Mozzi axes. Figure 15 deals with the tests carried out on frame A locking its steering head and shows the static twist axis measured applying an out-of-plane force at the swing arm pivot of frame A. The black thick point is the point where the force has been applied, the small red points are the points of the reference plate in which the displacement have been measured by means of laser sensors, and the green empty circle is the center of gravity of the frame. It is interesting to observe that the static twist axis intersects the frame between the locked steering head and the center of gravity; its orientation is almost orthogonal to the upper tube of the frame.

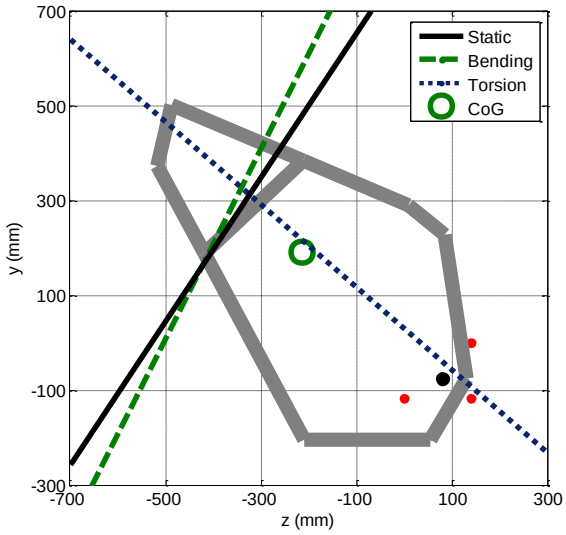

Figure 15 Frame A, front-constrained, static and dynamic twist axes

Linear stiffness has been identified calculating the ratio between the applied force and the lateral displacement of the swing-arm pivot, according to the formula:

$$k_{lat} = F / x_{lat} \qquad (29)$$

Then, the equivalent rotational stiffness has been identified multiplying the lateral stiffness for the squared twist arm, which is the distance between the twist axis and the swing-arm pivot:

$$k_{tw} = k_{lat} a_{tw}^2 \qquad (30)$$

Linear and twist stiffness of frame A in the front-constrained condition are presented in Table 3.

	Constraint condition	Linear stiffness	Twist arm	Rotational stiffness
Frame A	Front-constrained	167 kN/m	0.551 m	50.8 kNm/rad
Frame B	Front-constrained	272 kN/m	0.689 m	129 kNm/rad
Frame A	Rear-constrained	253 kN/m	0.475 m	57.0 kNm/rad
Frame B	Rear-constrained	238 kN/m	0.498 m	59.1 kNm/rad

Table 3 Linear stiffness and rotational stiffness about the static twist axis.

The same measurements carried out on frame B led to a quite different result, which is shown in Figure 16. The twist axis does not intersect the frame, but it is positioned above the frame and forms a small acute angle with the horizontal axis. This result can be explained taking into account the design of frame B: the upper tube of the frame is very thick and stiff, whereas the lower tubes have a smaller diameter and are

less stiff. When the frame is excited at the swing arm pivot, it undergoes a torsion deformation about its stiffer tube and the twist axis moves to the top of the frame.

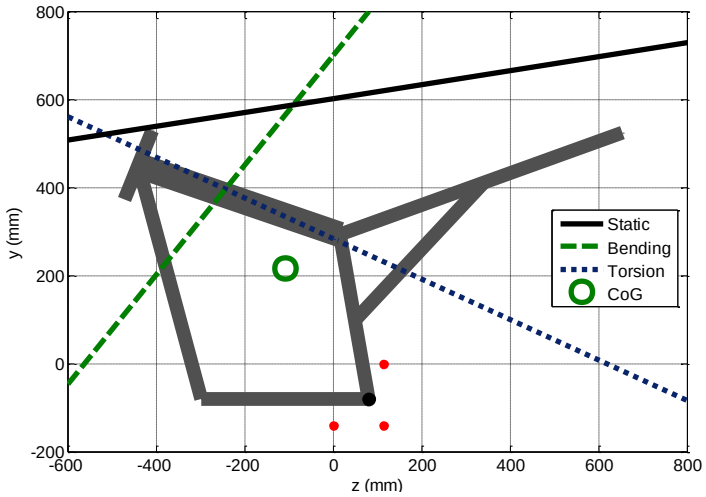

Figure 16 Frame B, front-constrained, static and dynamic twist axes.

Lateral and rotational stiffnesses of frame B have been identified with the same formulas used for frame A, and results are summarized in Table 3.

At a second stage, the identification of the modal twist axes has been carried out for frequencies close to the natural frequencies of the peaks measured by means of modal analysis. The tests for this analysis have been performed in front-constrained and rear-constrained conditions as well and the modal twist axes have been identified with the three-accelerometers technique described in the previous chapter. As plotted in Figure 15, at the natural frequency of the bending mode the modal twist axis is almost orthogonal to the upper tubes of the frame, because the vibration is dominated by bending deformation. At about the natural frequency of the torsional mode, on the contrary, the torsion mode occurs and the modal twist axis is almost parallel to the frame structure. It is interesting to highlight that the bending modal twist axis is very close to the static twist axis. This phenomenon is due to the fact that the natural frequency of the first mode of vibration (bending mode) is much lower than the one of the second mode (torsion mode). Hence, for low frequency or static excitation, bending deformation is predominant.

Figure 16 displays the identified modal twist axes for frame B in the front-constrained condition. At the natural frequency of the bending mode, the modal twist axis intersects the frame between the locked steering head and the centre of gravity and is almost orthogonal to the square tube of the frame, actually this mode is dominated by bending deformation of the frame and in particular of the square tube. At the natural frequency of the torsional mode, the modal twist axis is almost parallel to the square tube, because the frame undergoes a torsion deformation in which the square tube is almost motionless and vibrations occur in the lower part of the frame and in the tail that move in opposition. It is worth highlighting that for frame B (front-constrained) the direction of the static twist axis is a combination of the directions of the modal twist axes, because the natural frequencies of the bending and torsion modes are very close and both modes give a large contribution to static deformation of the frame.

Similar tests have been carried out in the rear-constrained condition. In frame A the static twist axis passes between the locked end (swing-arm pivot) and the center of gravity in the rear-constrained condition as well, as shown in Figure 17. Rotational stiffness about the twist axis is a bit larger than in the front-constrained condition. This result agrees with the fact that in the rear-constrained condition the most

stressed region of the frame coincides with the part of the structure which has the largest moment of inertia.

Frame B exhibits in the rear-constrained condition (Figure 18) a very different behavior from the one in the front-constrained condition. In this case frame B tends to behave like a cantilever structure with the twist axis passing between the locked end and the center of gravity. The direction of the twist axis is almost perpendicular to the large square tube of the frame. Lateral and rotational stiffnesses have been identified with the formulas presented for the front-constrained case. The value of rotational stiffness about the twist axis is comparable with the one of frame A in front-constrained condition (Table 3). In general, stiffness results presented in Table 3 are in reasonable agreement with the ones presented in [8], in which the whole rear frame of the motorcycle was considered, including the engine and swing-arm.

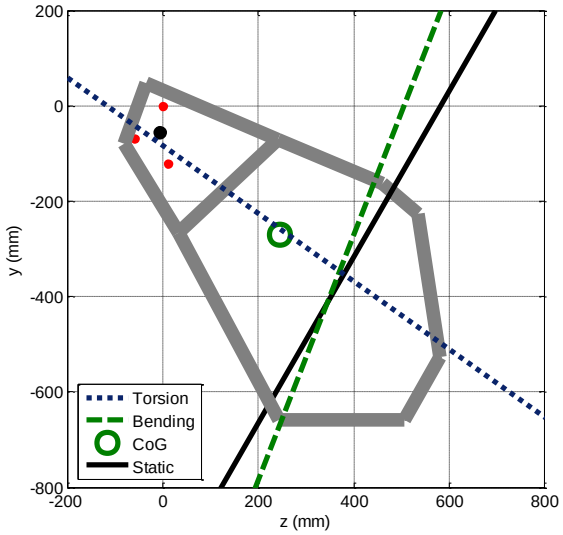

Figure 17 Frame A, rear-constrained, static and dynamic twist axes.

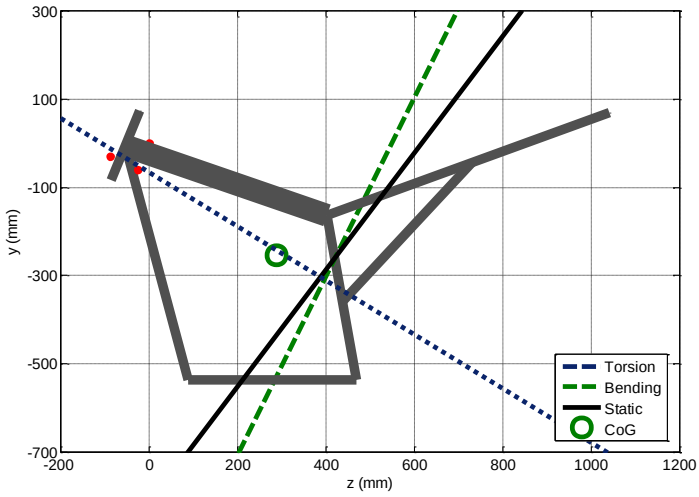

Figure 18 Frame B, rear-constrained, static and dynamic twist axes.

The other axes that are shown in Figures 17 and 18 are the identified modal twist axes for frames A and B. Figure 17 shows the modal twist axes of frame A in the rear-constrained condition. For the bending mode the modal twist axis is almost perpendicular to the upper tubes of the structure; for the torsional mode, the modal twist axis is directed from the rear pivot (where the frame was constrained) to the steering head.

The graph allows also a comparison between the static twist axis and the modal twist axes, the static twist axis is almost aligned with the modal twist axis of the bending mode.

Finally, Figure 18 collects the modal twist axes for frame B in the rear-constrained condition. The two axes are almost perpendicular and also in this case the static twist axis is almost aligned with the modal twist axis of the bending mode.

The last analysis performed on frames A and B consisted in the decomposition of the twist stiffness in bending and torsion stiffness components. The decomposition method has been described in chapter 1 and results are summarized in

Table 4. Bending stiffnesses of frame A in the two constraint conditions are very similar, whereas torsion stiffness in the front-constrained condition is larger than the one in the rear-constrained condition. Coming to frame B, bending and torsion stiffnesses in rear-constrained condition are similar to the ones of frame A, whereas in front-constrained condition bending stiffness is very large. This result can be explained considering the particular characteristics of this frame in the front-constrained condition: bending deformation is concentrated in the rear lower part of the frame that moves with respect to the steering head and also with respect to the upper tube, which is very stiff.

	Constraint condition	Bending arm	Bending stiffness	Torsion arm	Torsion stiffness
Frame A	Front-constrained	0.556 m	52.1 kNm/rad	0.032 m	22.0 kNm/rad
Frame B	Front-constrained	0.553 m	138.3 kNm/rad	0.298 m	60.4 kNm/rad
Frame A	Rear-constrained	0.458 m	53.5 kNm/rad	0.026 m	19.6 kNm/rad
Frame B	Rear-constrained	0.510 m	64.3 kNm/rad	0.097 m	60.2 kNm/rad

Table 4 Calculated values of bending and torsion stiffness.

2.2 Frame C

Frame C is designed for sporting applications, it is not heavier than frames A and B (its weight is 10.8 kg) due to its material (aluminum alloy) but has got a more compact design due to a design characterized by metal plates instead of tubes.

First, modal analysis of frame B without the engine has been carried out. The impact has been applied to the swingarm pivot and the tri-axial accelerometer has been moved to 22 different points of the frame. The identified natural frequencies of frame B without the engine are 42.2 Hz for the lateral mode and 109.2 Hz for the torsional mode, as shown in Figure 19. Then, the engine has been mounted on the frame and modal analysis has been performed again, measuring vibrations also on 10 points of the engine. The elaboration of the FRFs resulted in the identification of the lateral mode at 17.6 Hz and the torsional mode at 68.7 Hz. The natural frequencies of the frame with the engine are much lower than the ones of the frame alone, due to the mass of the engine. Figure 19 shows the modal shapes of the lateral and torsional modes.

Having performed modal analysis, tests for the identification of the static and dynamic Mozzi axis have been carried out. The tests of the frame for the identification of the static Mozzi axis have been carried out applying a slowly varying force (range ± 300 N) to the swingarm pivot in both cases of frame with and without the engine.

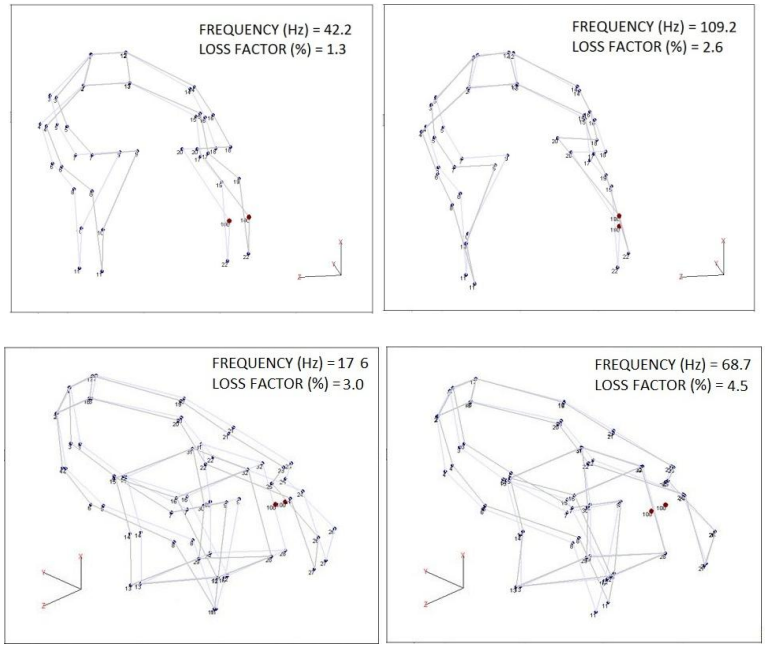

Figure 19 Displacements of nodes in the lateral and the torsional modes of frame , without and with the engine.

Figure 20 shows the results of the tests carried out on frame B without the engine. The static Mozzi axis is almost orthogonal to frame C, but it doesn't intersect the frame and lies beyond the column of the testing rig. This result can be explained taking into account the particular design of frame B which has two long lateral beams that are almost parallel and connect the rear part of the frame (with the swingarm pivot) to the steer head. Actually, owing to the deflection of the lateral beams, the rear part of the frame tends to move parallel to the steer head and for this reason the static Mozzi axis is located beyond the steer axis. Concerning the identification of the modal Mozzi axis, at the frequency of the bending mode the Mozzi axis moves even farther from the frame. The Mozzi axis identified for the natural frequency of the torsion mode is almost parallel to frame B and intersects it in its lower part.

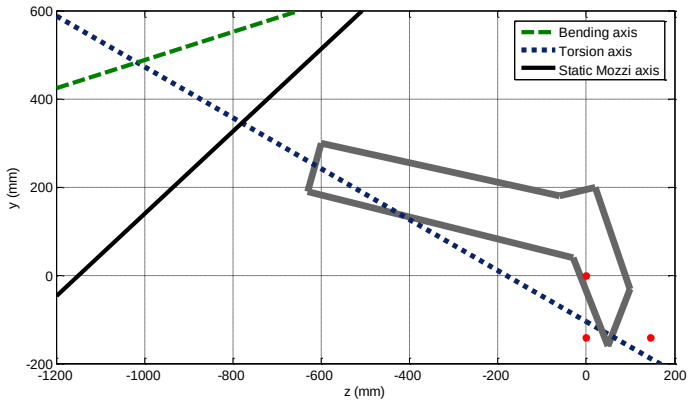

Figure 20 Frame C without the engine, static and modal Mozzi axes.

Then, the engine has been mounted on frame C and the identification of the static and dynamic Mozzi axes has been carried out. Results are shown in Figure 21. Both the static Mozzi axis and the Mozzi axis corresponding to the natural frequency of the bending mode get closer to the steer head of the frame, also in this case the dynamic axis is farther from the frame than the static one. The orientation of the Mozzi axis of the torsional mode is less affected by the presence of the engine and is almost parallel to the frame.

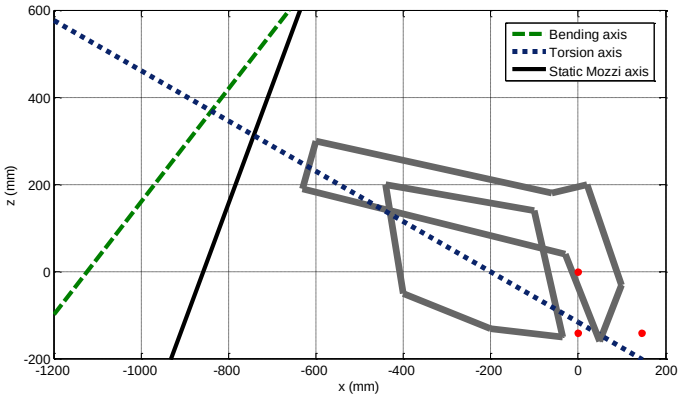

Figure 21 Frame C with the engine, static and modal Mozzi axes.

Finally, the stiffness properties of the frame have been identified, the results of the identification are summarized in Table 5. From a close examination of the figures, it is evident that the engine has a significant effect on the stiffness properties of the frame: the linear stiffness increases of about 50%; the twist and the bending stiffnesses of the frame increase of about 60%, whereas the torsion stiffness almost doubles when the engine is mounted on the frame.

	Linear stiffness [N/mm]	Twist stiffness [kNm/rad]	Bending stiffness [kNm/rad]	Torsion stiffness [kNm/rad]
Without engine	361	260.2	358.6	58.4
With engine	539	414.6	522.9	104

Table 5 Stiffness parameters identified for frame C

Chapter 3 - Identification of the structural properties of motorcycle swing arms in static and dynamic conditions

Two motorcycle swing-arms have been tested in the framework of this research. The first swing-arm (swing-arm A) is designed for enduro applications, is characterized by a simple geometry and its weight is limited to only 3.50 kg. The second swing-arm (swing-arm B) is designed for a sporting motorcycle, the design is more bulky and compact and its weight is 4.75 kg.

Static tests on the two swing-arms have been carried out locking the swing-arm pivot to the stiff column of the testing rig and applying a static load by means of the actuator on the wheel hub in order to imitate the realistic excitation that is caused by the contact between the road and the rear wheel. Modal analysis and dynamic tests for the identification of the modal twist axis have been carried out locking the swing-arm pivot to the stiff column, but with the actuator disconnected from the component in order to not affect its natural dynamic properties.

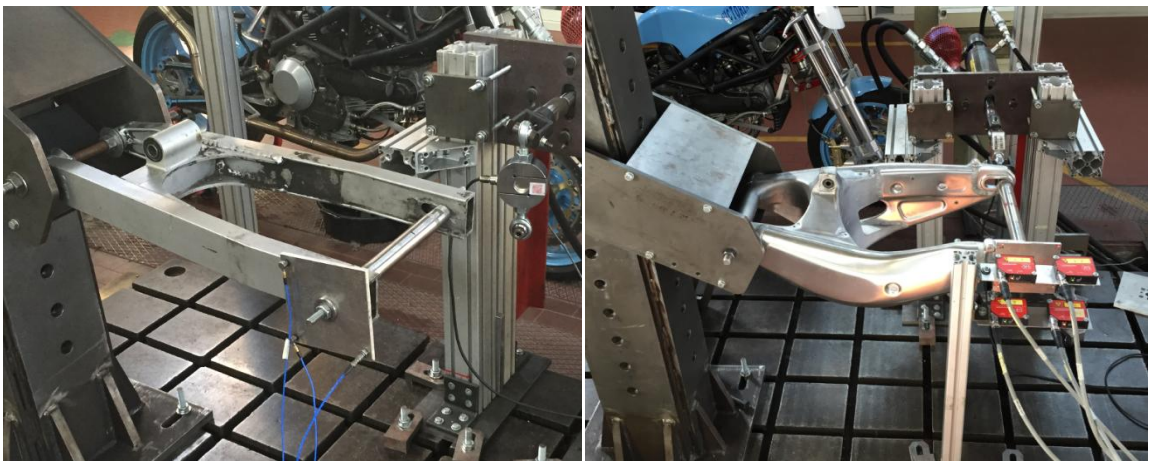

Figure 22 Swing arm A and swing arm B during tests on the *Mototiremeter*

3.1 Swing-arm A

For modal analysis tests, the hammer impulse was applied each time on the rear wheel hub (point 100), while the tri-axial accelerometer was attached each time to a different point. The accelerometer was oriented as follows: x-axis aligned with a vertical axis, y-axis aligned with the axis of the swing-arm stems and z-axis as vector product between x and y. a Due to the simple geometry of the swing-arm, FRFs have been measured only on six points of the swing-arm.

The vibration modes have been identified by means of ICATS software. The first two modes of swing-arm A A are displayed in Figure 23. The mode at 115 Hz is a lateral mode of the swing-arm (z direction), in which the rear wheel hub exhibits the maximum displacement. The mode at 184 Hz is a torsional mode, in which the right and left stems of the swing-arm move in opposition. A summary of the identified modal parameters is shown in Table 6.

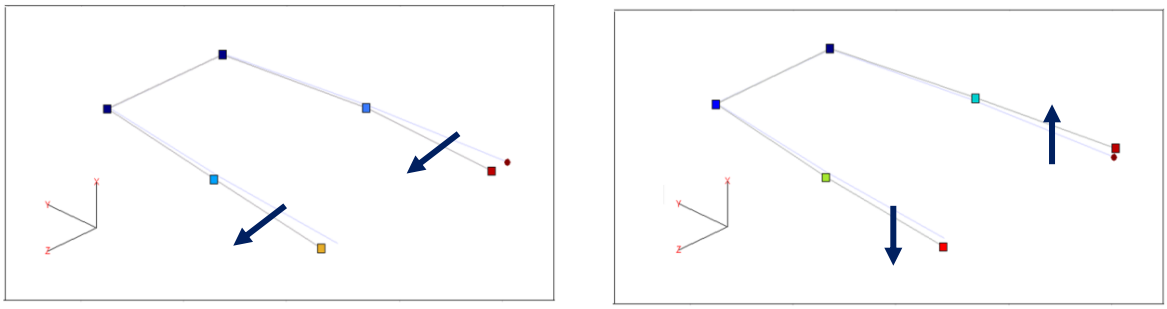

Figure 23 Displacements of nodes in the lateral and the torsional modes of swing-arm A.

Dynamic properties		
	Frequency	Hysteretic damping
Bending mode	115 Hz	1.73 %
Torsional mode	184 Hz	1.02 %

Table 6 Modal parameters of swing-arm A.

Figure 24 summarizes the output of the tests carried out on swing-arm A for the identification of the static and dynamic twist axes. Due to the very essential geometry of the swing-arm, it has been plotted as a simple thick grey line. The static twist axis intersects the swing-arm at about one third of its length and is almost orthogonal to its major axis. This result is in satisfactory agreement with the theory of solid mechanics about the twist axis of a cantilevered beam locked at one end and stressed with a static force at the free end. Linear stiffness has been identified calculating the ratio between the applied force and the lateral displacement of the rear wheel hub, according to the formula:

$$K_{lat} = F / y_{lat} \qquad (31)$$

Then, the equivalent rotational stiffness has been identified multiplying the lateral stiffness for the squared twist arm, which is the distance between the twist axis and the rear wheel hub:

$$K_{tw} = K_{lat} a_{tw}^2 \qquad (32)$$

The identified linear and rotational stifnesses are summarized in Table 7.

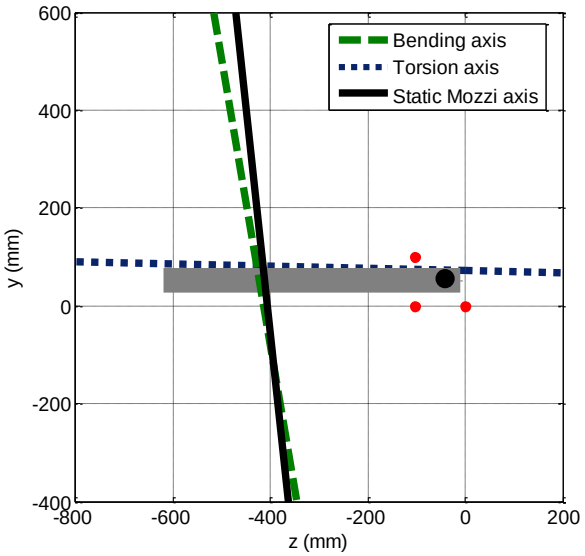

Figure 24 Swing-arm A static and dynamic twist axes.

Shifting the attention to the modal twist axes, it is interesting to highlight that at about the natural frequency of the bending mode the modal twist axis crosses the swing-arm almost orthogonally, because it vibrates in the lateral direction. At about the natural frequency of the torsional mode, on the contrary, the modal twist axis is almost orthogonal to the one previously identified and perfectly parallel to the swing-arm geometry.

Finally, the decomposition for the identification of bending and torsional stiffness has been carried out and results are summurized in Table 7.

Static properties	
Linear stiffness	623 kN/m
Twist arm	0.375 m
Twist stiffness	87.6 kNm/rad
Bending arm	0.388 m
Bending stiffness	94.2 kNm/rad
Torsion arm	0.025 m
Torsional stiffness	98.8 kNm/rad

Table 7 Stiffness parameters identified for swing-arm A

3.2 Swing-arm B

Modal analysis has been performed with the same method described for swing-arm A, but in this case the FRFs have been measured on 18 points due to the three-dimensional shape of swing-arm B. The vibration modes have been identified by means of ICATS software and are displayed in Figure 25. The mode at 134 Hz is a lateral mode of the swing-arm (z direction), in which the rear wheel hub exhibits the maximum displacement. The mode at 208 Hz is a torsional mode, in which the right and left stems of the swing-arm move in opposition.

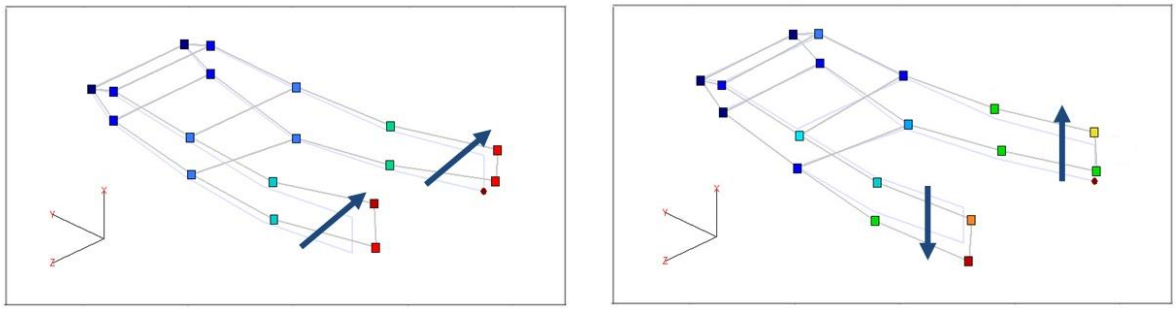

Figure 25 Displacements of nodes in the lateral and the torsional modes of swing-arm B.

Dynamic properties		
	Frequency	Hysteretic damping
Bending mode	134 Hz	0.74 %
Torsional mode	208 Hz	0.97 %

Table 8 Modal parameters of swing-arm B.

Figure 26 summarizes the output of the tests carried out on swing-arm B for the identification of the static and dynamic twist axes. The geometry of this swing-arm is more complex and in the plane x-z it has been sketched as a two-dimensional silhouette vaguely resembling a triangle. Also in this case, the static twist axis is almost orthogonal to the swing-arm geometry, but the intersection is closer to the stiff column of the testing rig. Linear stiffness and twist stiffness have been identified similarly as for swing-arm A and the identified static properties are summarized in Table 9.

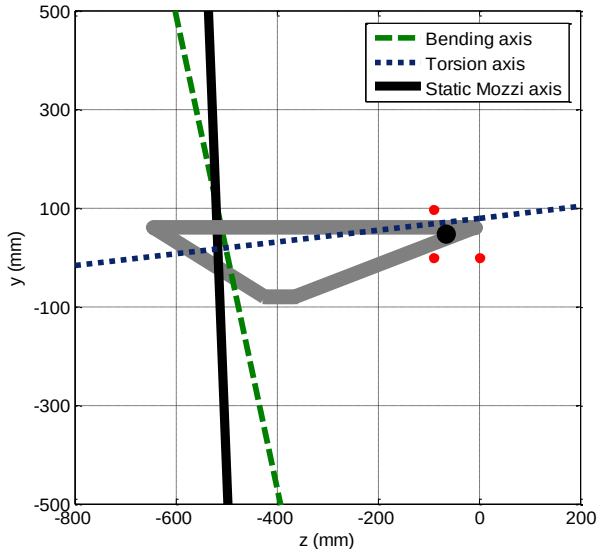

Figure 26 Swing-arm B static and dynamic twist axes.

Finally, the identification of the modal twist axis with the three accelerometers technique has been carried out (the dotted and dashed axes of Figure 26). At the natural frequency of the bending mode the modal twist axis crosses the swing arm almost orthogonally (bending mode); at about the natural frequency of the torsional mode, on the contrary, the modal twist axis is almost parallel to the swing arm (torsion mode). A summury of the identified modal parameters is shown in Table 8.

Static properties	
Linear stiffness	1083 N/m
Twist arm	0.477 m
Twist stiffness	246.4 kNm/rad
Bending arm	0.451 m
Bending stiffness	222.4 kNm/rad
Torsion arm	0.026 m
Torsional stiffness	77.4 kNm/rad

Table 9 Stiffness parameters identified for swing-arm B.

Chapter 4 - Identification of the structural properties of motorcycle front forks in static and dynamic conditions

Two motorcycle front forks have been tested in the framework of this research. The first fork (fork A) is designed for enduro applications, is characterized by two long and flexible stems and its weight is 12.1 kg. The second fork (fork B) is designed for a super-sport motorcycle, the design is more bulky and compact, the stems are shorter than the ones of fork A and its weight is 14.3 kg.

Static tests on the two forks have been carried out locking the steering head to the stiff column of the testing rig and applying a static load by means of the actuator on the lowest point of the front wheel in order to imitate the realistic excitation that is generated at the contact point between the road and the front wheel.

In contrast with the case of frames and swing-arms, in the case of front forks the stiffness decomposition can be carried out with a different method due to the simple two-dimensional geometry of those components and to the consequent assumption that the torsion axis is aligned with the major axis of the stems. Additional tests that will not be shown confirmed that the torsion axis is almost perfectly aligned with the fork.

The rotational bending and torsion stiffnesses are calculated solving a system of equations in which ϑ_{tors}, ϑ_{bend} and ϑ_{twist} are torsion, bending and twist angles, a_{tors}, a_{bend} and a_{twist} are torsion, bending and twist arms and k_{tors}, k_{bend} and k_{twist} are torsional, bending and twist stiffnesses respectively. The first equation states that the displacement of the point in which the force is applied caused by the rotation about the twist axis has to be equal to the sum of the displacements caused by the rotations about the bending and torsion axis respectively:

$$\vartheta_{twist} \cdot a_{twist} = \vartheta_{bend} \cdot a_{bend} + \vartheta_{tors} \cdot a_{tors} \quad (33)$$

Since twist, bending and torsion angles are given by:

$$\vartheta_{twist} = F \frac{a_{twist}}{k_{twist}} \qquad \vartheta_{bend} = F \frac{a_{bend}}{k_{bend}} \qquad \vartheta_{tors} = F \frac{a_{tors}}{k_{tors}} \quad (34)$$

the equation becomes:

$$\frac{a_{twist}^{\ 2}}{k_{twist}} = \frac{a_{tors}^{\ 2}}{k_{tors}} + \frac{a_{bend}^{\ 2}}{k_{bend}} \quad (35)$$

The second equation states that the ratio between torsion and bending angles must be equal to the tangent of the angle between the twist axis and the fork axis.

$$tg(\alpha) = \frac{a_{tors} k_{bend}}{k_{tors} a_{bend}} \quad (36)$$

The identified stiffness parameters are shown in the sections dealing in detail with fork A and fork B.
Modal analysis and dynamic tests for the identification of the modal twist axis have been carried out locking the steering head to the stiff column, but with the actuator disconnected from the forks in order to not affect their natural dynamic properties. Actually, modal analysis has been carried out both with and without the wheel: the tests with the wheel explore the actual modes that will be excited by tire forces on the running motorcycle; the test without the wheel explore the intrinsic stiffness and damping properties of the fork. Accelerations have been measured by means of a tri-axial accelerometer having the three axes oriented as follows: x-axis is aligned with the stems, y-axis perpendicular to the fork plane and z-axis as vector product between x and y. The tri-axial accelerometer has been moved to 10 different points of the forks and on 8 points of the wheel. The wheel used for the enduro fork was a 80/100-21 tire, the tire used for the super sport fork was a slick 120/70-R17. The tires were not in contact with the ground.

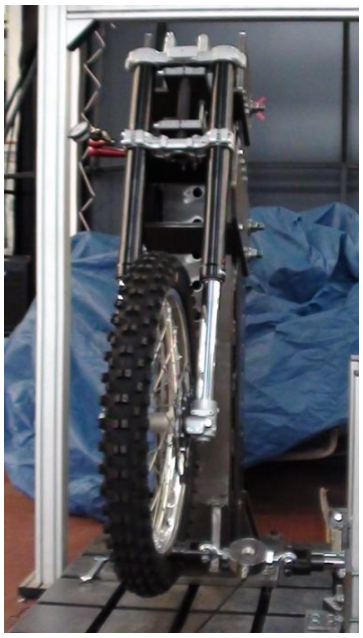

Figure 27 Front fork A on the *Mototiremeter*

4.1 Fork A

The static tests have been carried out by applying a slowly varying force (range ± 300 N) to the lowest point of the wheel. Figure 28 shows experimental results dealing with the enduro fork: the static twist axis is plotted with a thick line, the bending axis (dashed line) is the component of the twist axis perpendicular to the fork and the torsion axis (dotted line) is the component of the twist axis aligned with the fork. The large circle is the silhouette of the front wheel and the large black dot is the point of the wheel in which the force has been applied. It is clear that the twist axis is not orthogonal to the fork axis, which means that the front fork is stressed by both bending and torsion loads and the wheel twist axis is the result of bending and torsion properties of the front fork. Stiffness decomposition has been carried out according to the method previously described and the identified results are summarized in Table 10.

Dynamic measurements on front fork A have been carried out making use of the actuator and of the modally tuned hammer as well. The tests with the actuator aimed to study how the twist axis moves as a function of the frequency of excitation. The actuator has been controlled in order to produce a sinusoidal displacement with specific frequency (range 1-15 Hz) and amplitude values (range 1.5-2 mm).

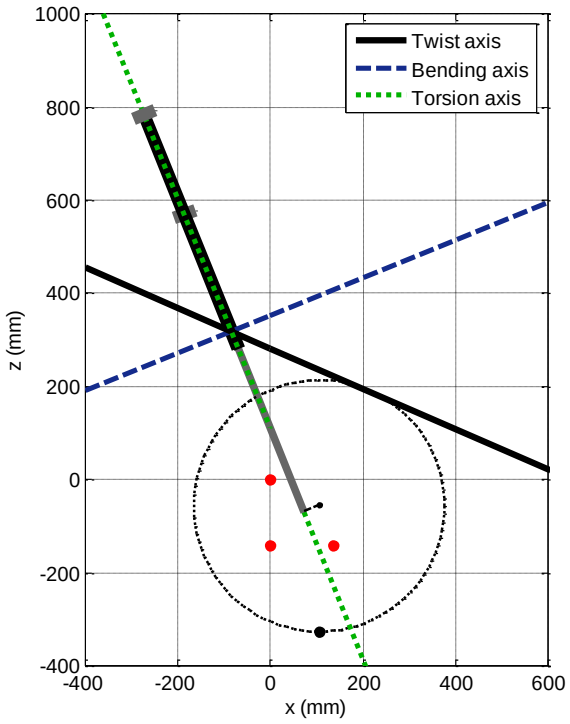

Figure 28 Twist axis for static test for the enduro fork

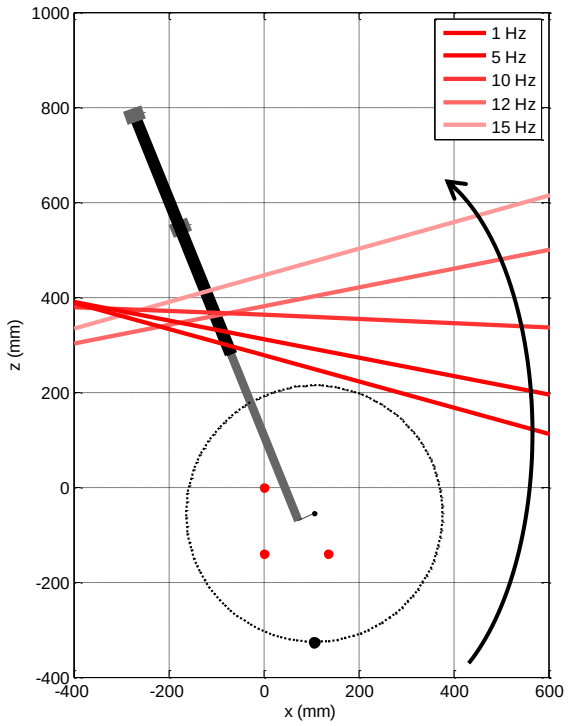

Figure 29 Evolution of twist axis position from 1 Hz (quasi-static condition) to 15 Hz, enduro fork.

Static properties	Simple method	Modal method
Lateral stiffness	56.1 kN/m	56.1 kN/m
Twist arm	0.517 m	0.517 m
Rotational twist stiffness	15 kNm/rad	15 kN/m
Bending arm	0.67 m	0.861 m
Rotational bending stiffness	28 kNm/rad	46.7 kN/m
Torsion arm	0.066 m	0.120 m
Rotational torsion stiffness	3 kNm/rad	7.4 kN/m
Inclination of the twist axis	45.5 °	45.5 °

Table 10 Stiffness parameters identified of the enduro fork: the simple method employs the bending and torsion axes assumed *a priori* (Figure 28); the modal method employs the bending and torsion axes identified with dynamic tests.

Figure 29 deals with the enduro fork and shows the evolution of the wheel twist axis position with respect to the excitation frequency. It is evident that the wheel twist axis at the lowest frequencies is very close to the one identified by static measurements. As the frequency increases the natural modes of vibration are excited and the twist axis position varies according to the arrow.

However, as explained in Chapter 1, the investigation of the dynamic twist axis carried out with a shaker excitation is limited to low frequencies (theoretically, up to 40 Hz). For a better investigation, the measurements with the three mono-axial accelerometers technique have been carried out. The measurements have been carried out after modal analysis, but are reported now for the sake of simplicity. Figure 30 shows the modal twist axes identified for the natural frequencies of the enduro front fork. It is interesting to note that at 23 Hz the modal twist axis is almost orthogonal to the front fork, which can be approximated as a simple bending beam. At 67 Hz the torsional mode occurs and the modal twist axis is almost parallel to the front fork. Those axes are somewhat similar to the ones identified with the static tests and the twist stiffness decomposition previously described.

A further elaboration of the experimental results of the test consist in the identification of its bending and torsion stiffness according to the general method employed for frames and swingarms. The twist stiffness has been decomposed into its bending and torsion components using the bending and torsion axes measured with dynamic tests (Figure 30). Results are shown in Table 10. It is worth highlighting that the bending and torsion stiffnesses identified with the modal method (which employs the modal Mozzi axes identified by means of experimental tests) are higher than the ones identified with the simplified decomposition method (which employs the assumed axes) and closer to the values presented in literature.

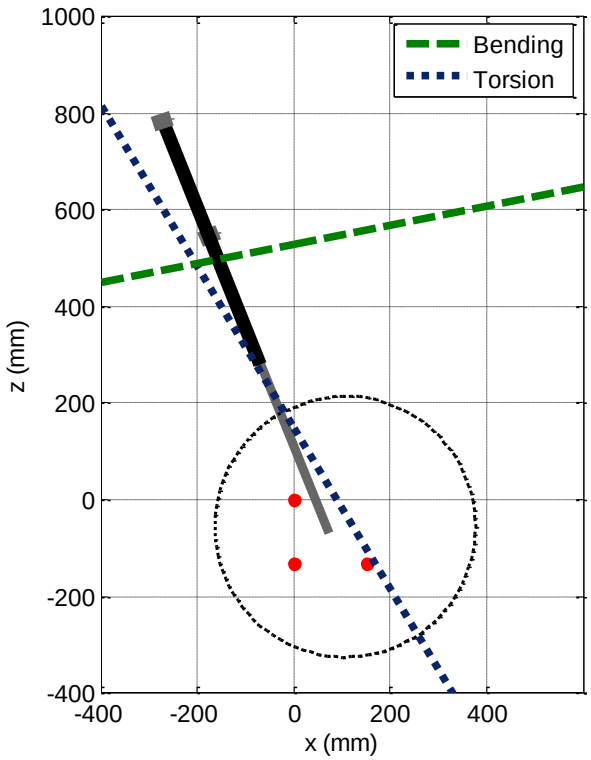

Figure 30 Bending and torsion axes identified on fork A with the three-accelerometers technique.

Successively, modal analysis has been performed on front fork A with and without the wheel. Figure 31 shows the overlays of the measured FRFs of the enduro fork in the three directions without the wheel. FRFs in the x direction (along the fork axis) show a small amplitude peak at about 20Hz, a large peak just below 40 Hz and large amplitudes with a small peak above 60 Hz. FRFs in the y direction (longitudinal) are characterized by two peaks, one just below 40 Hz and one just above 40 Hz. FRFs in the z (lateral) direction (excitation direction) show a well defined peak at about 40 Hz, which refers to the first important mode of the fork. Large amplitudes with a smooth peak are present at about 60 Hz. A quick interpretation of these data suggests that for the peak below 40 Hz the vibrations occur mostly in z (lateral) direction and for the peak above 40 Hz the vibrations occur mostly in the y (longitudinal) direction.

FRFs have been analyzed with the ICATS software. The modal shapes are displayed in Figure 32 while the modal parameters are summarized in. The first mode at 38.6 Hz is characterized by lateral deformation of the fork (z direction). The second mode at 41.2 Hz is dominated by longitudinal deformation of the fork (y direction). The last mode at 67.1 Hz occurs mostly in the y direction and it is a torsional mode of the fork, since the two stems move in phase opposition.

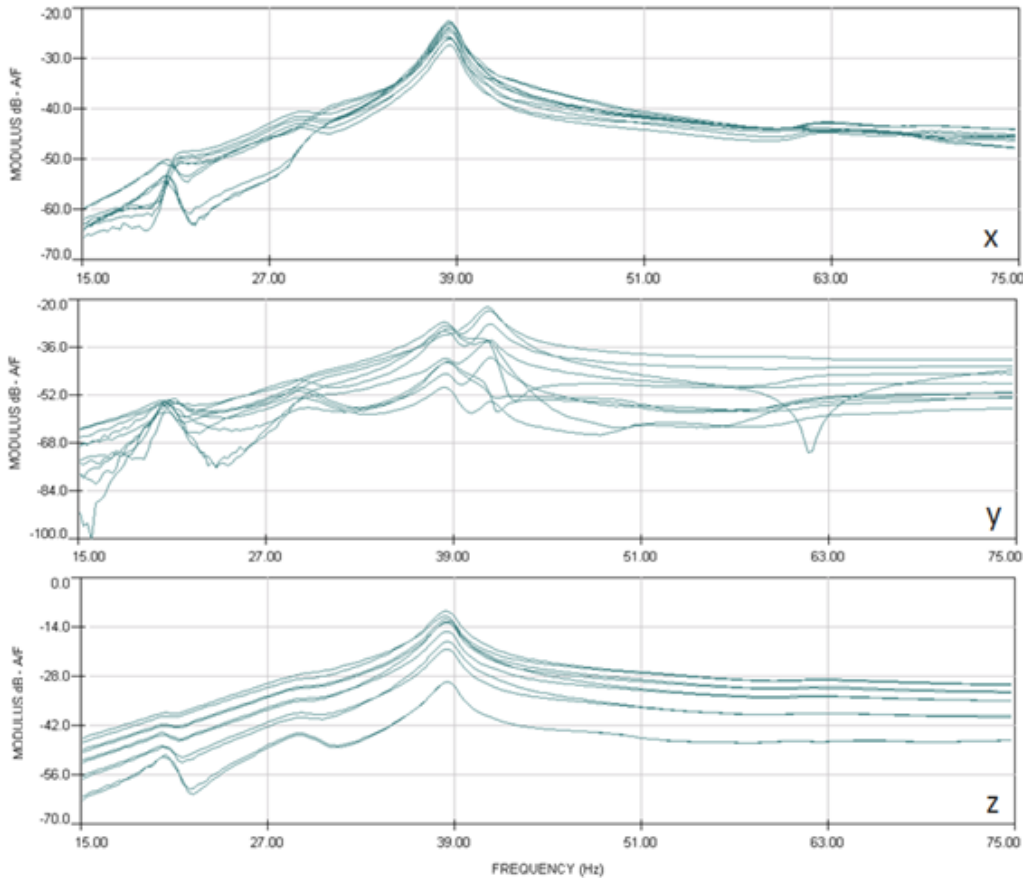

Figure 31 Measured FRFs of the enduro fork without wheel in the x, y and z directions.

#	Freq[Hz]	Viscous damping	Mode Shape
1	38.6 Hz	2.2 %	Lateral
2	41.2 Hz	1.8 %	Longitudinal
3	67.1 Hz	3.6 %	Torsional

#	Freq[Hz]	Viscous damping	Mode Shape
1	22.3 Hz	2.4 %	Lateral
2	23.5 Hz	1.4 %	Longitudinal
3	67.2 Hz	5.9 %	Wheel

Table 11 Modal parameters of the enduro fork without (left) and with (right) the wheel.

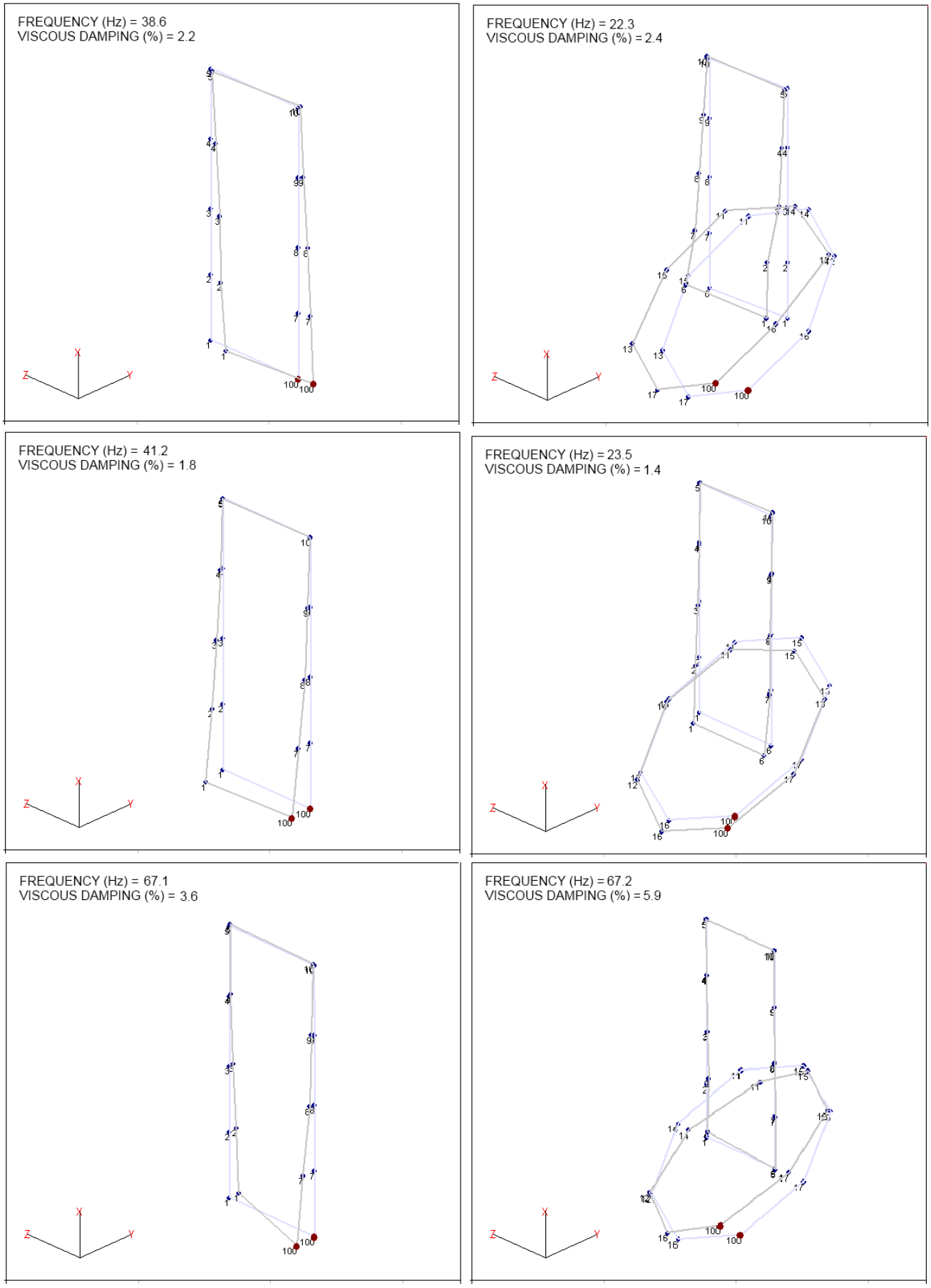

Figure 32 First modes of vibration of the enduro motorcycle's fork without (left) and with (right) the wheel.

Successively, the tire was mounted on the fork and new FRFs have been acquired. The FRFs (not shown for shortness sake) are very different from the ones measured without the wheel: the natural frequencies have drastically decreased because of the added mass and related inertia with respect to the deformation axes and the main peaks are now concentrated between 15 and 25 Hz. Another small peak occurs at about 60 Hz. The main peaks of the FRFs of the enduro fork have been identified as the first lateral and the first longitudinal modes of the motorcycle component, as shown in Figure 32. The small peak that appears in the FRFs at about 67 Hz derives from the interaction between the fork and the wheel and substitutes for the torsion mode of the fork alone. ICATS elaboration has shown that the points of the fork where the sensors are located are almost fixed, while the wheel, excited with an impact on the rim's lowest point, vibrates about its diametrical horizontal axis (Figure 32).

4.2 Development of a modally tuned fork model

In multibody codes it is typical to express a structural compliance through lumped models. The measurements carried out on front fork A have been used for developing a lumped model of the fork. The experimental results showed that, for frequencies up to 50 Hz, the most important mode of vibration is the bending mode, while the torsion mode has higher frequencies. Note that 30-50 Hz are the typical maximum frequencies of the structural modes taken into account when dealing with stability and handling simulations. Therefore, the modeling efforts are focused on the lateral (bending) modes: these vibrations are essential to a proper modeling of the motorcycle for stability analysis. Hence, a 1 DOF lumped model with bending deformability will be employed.

It is worth noting that there are different options for using experimental data (stiffness, natural frequencies, inertias) in order to create a lumped model. Three types of lumped models will be presented. The first two models recall those reported in [5] while the third is original and proposed in this thesis as an effective manner of combining static and dynamic tests while keeping the 1 DOF lumped model. Each model employs a different combination of experimental data and computed parameters, as shown in Table 12. The parameters with a small dot come from experimental data, the others are computed with mathematical formulas.

Model 1: this model employs the stiffness computed through static laboratory test located in the point where the (experimental) static twist axis intercepts the fork axis, and the vibrating inertia consists of the front wheel and the unsprung mass (measured). More precisely the bending stiffness is k_1=28 kNm/rad and is located at L_1=0.670 m from the contact point, the vibrating inertia consists of the front wheel plus the front unsprung mass and is J_1=2.085 kgm^2 (the wheel mass is 8kg, it has a diametrical moment of inertia of 0.278 kgm^2 and has a distance 0.405 m from the bending axis, while the unsprung mass is 3kg). The resulting natural frequency is fn_1=18.4 Hz, which is slightly lower than the 22.3 Hz measured through dynamic laboratory test. The damping coefficient is c_1=11.6 Nms/rad.

Model 2: the model employs a stiffness adjusted to present the experimental natural frequency with the measured wheel and unsprung inertia. In addition the stiffness is located in the point where the (experimental) dynamic twist axis intercepts the fork axis. The bending stiffness is now k_2=78.4 kNm/rad and is located at L_2=0.846 m from the contact point, the vibrating inertia consists again of the front wheel plus the front unsprung, M_2= M_1=11 kg, but the inertia is now increased to J_2=3.995 kgm^2 because the arm L is increased.

Model 3: this model employs the stiffness identified through static laboratory test placed where the (experimental) static twist axis intercepts the fork axis but the vibrating inertia is adjusted in order to give the same natural frequency measured in modal test. The bending stiffness is now k_3= 28k Nm/rad and is located at L_3=0.670 m from the contact point, the vibrating inertia consists again of the front wheel plus the front unsprung. The total mass is M_3=11kg while the inertia is now reduced to J_3=1.426 kgm^2 (by means of a pure moment of -0.67 kgm^2) to rise the natural frequency to the experimental value of fn_3=22.3 Hz. Finally, the damping coefficient is computed again to present the same damping ratio measured experimentally, c=9.6 Nms/rad.

The different front fork lumped models have been introduced in a multibody code to simulate the motorcycle stability. The other vehicle parameters as well as the DOFs of the model are described in more detail in [29]. The simulation focused on straight motion stability. The motorcycle trim is first computed by solving the nonlinear model equations given the forward speed and with null lateral and longitudinal accelerations (straight motion). Then, the nonlinear system is linearized about this trim and the state space matrices are extracted to give the well known standard formulation for linear systems:

$$\dot{x} = Ax + Bu \qquad (37)$$

Finally the eigenvalues of **A** (i.e. the system vibration modes) are computed. The elaboration is repeated at each speed to compute the vibration modes at different speed. Four cases are considered: rigid fork and forks according to model 1, model 2 and model 3. The simulated speed range is 5-40 m/s, the limited top speed being related to the power train characteristics of the bike.

Figure 33 shows the real part of the eigenvalues of the different models (i.e. on the stability) for speeds in the range 25-40 m/s where the effect is more evident for this bike. When it comes to the wobble, the rigid model is the less stable and has a critical speed of 35 m/s. On the other hand, when including flexibility with model 1 and model 3, the bike is always stable in the simulated speed range. This stabilizing effect of the flexibility on wobble is well known ([4]). It is interesting to note that model 1 and model 3 are very close to each other, while model 2 is in between models 1-3 and the rigid case, and has a critical speed of 37 m/s.

If stability of weave mode is dealt with, the rigid model is the most stable for speeds up to 37 m/s, while above this speed the models including flexibility seem more stable.

		Model 1	Model 2	Model 3
Bending stiffness	k_i (kNm/rad)	o 28	78.4	o 28
Bending arm	L_i (m)	o 0.670	o 0.846	o 0.670
Damping coefficient	c_i (Nms/rad)	11.6	26.9	9.6
Vibrating inertia	J_i (kgm^2)	o 2.085	3.995	1.426
Natural frequency	f_n (Hz)	18.4	o 22.3	o 22.3
Viscous damping	ζ_i (viscous)	o 2.4 %	o 2.4 %	o 2.4 %

Table 12 Parameters for the lumped models of the enduro fork.

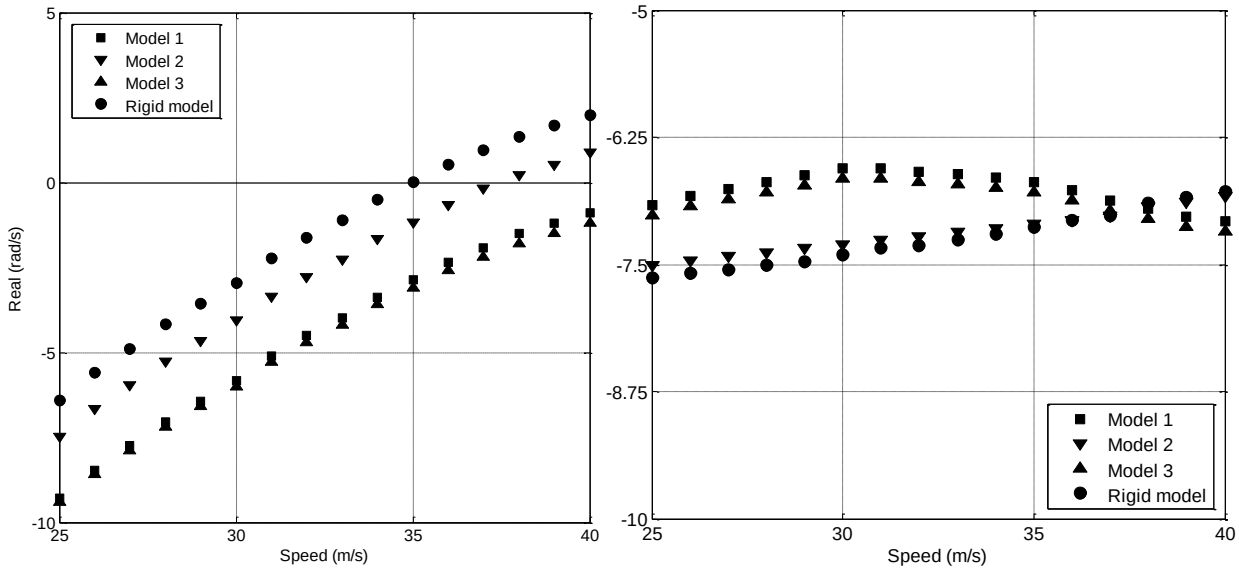

Figure 33 Free vibration modes of the enduro bike, for speed from 5 to 40m/s

4.3 Front fork B

Due to its more compact geometry and its origin from the more demanding world of super-sport motorcycles, static tests carried out on front fork B ranged from -500 to 500 N. The experimental results are shown in Figure 34. Also in this case the twist axis is not orthogonal to the fork axis, but it is worth highlighting that, even if the two forks are different and suited to different kinds of motorcycles, the positions and inclinations of the twist axes are similar. As expected, the super sport fork is much stiffer than the enduro one, as shown in Table 13.

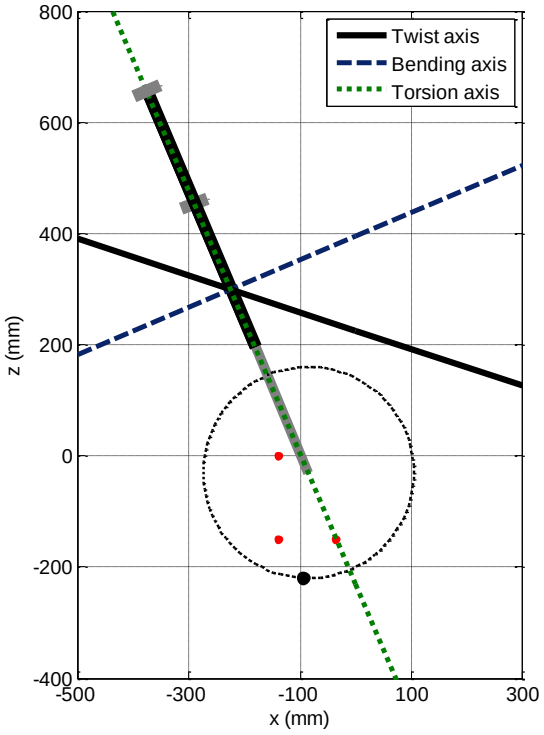

Figure 34 Twist axis for static test for the super-sport fork.

Static properties	
Lateral stiffness	109.3 kN/m
Twist arm	0.452 m
Rotational twist stiffness	22 kNm7rad
Bending arm	0.528 m
Rotational bending stiffness	35 kNm/rad
Torsion arm	0.083 m
Rotational torsion stiffness	6 kNm/rad
Inclination of the twist axis	41.2 °

Table 13 Stiffness parameters identified from the static test of the super sport fork.

Modal analysis has been the last test performed on front fork B. The identified modal parameters are summarized in Table 14. For the case of the fork without the wheel, the dynamic properties are similar to the ones of the enduro fork. The natural frequencies are vaguely higher than the ones measured on fork A due to the larger stiffness of fork B. A remarkable increase in the damping of the longitudinal mode appears. Also in the case of the fork with the wheel, the modal parameters of the super sport fork are very close to the ones of the enduro fork: natural frequencies are a bit increased due to the different fork stiffnesses; the damping coefficients are somewhat increased due to the extremely performing characteristics expected from a super sport fork. The modes of vibration of the super sport fork are not reported for the sake of shortness; however they are very similar to the ones of the enduro fork in both cases with and without the wheel.

#	Freq[Hz]	Viscous damping (%)	Mode Shape	#	Freq[Hz]	Viscous damping (%)	Mode Shape
1	42.0	2.0	Lateral	1	23.7	3.0	Lateral
2	49.4	7.5	Longitudinal	2	27.5	2.3	Longitudinal
3	63.4	7.6	Torsional	3	74.4	4.7	Wheel

Table 14 Modal parameters of the super sport fork without (left) and with (right) the wheel.

Chapter 5 – Identification of transient properties of motorcycle tires

In the framework of this research, three sets of tires have been measured. The tires of the first set have radial structure and are suited to high performance motorcycles, the sizes are 120-70-R17 (front) and 180-55-R17 (rear). The tires of the second set have diagonal structure and are suited to high wheel scooters, the sizes are 110-70-16 (front) and 140-70-14 (rear). Finally, the tires of the third set are diagonal and suited to scooters, the sizes are 120-70-12 (front) and 130-70-12 (rear). With the nominal inflation pressure and no vertical load the cross section profiles of the various tires have been measured by means of a special tool and the radii of curvature have been calculated. Figure 35 shows the measured profiles of the tires and Table 15 summarizes the calculated radii of curvature.

Front tires		Rear tires	
Size	Torus radius [mm]	Size	Torus radius [mm]
120-70-R17	43	180-55-R17	97
110-70-16	39	140-70-14	66
120-70-12	41	130-70-12	55

Table 15 : Calculated radii of curvature

In the first section of Chapter 5, the experimental relaxation lengths measured on the testing rig of the University of Padova will be presented. In the following paragraph, modal analysis results obtained on the six tires are shown. In the third paragraph, a method for the prediction of the tire relaxation lengths starting from data of modal analysis and based on a first order model of the tire is presented and discussed. Finally, the predicted values of relaxation lengths are compared with the experimental ones.

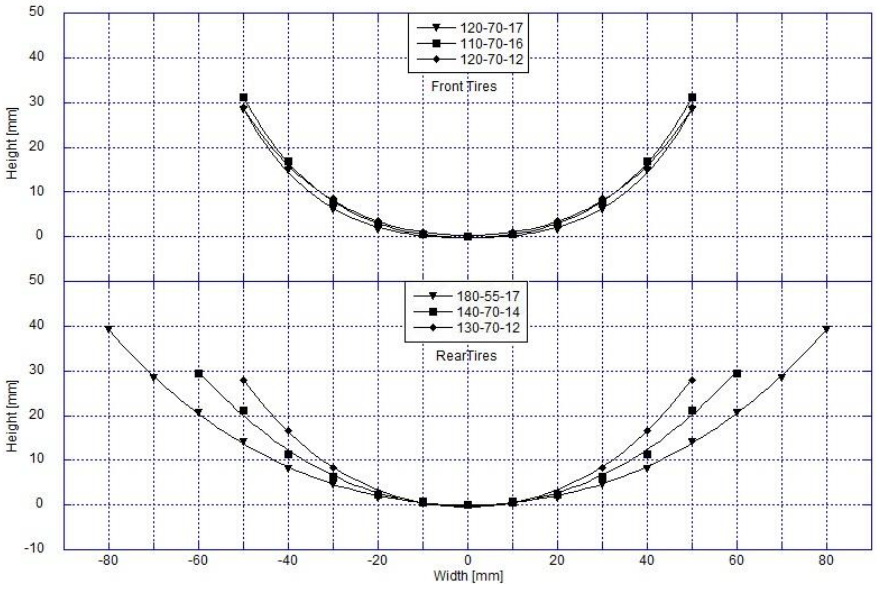

Figure 35 The cross sections of the six tested tires: experimental data and fitted profiles.

5.1 Experimental tests

The experimental methods for the measurement of tires relaxation length have been described in Chapter 2. The testing procedure included a running in period (with the tire rolling on the disk) followed by the yaw dynamic excitation carried out with constant amplitude (1.5°) and step increasing frequency, which in turn was set to 0.42, 0.84, 1.26, 1.68 and 2.10 Hz. At each frequency about 10 cycles were performed, the rolling velocity of the tire corresponded to a forward speed of 5 km/h. Tire load was set to 1500 N, inflation pressure was set to 0.5, 0.75, 1, 1.5, 2, 3 and 4 bar, these values included the nominal value (about 2 bar depending on the tire), very large values due a wrong inflation and very small values, which may occur when the tire is deflating. Figure 36 shows against pressure the relaxation lengths of four tires identified for different values of input excitation frequency. The graphs on the top refer to the set of motorcycle tires, the graphs at the bottom refer to one of the two sets of scooter tires. It is evident that relaxation length decreases as inflation pressure increases, no matter which the excitation frequency is. It is an expected result, and can be explained as follows. Increasing the tire pressure will also increase the tire stiffness; as a result, the tire will be able to respond more quickly to harmonic side-slip oscillation and the relaxation length will be smaller than the one measured for lower values of inflation pressure.

Tires don’t exhibit a clear correlation between the relaxation length and the excitation frequency in the range of frequencies here considered: the curves measured at different excitation frequencies are inclined to mingle with each other.

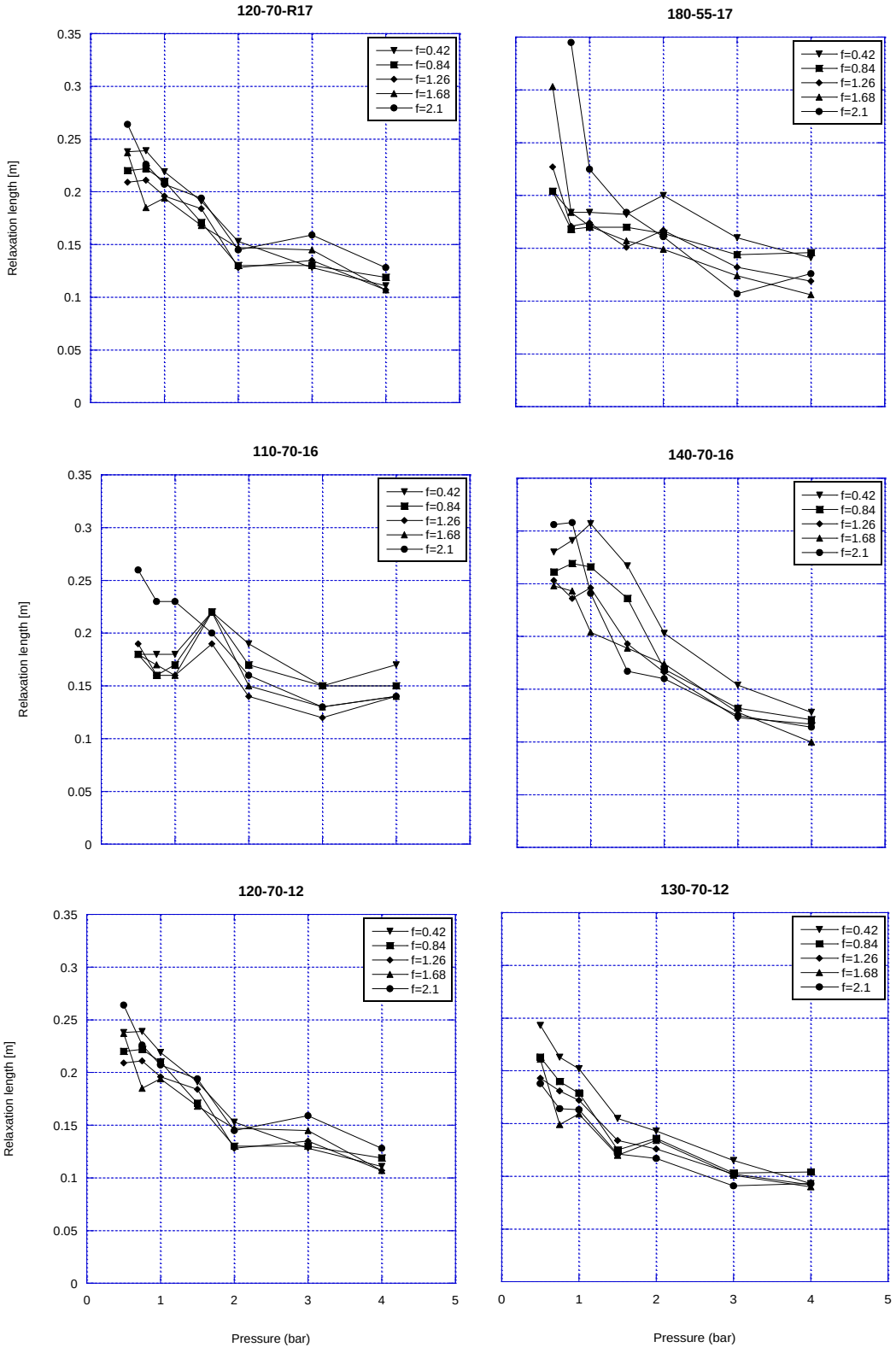

Figure 36 Experimental relaxation lengths of a motorcycle set and a scooter set of tires

5.2 Modal analysis of tires

In order to carry out modal analysis of tires, the wheels have been fixed to the stiff column of the *Motostiffmeter* so that the rims were motionless and only the tires' belts could vibrate. The hammer impulse was applied each time on a different point, while the accelerometer was fixed on the lowest part of the wheel (point 100). FRFs have been measured on six points of the wheel equidistant from each other, as shown in Figure 37.

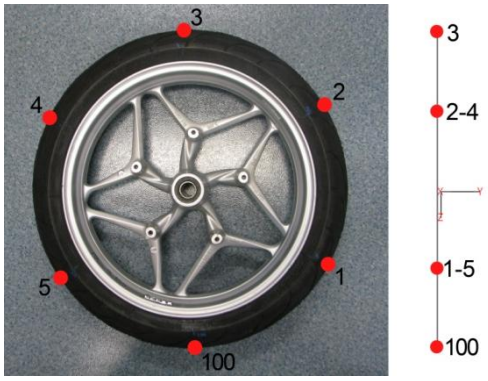

Figure 37 Measurement points for modal analysis.

For each measurement point the FRF was calculated as the ratio between the cross spectrum of input signal force and output signal (acceleration) and the auto spectrum of input signal. Figure 39, which refers to the FRFs measured on the scooter tire 110-70-16, shows the interesting effect of inflation pressure on the natural frequencies of tires. In general, natural frequencies increase with inflation pressure, which agrees with physical intuition since an increased inflation pressure stiffens the system. When inflation pressure increases the natural frequency of the first peak slightly increases and the peak value increases. The second peak (at about 100 Hz) and the third peak (at about 170 Hz) are more influenced by inflation pressure, with significant increases both in the peak value and in the resonance frequency. Also in the range of high modal density (above 300 Hz) the resonance frequencies tend to move towards higher values when inflation pressure increases. The effect on peak amplitude is less clear, because sometimes adjacent peaks tend to merge as inflation pressure increases.

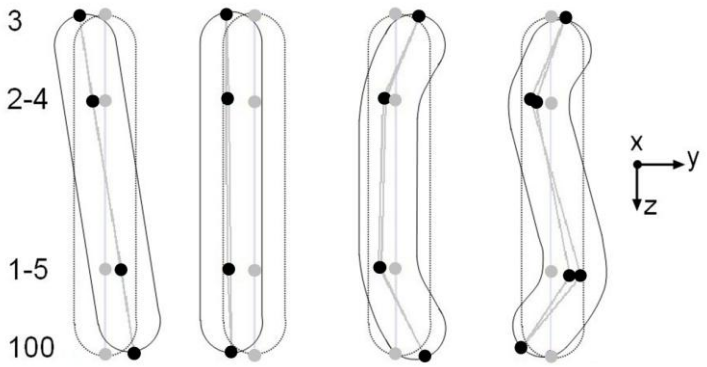

Figure 38 The identified modal shapes

Then, the modes identification has been carried out on ICATS, the identified modal shapes are shown in Figure 37. The first typical mode is a rigid belt diametrical mode, since the tire's belt vibrates about its horizontal axis. The second typical mode of the same tire is a lateral mode and it is characterized by a lateral vibration of the tire's belt with respect to the wheel's rim (rigid belt mode). The vibration of the

third typical mode exhibits a C shape, since the two points at the extremities and the four points in the middle of the wheel move in opposition. The fourth typical mode is an S-shaped mode, since even points and odd points move in opposition. The yaw mode about the vertical diameter was not identified from the collected FRFs because the accelerometer (point 100) for symmetry reasons is always located on the nodal axis of this mode.

Some observations can be drawn from a comparison of the natural frequencies and the damping coefficients identified on the six tested tires. The first four typical modes (camber, lateral, C-Shaped and S-shaped)

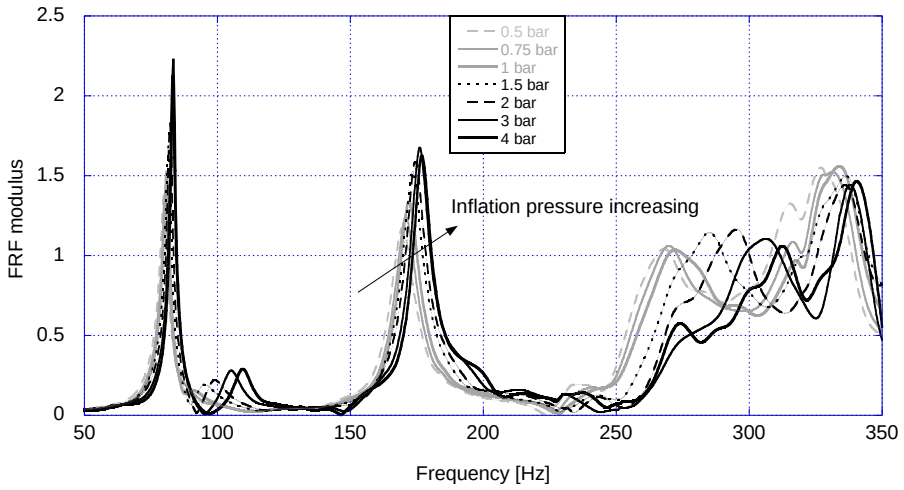

Figure 39 Measured FRFs for several values of inflation pressure, 110-70-16 tire.

essentially appear in the same order for the six tested tires, only in the small scooter tires at low inflation pressure the frequency of the camber mode is slightly higher than the one of the lateral mode. The natural frequency of the camber mode is the least influenced by inflation pressure, only the camber mode of the rear motorcycle tire, which has a large size, shows a certain sensitivity to inflation pressure. The mode with the smallest damping ratio is usually the rigid ring camber mode, only in the 110-70-16 tire the mode with smallest damping ratio is the lateral mode.

5.3 Stiffness and damping identification

The stiffness and damping properties of the tire's carcass have been identified from the measured modal properties. The tire is modeled as a thin ring that can bend out-of-plane and is elastically suspended to the rim by means of the carcass, as shown in Figure 40.

Modal shapes are normalized with respect to the amplitude of the lowest point (point 100), which is assumed equal to y_{ok} and can be described by the equation:

$$y(\varphi) = y_{ok} \cos(k\varphi) \qquad (38)$$

In which φ is the angular coordinate that defines the position of the generic ring element. If *k=0*, the rigid ring lateral mode is obtained. If *k=1* the rigid ring camber mode is obtained. Larger values of *k* give the modes with belt deformation of increasing complexity (*k=2* C-shaped mode, *k=3* S-shaped mode).

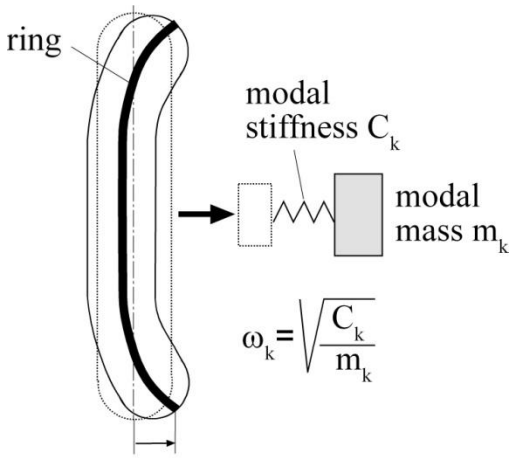

Figure 40 Modal mass and stiffness

Modal stiffness is obtained with a Raleigh-Ritz approach [32]. Modal analysis showed that the dampings of the first modes of the tire are rather small. Hence, when a vibration mode is excited in resonance condition, it is possible to assume that the maximum potential energy associated to the deformation of the carcass and the ring ($U_{k\max}$) is equal to the maximum kinetic energy of the ring ($T_{k\,max}$):

$$U_{k\max} = \frac{1}{2} C_k y_{ok}^2 = \frac{1}{2} m_k \omega_k^2 y_{ok}^2 = T_{k\max} \quad (39)$$

In which ω_k is the natural frequency, m_k the modal mass and C_k the modal stiffness (Figure 40). C_k refers to the lateral displacement of the lowest point of the ring, because modal shapes are normalized with respect to the amplitude of this point. The maximum kinetic energy can be calculated considering the velocity of the ring elements and the ring mass per unit length (μ), which is assumed constant. When the *k*-mode is excited, displacement is given by equation:

$$y_k = y_{ok} \sin\left(\omega_k t\right) \cos\left(k\varphi\right) \quad (40)$$

It follows that velocity and maximum velocity are given by:

$$\dot{y}_k = y_{ok} \omega_k \cos\left(\omega_k t\right) \cos\left(k\varphi\right) \quad (41)$$

$$\dot{y}_{k\max} = y_{ok} \omega_k \cos\left(k\varphi\right) \quad (42)$$

Therefore the maximum kinetic energy is given by:

$$T_{k\max} = \frac{1}{2} \int_0^{2\pi} \mu y_{ok}^2 \omega_k^2 \cos^2\left(k\varphi\right) r d\varphi \quad (43)$$

In which *r* is the ring radius. It follows that:

$$T_{k\max} = \frac{1}{2} \mu y_{ok}^2 \omega_k^2 r \int_0^{2\pi} \cos^2\left(k\varphi\right) d\varphi \quad (44)$$

And modal mass is given by the following equation.

$$m_k = \frac{m}{2\pi}\int_0^{2\pi} \cos^2(k\varphi) d\varphi \quad (45)$$

This integral can be evaluated for the first modes of the ring. The mass of the ring (*m*) is assumed to be a share of the measured mass of the tire. Dealing with car tires Pacejka [13] suggested to assign 75% of the tire's mass to the belt. To determine the ring's mass this percentage was slightly improved (80 %) to take into account the different shape of the tires for two-wheeled vehicles.

Finally, modal stiffness C_k can be calculated from equation:

$$C_k = m_k \omega_k^2 \quad (46)$$

In which ω_k is the natural frequency and m_k the ring mass of the k-mode. The mass of the ring is assumed to be a share of the measured mass of the tire. Dealing with car tires Pacejka [13] suggested to assign 75% of the tire's mass to the belt. To determine the ring's mass this percentage was slightly improved (80 %) to take into account the different shape of the tires for two-wheeled vehicles. Table 16 summarizes the identified stiffness parameters at nominal inflation pressure. Only in the motorcycle radial tires the C-shaped mode with ring deformation has a modal stiffness lower than the one lateral mode. The S-shaped mode always has a very large modal stiffness.

Tire	Camber	Lateral	C-shaped	S-shaped
120/70 R17	463	1906	1239	4690
180/55 R17	515	1178	978	2258
110/70 16	398	1181	1847	5357
140/70 14	222	767	3043	10851
120/70 12	343	742	2589	10494
130/70 12	360	709	2842	10318

Table 16 Modal stiffnesses for inflation pressure of 2 bar (kN/m)

Finally, the small damping coefficients of the modes can be calculated from damping ratios (ζ) according to equation:

$$K_k = \zeta_k 2\sqrt{C_k \omega_k} \quad (47)$$

5.4 Prediction of relaxation length

A specific version of the ring model [15] is considered here. Since on the testing machine of Padova University it is possible to identify the relaxation length from low speed tests with enforced rotation of the wheel about its vertical diametrical axis (yaw rotation), the input of the model is the enforced yaw rotation (Ψ_a) and the inertial properties of the ring are neglected, Figure 41 shows the block diagram of the model, equations are collected in Appendix 1.

The first block $(V - i\omega a)$ takes into account that the input yaw angle generates a side-slip angle both because it modifies the attitude of the wheel and because it generates a lateral velocity. Block $1/\sigma_c i\omega + V$ represents the effect of contact patch, σ_c being the relaxation length of the contact patch. Then there are two feedback loops. The inner feedback loop takes into account that the lateral force F_y owing to the lateral compliance of the tire generates a lateral velocity that algebraically adds to the one due to the input yaw motion. C_{yg} represents the global lateral stiffness. K_{yg} represents the global lateral damping.

The outer feedback loop represents the effect of self-aligning torque $F_{yo}t_o a$ (in which t_o is tire trail). If the tire shows finite stiffness and damping characteristics about the vertical diametrical axis, the self-aligning torque generates a yaw rotation (Ψ) of the carcass that algebraically combines with the one caused by hub rotation (Ψ_a). Since the tire is axial-symmetric, the modes of vibration about the horizontal and the vertical diametrical axes are equal and stiffness C_{zz} and damping K_{zz} can be assumed equal to the ones identified from the horizontal diametrical mode (camber mode). This is a reasonable approximation, since in the loaded tire some differences between the two diametrical modes may appear.

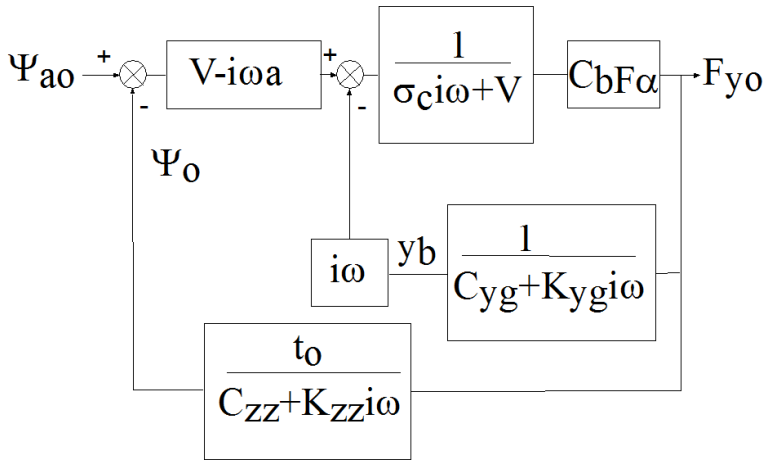

Figure 41 Block diagram of the mathematical model

It is worth highlighting that, if the effect of modal damping is taken into account, the tire does not behave as a first order system.

If the damping of the tires and the effect of self aligning torque are neglected in the ring model, a simple first order model of the tire is derived. In [34] it is shown that a very small error is introduced due to the simplification from a second order to a first order model. For a first order model, case the equation for the calculation of relaxation length σ is:

$$\sigma = am + C_{bF\alpha}(1/C_y + r_2/C_{xx} + 1/C_{res}) \quad (48)$$

The term *am* is the contribution of the contact patch in which *a* is the half-length of the contact patch and *m* is the ratio between the adhesion zone and the total length of the contact patch [13]. The second term is the contribution of the carcass stiffness: it takes into account lateral stiffness C_y, rotational stiffness C_{xx} (due to the camber mode) and a residual stiffness C_{res}. C_{bFa} is the cornering stiffness of the tire and can be measured by means of specific steady-state tests. For a detailed description of the tests methods and results, refer to Appendix 2.

In [13] the residual stiffness was introduced to ensure that the total static stiffness in the lateral direction is correct. Actually, lateral stiffness of the tire is a series of an infinite number of modal stiffnesses. The modal approach adopted in this research makes it possible to give a simple interpretation of residual stiffness: the residual stiffness takes into account the contribution of the modes of vibration different from the camber and lateral modes, e.g. the C- and S-shaped modes.

The stiffness properties identified by means of modal analysis, cornering stiffness measurements and contact patch measurements make it possible to predict relaxation length. Cornering stiffness was

measured by means of specific tests performed on the tester machine of the University of Padova (Figure 11). The motorcycle and high wheel scooter tires were tested with vertical load of 1500 N, whereas the scooter tires were tested with vertical load of 1000 N.

In order to evaluate the contribution of the contact patch half length *a,* the contact patch was measured. The tire was mounted on the tire tester machine, the tread was covered with black ink and the contact patch size was printed putting a white paper sheet under the loaded tire. Contact patch half length was calculated as one half of the length of the center line of the imprint. Figure 42 shows the measured contact patches of the front scooter tire. Table 17, which summarizes measured values, shows that *a* increases by about 50% if inflation pressure decreases from the nominal value (2 bar) to the lowest value (0.5 bar). If inflation pressure doubles, *a* decreases by about 15-20% depending on the tire.

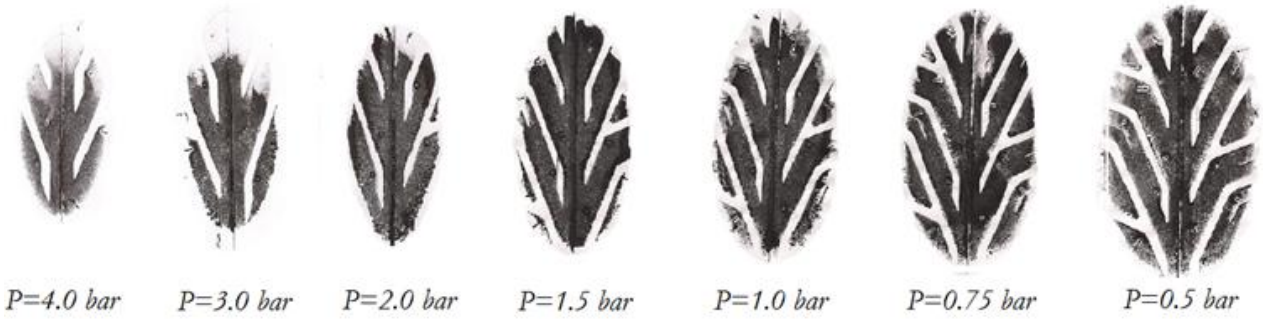

Figure 42 Variation in contact patch sizes with pressure, tire 120-70-12

Pressure [bar]	120/70 R17 a [m]	180/55 R17 a [m]	110/70 16 a [m]	140/70 14 a [m]	120/70 12 a [m]	130/70 12 a [m]
0.5	0.106	0.115	0.090	0.095	0.062	0.072
0.75	0.098	0.101	0.081	0.081	0.074	0.069
1	0.088	0.087	0.076	0.073	0.056	0.060
1.5	0.078	0.075	0.065	0.068	0.050	0.056
2	0.07	0.065	0.060	0.058	0.047	0.051
3	0.065	0.055	0.054	0.055	0.042	0.046
4	0.054	0.050	0.052	0.051	0.040	0.043

Table 17 Measured half length of the contact patch

According to Pacejka [14] the relaxation length of the contact patch can be assumed equal to a fraction m of the measured half length, constant m is given by this equation:

$$m = 1 - \frac{C_{bF\alpha}}{3\lambda FL}\tan(\alpha) \qquad (49)$$

In which F_z is vertical load, λ the friction coefficient and α the wheel side-slip angle assumed equal to 1.5°. The relaxation lengths of the tested tires are calculated by means of equation (48) setting the residual stiffness term (1/Cres) equal to the series of the modal stiffness of the C- and S-shaped modes:

$$1/C_{res} = 1/C_C + 1/C_S \qquad (50)$$

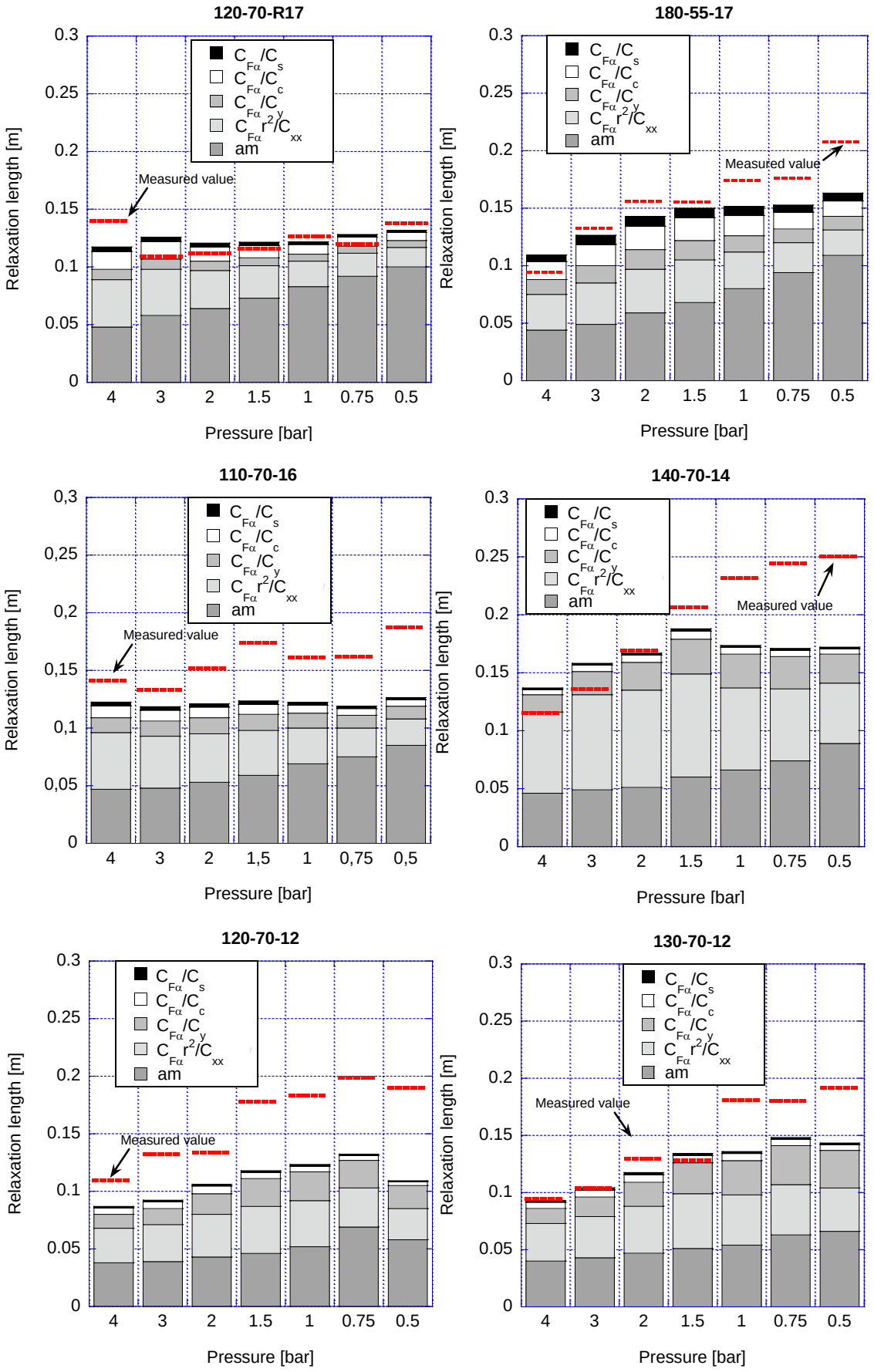

Figure 43 Predicted and measured relaxation lengths.

Results are summarized in the histograms of Figure 43. The first part of the bar (dark grey) represents the contribution of σ_c, the second part (light grey) the contribution of the camber mode, the third part (grey) the contribution of the lateral mode, the fourth part (white) the contribution of the C-shaped mode, the

last part (black) the contribution of the S-shaped mode. In general, relaxation length tends to decrease if inflation pressure increases. The contribution due to the contact patch is always important and exhibits a small but steady increase as inflation pressure decreases. In the radial motorcycle tires the contribution of contact patch is more important than in the diagonal scooter tires, which have a larger compliance and a smaller size. The most important term related to modal stiffness is the one of the rigid ring camber mode. The term due to the rigid ring lateral mode is much smaller than the one due to the camber mode. In motorcycle tires the contribution of the C-shaped mode is comparable with the one of the lateral mode, whereas in scooter tires it is a fraction of the contribution of the lateral mode. The contribution of S-shaped mode is very small in all the tested tires. The contributions of the modes with ring deformation do not show large variations as inflation pressure changes.

The relaxation lengths measured by means of experimental tests (dashed red line) are plotted in Figure 43 in order to make a comparison with the predicted relaxation lengths. Since experimental results showed that the measured relaxation lengths are almost independent from the excitation frequency (Figure 36), the dashed red line is the average of the relaxation lengths identified in the tests at excitation frequencies 0.84, 1.26 and 1.68 Hz. It is evident that relaxation length increases both in predicted and experimental values as inflation pressure decreases: a lower inflation pressure generates a decrease in the tire stiffness, hence it takes more time for the tire to follow the harmonic side-slip excitation, with an increasing in relaxation length. The graphs show that in the radial tires with inflation pressure set to the nominal value (2 bar) or values close to the nominal one there is an acceptable difference (about 20%) between predicted and measured relaxation lengths. In the diagonal scooter tires the difference is larger (30%-50%) and increases if inflation pressure decreases. In most cases the measured value is larger than the predicted one. It is assumed that the cause of deviation of predicted values from measured values of relaxation length is the incompleteness of the modal model. Actually only the two modes with ring deformation having the lowest natural frequencies were identified and taken into account in the model, but higher order modes may influence the deformability of the tire.

Chapter 6 – Identification of the static and dynamic properties of bicycles and bicycles components

In the framework of this Ph. D. some experimental activities have been carried out on bicycles and bicycles components.

The study of bicycles and bicycle frames has been focused on the analysis of their dynamic properties, with a specific interest in their modes of vibration. Modal analysis of an ordinary bicycle with steel frame has been carried out, the results have been compared with the modal properties of three other bicycles available in our lab database. The three bicycles are one sport bicycle with ergal frame and two sport bicycles in carbon-fiber frame.

Two bicycle front forks have been tested: the first one was an expensive carbon fork suited for a racing bicycle, the second one was a simple steel fork that can be mounted in an ordinary city bike. The forks are shown in Figure 48 and their weights are 0.393 kg and 1.336 kg, respectively. The forks have been tested by means of modal analysis, both with and without the wheel. It is worth remembering that the mass of the wheel can affect deeply the properties of the front fork. The measurements without the wheel have been carried out on a two dimensional mesh of test points in which the blades of the fork are described by four points equidistant from each other. A ninth point has been added close to the fixation point to check the stiffness of the locking system. During the tests without the wheel, a fake hub has been added to the wheel hub in order to avoid relative motions between the blades of the fork. During the tests with the wheel, eight points (equidistant from each other) have been added to the mesh in order to sketch the wheel and to study its dynamic behavior. A further elaboration of modal analysis data allowed the identification of the bending and torsional stiffnesses of the forks. Those properties have been used in order to carry out some

numerical simulations on a mathematical model developed in order to take into account also the compliance of the front fork. The equations of the model are presented in Appendix 3.

6.1 Modal analysis of bicycles

Modal analysis of bicycles has been carried out keeping the vehicles in equilibrium by means of soft elastic ropes, connected to the two-wheeled vehicle in three different points: steer, middle of the top tube and seatpost. Two small sheets of sandpaper have been placed under the wheels in order to simulate the conditions of friction normally found on the road surface, and thus to prevent any oscillatory motions affected by the sliding of the tires on the floor. It is very important for the dynamic analysis of the bicycle to carry out the tests with the correct tire pressure: in the sport bicycles the tires have been inflated until reaching a pressure of 7 bar, in the utility bicycle inflation pressure is set to 4 bar. FRFs have been measured on 9 points of the frame and 12 points of the fork blades. The larger density of measurement points in the forks is motivated by the importance and complexity of this sub-system. The bicycles have been excited with an out-of-plane hammer impact on the hub of the rear wheel (point 100). The tri-axial accelerometer has been moved to the different points of the mesh and had the three axis oriented as follows: x axis pointing upwards, y axis aligned with the bicycle traveling direction and z axis as the vector product of x and y.

Figure 44 The measurement points for modal analysis

Figure 45 shows the overlays of the moduli of the FRFs measured on the steel bicycle. Frequency axis ranges from 0 to 75 Hz because higher frequencies are scarcely interesting from the point of view of bicycle stability, safety and comfort. FRFs measured on the other bicycles have some common features, which are due to typical vibration modes of bicycles, and some different aspects, which are specific for each bicycle. The common features are:

A small peak at very low frequencies (1-2 Hz), which is due to the suspension system.

A low frequency peak at 11-12 Hz, followed by a medium-sized peak.

A very sharp peak at 37-38 Hz, with some smaller peaks on both its sides.

Some small peaks in the frequency range from 40 to 75 Hz.

Some of these peaks refer to characteristic modes of the frame or the fork, others are typical modes due to the coupling of the two components. The existence of a coupling is confirmed by the presence of a peak on the FRFs of both frame and fork points.

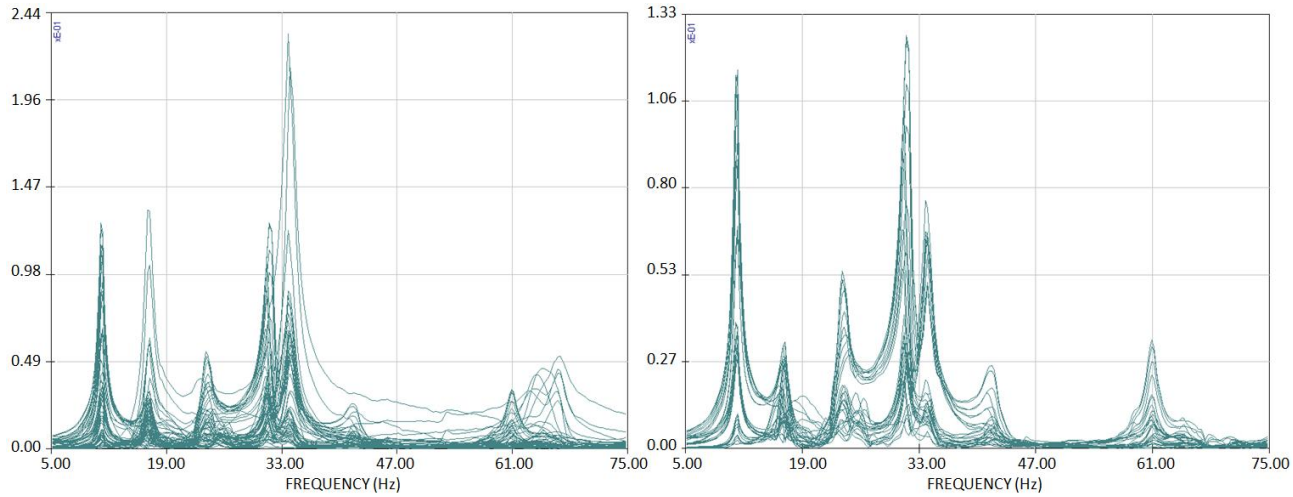

Figure 45 Overlays of FRFs measured on the steel bicycle: all points (left) and only fork ones (right.)

Then, FRFs have been processed by means of the ICATS software in order to perform the modal parameters identification. Table 18 summarizes the modal parameters of the common modes of the four bicycles and includes a short description of the identified modes. f is the natural frequency and η is the structural damping coefficient.

The first two typical modes, which are associated to the peaks at 11 – 12 Hz and 17- 18 Hz respectively, are characterized by large deflections of the tires and nearly rigid behavior of the fork and frame. The mode at 11 - 12 Hz is characterized by a rigid yaw rotation of the rear frame and steer rotation of the front frame; the mode at 17 – 18 Hz is dominated by a rigid roll rotation of front and rear frame about a nodal line, which is close to the top tube of the bicycle. The modal shapes of the identified modes are shown in Figure 46, which displays the displacement of the measurement points with respect to the 0-deflection shape of the bicycle.

The third typical mode appears at 24 – 26 Hz and is connected to a medium-sized peak which is more evident in the FRFs of the fork. This mode is very important for bicycle stability, because it is essentially a torsion mode in which the tips of the fork move in phase with the crank set and in opposition with seat-stays and chain-stays. This relative motion is due to lateral bending of the fork and torsion of the frame.

The fourth typical mode corresponds to the high peak at about 35 Hz. It is essentially the first bending mode of the frame. The shape of this mode is similar to the one of the first bending mode of a free-free beam, with two nodal lines (the first between the seat tube and the head tube, the second between the seat tube and the rear hub) an three antinodes (the head tube, the seat tube and the rear hub).

Mode	Steel		Ergal		Carbon Monocoque		Carbon Banded		Description
	f [Hz]	η %	f [Hz]	η %	f [Hz]	η %	f [Hz]	η %	
1	11	8.5	12.8	7.7	11.5	6	11	8.5	Tire dominated - Yaw
2	17	5.3	18.5	4.4	17.8	5.5	17	5.3	Tire dominated - Roll
3	24.1	5.7	25.7	3.6	23.7	5.5	24.1	5.7	Torsion
4	33.9	3.7	34.4	4.1	34.9	3.9	34.2	5.9	First bending
5	41.6	1.7	43.2	1.5	43.5	3.8	45.8	1.3	Fork lateral
6	64.1	4	62.3	1.5	65.3	3.6	72.8	3.9	Second bending
7	66.5	2.7	71.0	1.6	72.8	2.8	-	-	Seat tube, rear frame

Table 18 Modal parameters of the common modes of the tested bicycles.

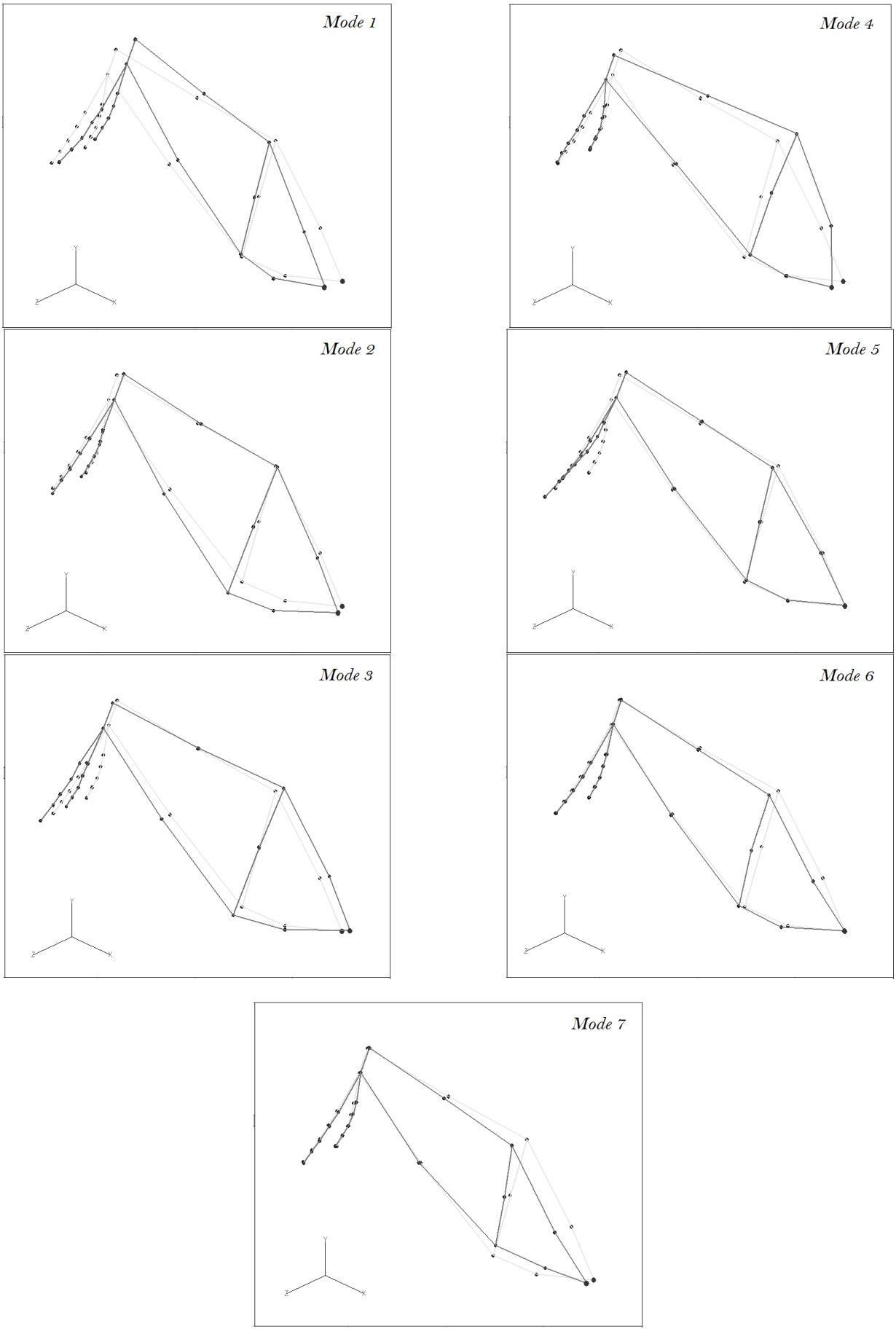

Figure 46 The seven common modes of the tested bicycles in the range 0-75 Hz

The FRFs of the tested bicycles after the main peak show a minor peak at about 40-43 Hz. This peak corresponds to the fifth typical mode, which is characterized by fork deformation in the lateral direction and torsion deformation of the frame with the head and the saddle moving in opposition.
The band of frequency between 50 and 75 Hz is the most influenced by bicycle material and construction technology. The mode at 62-65 Hz that appears in the steel, ergal and carbon bicycle with monocoque frame can be considered the sixth typical mode. It is essentially a bending mode of the frame characterized by negligible displacements of the front fork and head tube, large displacements of the crank set and of the rear hub, which moves in opposition with respect to the crank set. In the carbon bicycle with banded frame this mode does not appear because in this range of frequency there is still a strong interaction between the fork and frame and there are some specific modes with large displacements of the fork.
The mode at 70 – 73 Hz in the carbon and ergal bicycles and at 66 Hz in the steel bicycle essentially shows large deformation of the seat tube, chain stays and seat stays. It can be considered the seventh typical mode of the bicycles and is shown in the last picture of Figure 46.

The most important effects of material properties and construction technology can be summarized as follows. The utility bicycle, which is heavy and not designed for high speeds, shows below 50 Hz a significant interaction between bending deformation of the frame and lateral deformation of the front fork, which has a simple circular cross section and is not as stiff as in the other bicycles. This bicycle, instead of having the typical bending mode flanked by the typical torsion and fork modes, shows three modes with important fork deformation and a bending mode of the frame which is different from the typical bending mode of the other bicycles, since it shows some deformation of the fork with two nodal points at the hub of the front wheel. At 61.19 Hz the utility bicycle exhibits a mode with large deformation of the fork near the head tube (Figure 47), this mode in similar to the typical high frequency fork mode that in the other bicycles appears above 100 Hz.
The comparison between the modal properties of the two sport bicycles with carbon frame highlights that in the medium range of frequencies (50 – 75 Hz) the bicycle with banded frame has a larger density of modes and a shows a larger interaction between the modes of the fork and frame. Nevertheless the frequencies of the main peaks show only small variations. The banded frame leads to an increase in the damping of the most important modes. In particular the increases in the damping of the typical torsion mode (from 5.5 to 6.4 %) and in the damping of the typical bending mode (from 3.9 to 5.9 %) are useful for dampening the dangerous high speed wobble oscillations.

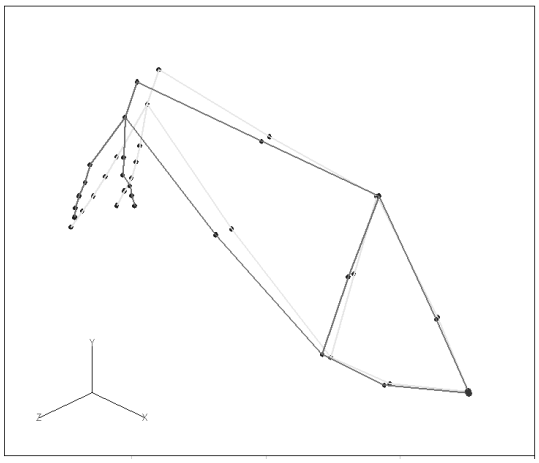

Figure 47 The mode at about 61 Hz on the steel bicycle.

6.2 Modal analysis of the carbon front fork

The FRFs of the carbon fork measured without the wheel show two important peaks at about 65 and 95 Hz and a smaller peak at about 200 Hz. The first peak corresponds to the lateral mode, in which the fork blades move in the z direction; the second peak corresponds to the longitudinal mode, in which the fork blades vibrate in the y direction. The third smaller peak corresponds to the torsional mode, in which the fork blades move in opposition in the y direction. The mode shapes are shown in Figure 49, in which red color represents the largest vibration amplitude and blue color the smallest.

The FRFs measured with the wheel show some peaks in a frequency range lower than the one of the peaks of the FRFs measured without the wheel. Two small peaks are close and localized at about 20 Hz, a very high peak appears at about 30 Hz. A fourth peak appears at about 80 Hz. The first peak corresponds to the torsional mode of the fork blades, as shown in Figure 50. The wheel follows rigidly the deformation of the blades and therefore displays a large deformation in the outer points. The second peak is due to the lateral mode, while the third peak corresponds to the longitudinal mode. The fourth mode is the diametrical mode of the wheel and is shown in Figure 50: the vibration is localized on the points of the wheel, which rotates about its horizontal axis.

Figure 48 The tested front forks: carbon fork with the wheel (right) and steel fork (left).

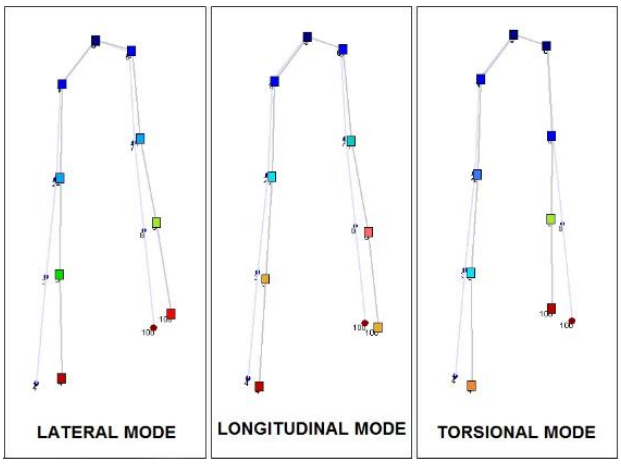

Figure 49 The modal shapes of the carbon fork without the wheel.

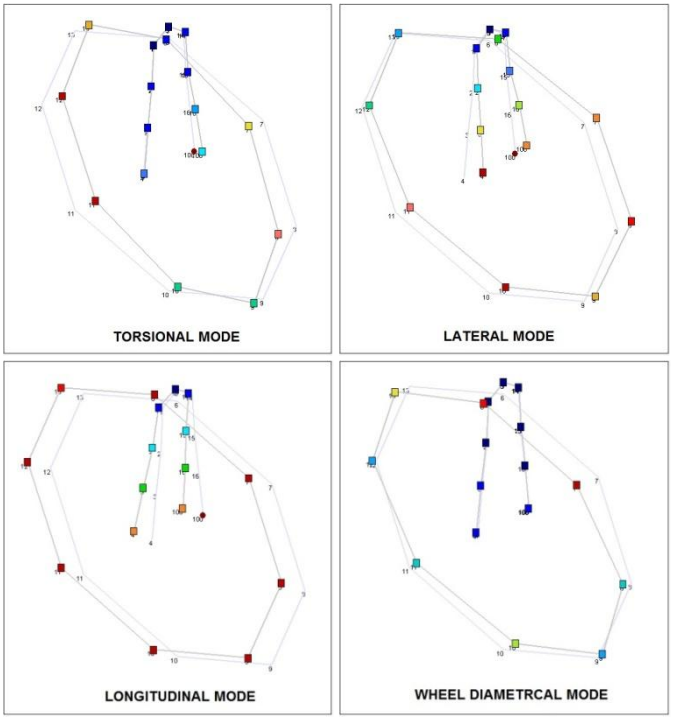

Figure 50 The modal shapes of the carbon fork with the wheel.

		Carbon fork		Steel fork	
#	Mode	f [Hz]	η [%]	f [Hz]	η [%]
1	Lateral	64	2.5	84.7	3.13
2	Longitudinal	94.1	2.57	83.4	2.69
3	First torsional	191.2	7.57	214.1	2.23
4	Second torsional	/	/	230.1	1.85

Table 19 Modal parameters of the forks without the wheel

		Carbon fork		Steel fork	
#	Mode	f [Hz]	η [%]	f [Hz]	η [%]
1	Torsional	19.3	10.04	29.7	2.22
2	Lateral	21.3	4.24	30.5	2.79
3	Longitudinal	31.7	2.93	35.1	2.42
4	Wheel diametrical	80.4	1.49	80.2	1.67

Table 20 Modal parameters of the forks with the wheel

6.3 Modal analysis of the steel front fork

The modal analysis of the steel fork has been carried out with the same methods of the carbon fork. For the tests carried out without the wheel, the lateral and longitudinal modes occur in inverse order with respect to the carbon fork. However, it is worth noticing that the natural frequencies of the first two modes are extremely close, which makes the measurements and the identification of the modal properties particularly tricky. This phenomenon can be explained as follows: the blades of the steel fork display a circular section, also with the coupling of the wheel hub the stiffnesses in the lateral and in the longitudinal directions are similar. The blades of the carbon fork, on the contrary, present an elliptical section, with the major axis oriented in the traveling direction. The moment of inertia of the elliptical section about its major axis is

smaller than the moment of inertia about its minor axis. The stiffness in the traveling direction is larger than the stiffness in the lateral direction.

Also for the steel fork, the torsional mode occurs at high frequency (about 200 Hz). However, two close peaks can be observed in the range of frequency 200-230 Hz, which correspond to the first two torsional modes. In the mode at 214.1 deformation is localized mainly the lower tips of the fork, on the contrary in the mode at 230.1 Hz deformation involves the whole fork blade.

For the tests with the wheel, it is worth noticing that the four identified modes occur in the same order of the ones identified on the carbon fork. The results of modal analysis carried out on the forks are summarized in Table 19 and Table 20.

6.4 Torsional stiffness and damping identification

This paragraph shows the methods used for identifying the torsional stiffnesses of the carbon and steel forks using the data obtained from modal analysis. First, torsional stiffness k_γ is identified using the data obtained from the tests on the fork with the wheel. Since in resonance conditions the system behaves as a 1 DOF system, stiffness can be calculated according to the simple equation:

$$k_\gamma = (2\pi f_{tors})^2 I_{tors} \quad (51)$$

In which f_{tors} is the natural frequency of the torsional mode. The inertial term I_{tors} takes into account both the inertia of the wheel and the inertia of the fork about the torsion axis. The torsion axis is assumed to be roughly equal to the steering axis owing to symmetry considerations. The inertia of the wheel has been calculated considering the wheel as a ring of radius r_F and mass m_F. The inertia of the fork has been calculated concentrating the fork mass in two point masses equivalent each one to one sixth of the global fork mass and vibrating on the tips of the blades. This approach is commonly used to take into account in a simple way the distributed mass of elastic elements [33]. The global inertia is:

$$I_{tors} = I_{fork} + I_{wheel} = 2\left(\frac{1}{6} m_{fork} d^2\right) + m_F r_F^2 \quad (52)$$

where *d* is the distance between the blades extremity and the torsion axis (steering axis) and m_{fork} is the global mass of the fork.

Then, the torsional stiffness of the fork is identified also using the results of the modal analysis carried out on the fork alone. In this configuration, the inertia of the wheel has been replaced with the inertia of the fake hub, calculated according to the formula of a cylinder:

$$I_{hub} = \frac{1}{12} m_{hub} \left(3 r_{hub}^{\ 2} + l_{hub}^{\ 2}\right) \quad (53)$$

In which m_{hub}, r_{hub} and l_{hub} are the mass, the radius and the length of the hub respectively.

For the carbon fork the torsional stiffnesses identified considering fork with the wheel and alone are 1208 Nm/rad and 1253 Nm/rad respectively. The good agreement between the two values confirms the validity of the method.

The methods used for identifying the torsional stiffness of the carbon fork have been applied to the steel fork as well. The elaboration of data obtained from the modal analysis of the steel fork with the wheel by means of equation (51) gives a torsional stiffness of 2901 Nm/rad.

Parameter	Value
Carbon fork mass	0.393 kg
Steel fork mass	1.336 kg
Hub mass	0.094 kg
Wheel mass	1.334 kg
Hub length	0.225 m
Hub radius	0.004 m
Wheel radius	0.350 m

Table 21 Inertial parameters for the identification of the forks' stiffness.

The analysis of data obtained from the fork alone is more difficult, because two torsional modes have been identified at close frequencies (Table 19). For each mode, a torsional stiffness (named $k_{\gamma 1}$ and $k_{\gamma 2}$) has been identified with the same method already showed for the carbon fork with the hub. Then, according to the modal summation approach [10], the global torsional stiffness has been calculated as the equivalent stiffness of the two torsional stiffness $k_{\gamma 1}$ and $k_{\gamma 2}$ in series:

$$k_{\gamma} = \frac{1}{1/k_{\gamma 1} + 1/k_{\gamma 2}} \tag{54}$$

The torsional stiffness identified for the steel fork alone is 1938 Nm/rad, this value is not very far from the one identified for the carbon fork alone. Inertial parameters used in the previous formulas are shown in Table 21.

Once the torsional stiffness has been identified, starting from modal analysis data with the wheel, the damping coefficient of the torsional mode has been calculated by means of the equation:

$$c = \zeta c_c \tag{55}$$

In which ζ is the viscous damping ratio (half of the hysteretic damping identified with ICATS) and c_c is the critical damping, it is given by:

$$c_c = 2\sqrt{k_{\gamma} I_{tors}} \tag{56}$$

The damping coefficient identified for the carbon fork is 1.0 Nm/(rad/s), the damping coefficient identified for the steel fork is 0.3 Nm/(rad/s).

6.5 Bending stiffness and damping identification

In this paragraph a technique for evaluating the bending stiffness of the tested bicycle forks starting from the results of modal analysis is presented. Also in this case, the bending stiffness is calculated according to equation of a resonating 1 DOF system:

$$k_\beta = (2\pi f_{bend})^2 I_{bend} \quad (57)$$

In which is f_{bend} the natural frequency of the lateral (bending) mode and I_{bend} is an inertial term which depends on the measurement configurations. In the case of the fork with the wheel, I_{bend} is given by:

$$I_{bend} = 2\left(\frac{1}{6} m_{fork} {h_W}^2\right) + m_F {h_W}^2 + \frac{1}{2} m_F {r_F}^2 \quad (58)$$

In which the first term is the inertia of the fork about the bending axis, the second term is the inertia of the wheel about the bending axis and the third term is the pure moment of inertia of the wheel (considered as a thin ring). In the case of the fork alone, I_{bend} is equal to:

$$I_{bend} = 2\left(\frac{1}{6} m_{fork} {h_W}^2\right) + m_{hub} {h_W}^2 + \frac{1}{2} m_{hub}\left(3{r_{hub}}^2 + {l_{hub}}^2\right) \quad (59)$$

In which the first term is the inertia of the fork about the bending axis, the second term is the inertia of the hub about the bending axis and the third term is the moment of inertia of the hub.

The problem here is to measure the value of h_W, which is the distance between the tips of the fork and the bending axis and is necessary for computing the inertial terms. A standard modal analysis doesn't allow to identify the exact position of the bending axis and the impulsive analysis with the reference metal plate and the three mono-axial accelerometers described for motorcycle components cannot be employed in the case of a bicycle fork, because the mass of the pale is not negligible with respect to the mass of the fork and can alter its dynamic properties. Moreover, the bending axis cannot be identified on symmetry considerations as it was possible for the torsion axis. A simple method for identifying the bending axis position from the two sets of measurements has been adopted: two stiffness curves using h_W as a variable parameter have been computed. The former curve is for the fork with the wheel, the latter is for the fork alone. Since the forks must have the same stiffness both with and without the wheel, the correct value of h_W is identified by the intersection of the two curves. h_W values range from 0 (tips of the blades) to 0.460 m (lower jaw fixing point). The other parameters used in the formulas have been summarized in Table 21.

Taking into account the stiffness curves calculated for the carbon fork, the intersection point between the two curves is found at a distance of 0.383 m from the tips of the fork. The corresponding stiffness value identified for the carbon fork is equal to 5326 Nm/rad. Similar calculations carried out for the steel fork led to a bending stiffness of 5635 Nm/rad. These values are in good agreement with the ones presented in [31].

Once the bending stiffness has been identified, from data obtained by modal analysis with the wheel, the damping coefficients of the lateral mode have been calculated by means of the equation (55). In this case, ζ is the viscous damping ratio (half of the hysteretic damping identified with ICATS) and c_c is the critical damping of the bending mode:

$$c_c = 2\sqrt{k_\beta I_{bend}} \quad (60)$$

The damping coefficient identified for the carbon fork is 1.6 Nm/(rad/s), the damping coefficient identified for the steel fork is 0.8 Nm/(rad/s). The identified values of damping and stiffness have been introduced in

a bicycle model developed in order to take into account the front fork flexibility, a detailed description of the model is given in Appendix 3.

6.6 Numerical simulation

The bicycle model equations with fork compliance have been implemented in MATLAB codes. To perform stability analysis the complex eigenvalue problem has been solved. The geometric and mass parameters of the bicycle have been set equal to the ones of the reference bicycle presented in [30], but the stiffness and damping properties of the steel fork that have been identified in the present research have been added.

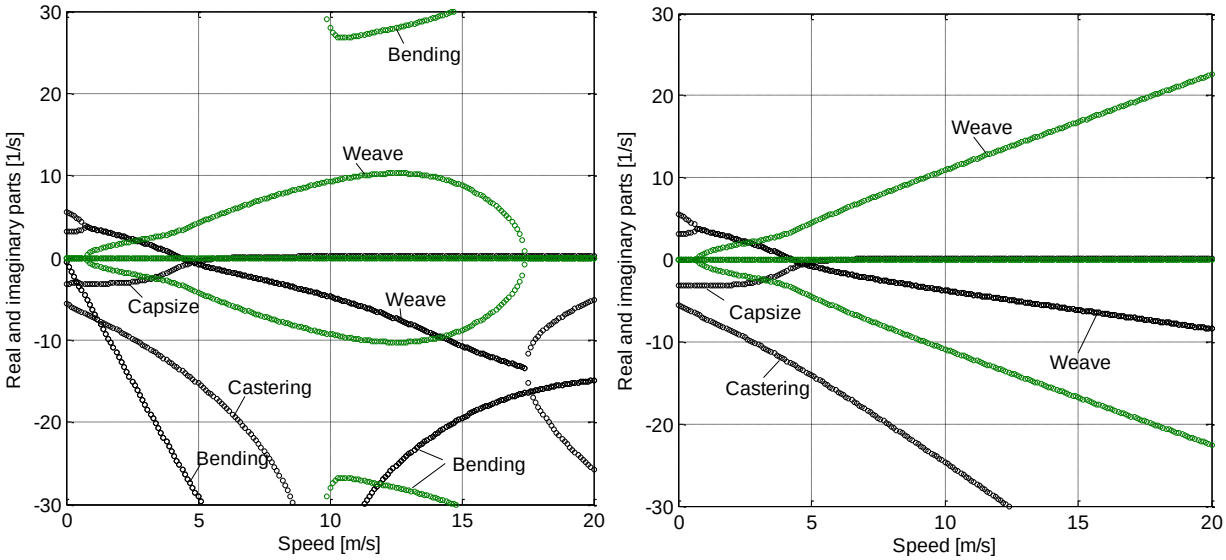

Figure 51 Eigenvalues of the model with bending stiffness and damping (left, h_w=0.21), and eigenvalues of CWBM (right) blue dots real parts, purple crosses imaginary parts

Figure 51 deals with the effect of fork bending and shows against forward speed the real parts (dots) and the imaginary parts (crosses) of the calculated eigenvalues. For comparison, the real and imaginary parts of the Carvallo and Whipple bicycle model are reported. The most evident effect of the introduction of bending compliance is the modification of weave mode at high speed. In the CWBM weave at high speed remains a complex mode with increasing real and imaginary parts. When bending compliance is introduced, weave mode disappears above a certain speed (17 m/s in the case here considered) and is replaced by a couple of modes with real negative eigenvalues. The former has an increasing (in modulus) negative eigenvalue. The latter decreasing (in modulus) negative eigenvalue, which eventually becomes positive (instability) at very high speed, which is not compatible with a bicycle. It is worth highlighting that disappearance of weave at high speed was also shown by the simulations carried out in [31] considering both tire mechanics and fork bending. Since the simulations here presented consider only the effect of fork bending, the disappearance of weave at high speed can be considered a typical effect of fork bending. The second effect of the introduction of fork bending is the appearance of a new complex mode, which is dominated by steer rotation and front fork bending. The imaginary part of the eigenvalue of the new mode (which is the damped natural angular frequency) is always larger than 27 rad/s. The real part of the eigenvalue of the new mode (which is related to damping) is small at zero speed, then it increases, reaches a maximum and decreases again. The self-stability range extends from 4.4 to 6 m/s and is very similar to the one predicted by the CWBM.

The effect of fork torsion on bicycle stability is analyzed in Figure 52. The simulation shows that fork torsion is almost decoupled from the other modes and generates a complex mode with high frequency. With the

torsion stiffness and damping values identified form the modal test with the fork alone, the eigenvalue of the torsion mode at 5 m/s is -56±455 i, only the real part appears in Figure 52. The other modes (capsize, weave and castering) are similar to the ones of the CWBM.

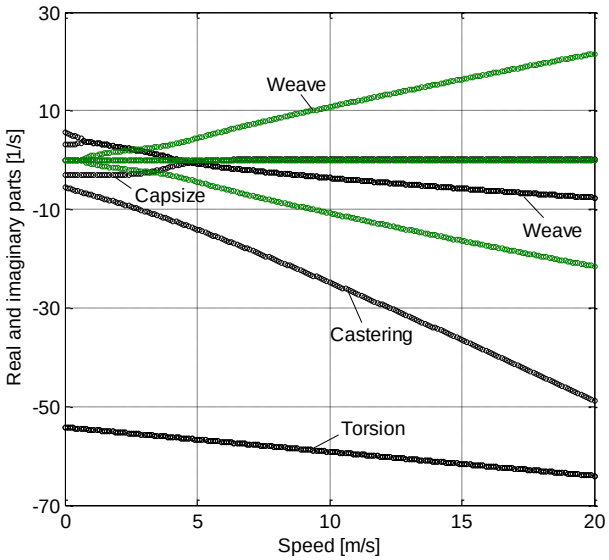

Figure 52 Eigenvalues of the model with torsion stiffness and damping, blue dots real parts, purple crosses imaginary parts.

Chapter 7 – Identification of steady-state properties of wheelchair tires

In the framework of this research, two typical wheelchair tires produced by two different manufacturers have been tested, in the following they will be named tire A and tire B. Their size is 24 x 1.3/8 inches (37-500 ETRTO) and maximum inflation pressure is 5 bar.

7.1 Experimental tests

First, both tires were tested in a reference condition with vertical load 400 N, inflation pressure 4 bar and disc speed 4 km/h. Side slip angle (α) ranged from 0° to 5°, this range includes both normal road operations (α < 1°) and rough maneuvers with large side slip angles. Camber angle (γ) ranged from 0° to 10° to include a wide set of possible fittings of the wheels on the chair. Then, tires have been tested in conditions different form the reference ones: the inflation pressure has been reduce to 2 bar, the load has been increased to 600 N and the speed of the disk has been reduced to 2 km/h. All the combinations that can be obtained by varying these three parameters have been taken into account.

Results of these tests are represented in Figure 53 in terms of normalized forces and torques: a normalized force is a measured force divided by the vertical load, whereas a normalized torque is a measured torque divided by the vertical load. The curves of the wheelchair tires are compared with the ones of a high performance bicycle tire (size 37-622 ETRTO) tested at the same value of inflation pressure, vertical load and speed.

The curves of normalized side slip force show that this component of the lateral force increases in monotonic way with side slip angle. In the side slip range here considered no saturation phenomenon takes place; it is worth highlighting that also in car tires saturation takes place for higher values of side slip angle [13]. Tire A exhibits for every angle of side slip larger values of force than tire B and a larger cornering

stiffness (the slope of the curve near the origin). The curve of tire A is very close to the one of the high performance bicycle tire.
The curves of normalized self aligning torque of the two tires are rather close and both show a tendency to saturation above 3°. The maximum values (in modulus) of self aligning torques of tire A and B are similar to the maximum value (in modulus) of the self aligning torque of the bicycle tire, but the bicycle tire shows a larger slope near the origin and reaches saturation for a lower value of side slip angle.
The curves of normalized camber force are regular and monotonic for both tires and both curves show smaller values than the ones of the high performance bicycle tire, but tire A exhibits larger values than tire B for camber angles greater than 6°.
Finally, the curves of twisting torque against camber angle are almost linear, in this case the three tires tend to mingle with each other.

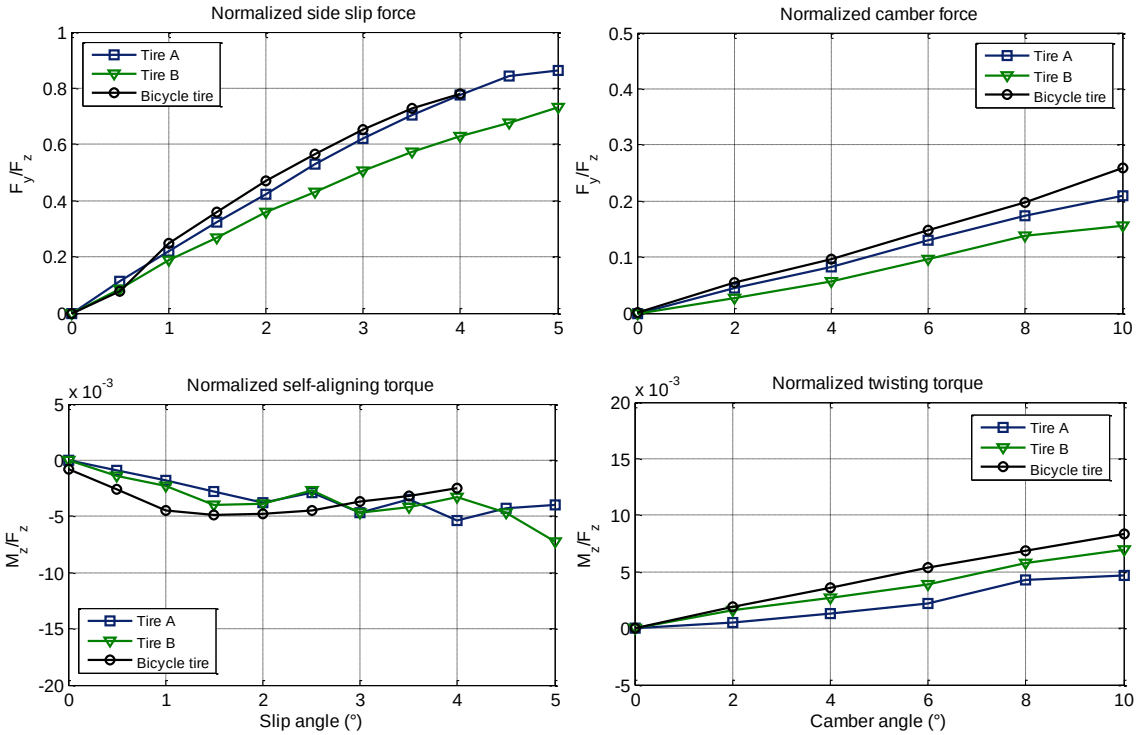

Figure 53 Forces and torques of wheelchair and bicycle tires in reference conditions
(vertical load 400 N, inflation pressure 4 bar and disc speed 4 km/h)

The effect of different conditions has been analyzed carrying out specific tests in which only one parameter was varied at a time. The disc speed, which corresponds to the wheelchair forward speed, has a negligible effect on the measured tire properties. To give an example, Figure 54 shows the effect of a decrease in speed on the side slip force generated by tire A, the difference between the two curves is negligible.
Figure 55 deals with the effect of inflation pressure on tire performance, a strong decrease in tire pressure (from 4 to 2 bar) is considered. Tire properties related to side slip angle are strongly affected by inflation pressure. In both tires a decrease in inflation pressure causes a large decrease in the side slip force generated at the same side slip angle. This trend agrees with the ones measured in bicycle tires [18] and the ones measured in motorcycle and scooter tires [29], which moreover sometimes show a saturation at high pressure. Self aligning torque increases (in modulus) when inflation pressure decreases, probably because the contact patch becomes larger. This result is in agreement with the measurements carried out on bicycle and motorcycle tires [18] [29]. Coming to camber force, Figure 55 shows that camber force

generated by tire A is not influenced by inflation pressure, like it happens in bicycle tires; whereas camber force generated by tire B tends to increase if inflation pressure decreases, like it happens in many motorcycle tires. Like in bicycle tires, inflation pressure has a negligible effect on twisting torque.

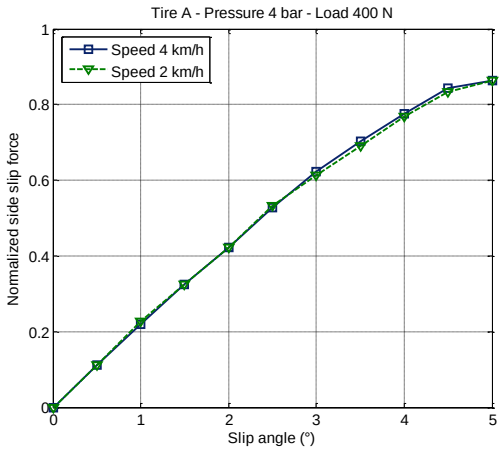

Figure 54 Effect of forward speed on side slip force

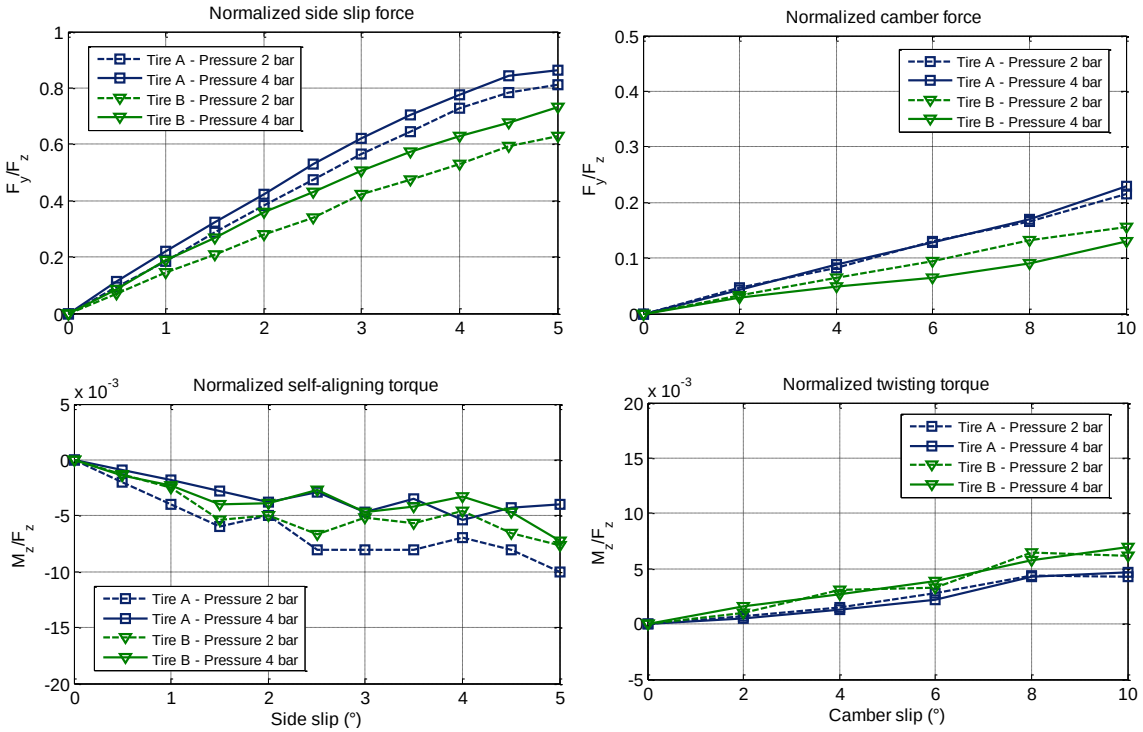

Figure 55 Effect of inflation pressure on tire forces and torques

The last parameter here considered is vertical load, its effect is shown in Figure 56. In wheelchair tires, like in bicycle and motorcycle tires, when vertical load increases lateral forces do not increase proportionally, because normalized lateral forces decrease when vertical load increases. This effect is particularly important for side slip force. The effect of vertical load in tire torques is less prominent: in tire A self aligning and twisting torques are almost unaffected by tire load, whereas in tire B both torque components decrease slightly (in modulus) when load increases.

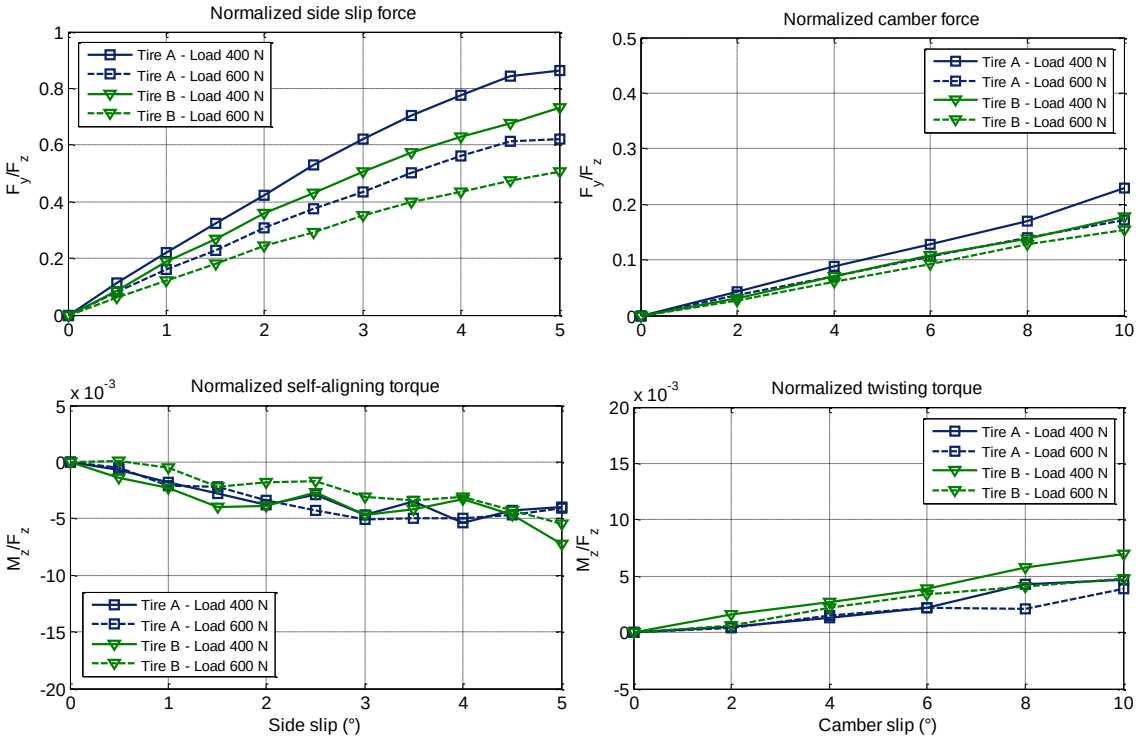

Figure 56 Effect of vertical load on tire forces and torques

7.2 Mathematical model

In the framework of this research, a specific mathematical model of a wheelchair moving on a horizontal road has been developed with the aim of studying the effect of the measured tire properties on typical maneuvers. The model includes five rigid bodies: the wheelchair with the user, the rear wheels and the front castering wheels.

The main assumptions that were made to develop the model are here summarized:

• The user is a rigid body firmly attached to the chair and exerts two propulsive torques on the rear wheels.

• The wheels roll without slipping in the longitudinal direction, which is the intersection between the wheel plane and the road plane.

• The wheels can slip in the lateral direction, which is the direction in the load plane perpendicular to the wheel plane.

• The side slip angles are small, therefore their trigonometric functions can be linearized, tire forces and torques can be approximated as linear functions of side slip angle. This assumption is currently made for studying standard maneuvers of cars.

• The load transfer between front and rear wheels is neglected, because neither sudden accelerations nor sudden deceleration are compatible with standard operations of wheelchairs.

• The lateral load transfer (between right and left wheels) is neglected, because large centrifugal forces are not compatible with standard operations of wheelchairs.

• The mass and moment of inertia of the small castering wheels is neglected.

• Transient tire properties (e.g. relaxations length) are negligible because they have a very small effect on cornering properties at low speed (typically they affect high speed stability of motorcycles).

The system has five degrees of freedom: longitudinal and lateral displacements of the center of mass of the chair-user, rotation ψ of the chair-user in the plane of motion, caster angles of front wheels (δ_{fr} and δ_{fl}).

Equations of motion are written in coordinate system x_m y_m, which moves with the vehicle. Absolute velocity of the center of mass (V) has components u and v along axes x_m y_m respectively.

7.3 Effect of cornering stiffness

The effect of cornering stiffness has been studied performing three numerical simulations on two typical wheelchair maneuvers: the steady-turning and the slalom. Each time, a different value has been assigned to the cornering stiffness: in one case the measured value, in another case the half of the measured value and in the last case the double of the measured value, so that a wide range of different possibilities has been analyzed.

Figure 57 shows the effect of cornering stiffness on trajectory and slip angles in the steady-turning maneuver. From a closer look of the first graph, it is worth noticing that the radius of the trajectory slightly decreases if the cornering stiffness increases. This result agrees with the effect of the cornering stiffness on the values of slip angle for the right (up) and left (down) rear wheels. If the stiffness increases, the slip angles reached at the steady-state decrease. Moreover, it is possible to notice that the slip angles exhibit an inversely proportional behavior with respect to the value of cornering stiffness: for example, for a value of cornering stiffness equal to the half of the measured value a double slip angle is obtained. The values of the slip angles are lesser than 1° in most cases, which confirms the correctness of the linearization of the trigonometric functions of the model with linear functions.

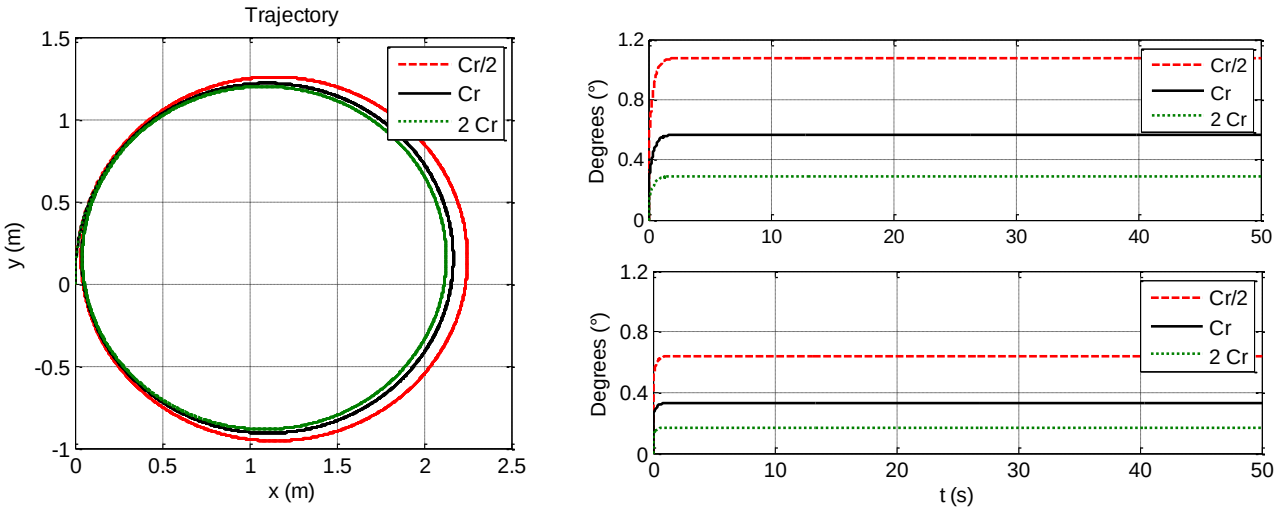

Figure 57 Effect of cornering stiffness on trajectory and slip angles in the steady-turning maneuver

Figure 58 shows the effect of cornering stiffness on trajectory and slip angles in the slalom maneuver. Also for this maneuver, the effect of the cornering stiffness on the trajectory is rather limited, an increase in the stiffness causes a small increase in the amplitude of the trajectory. The curves of the side slip angles of the right (up) and left (down) rear wheels show that if the self-aligning torque stiffness increases, the amplitudes decrease. The curves are also asymmetrical with respect to the y-axis: the right wheel shows a positive mean value, the left wheel shows a negative mean value. It is interesting to highlight the small phase shift that occurs between the curves of the slalom simulations. If, for example, the graph of the trajectory is taken into account, it is possible to notice that the trajectory with a larger amplitude shows a phase lag with respect to the trajectory with smaller amplitude. Form a physical point of view, since the forward speed of the vehicle u is constant, if the trajectory becomes larger more time is spent in order to carry out the lateral displacement and the vehicle moves less in the longitudinal direction.

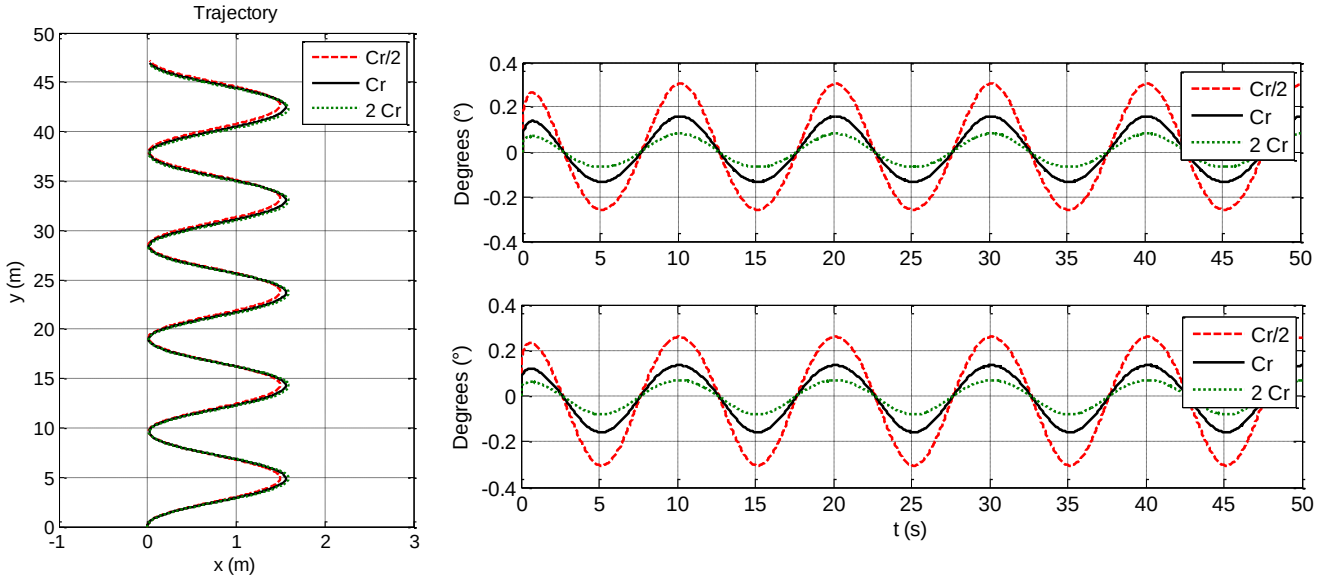

Figure 58 Effect of cornering stiffness on trajectory and slip angles in the slalom maneuver

7.4 Effect of self-aligning torque stiffness

Similarly to the case of the cornering stiffness, three simulations have been performed on the steady-turning and the slalom maneuvers, the self-aligning torque stiffness ranging from half to the double of the measured value. Figure 59 shows the effect of self-aligning torque stiffness on trajectory and slip angles in the steady-turning maneuver. It is possible to notice that the self-aligning torque stiffness has a weaker influence on the output parameters of the model. If the value of C_{mr} increases, the slip angles slightly decrease. On the contrary, if the self-aligning torque stiffness increases, also the radius of the trajectory increases. It is an expected result, because with smaller slip angles the wheelchair can balance a smaller centrifugal force (the forward speed u is constant, and the radius increases).

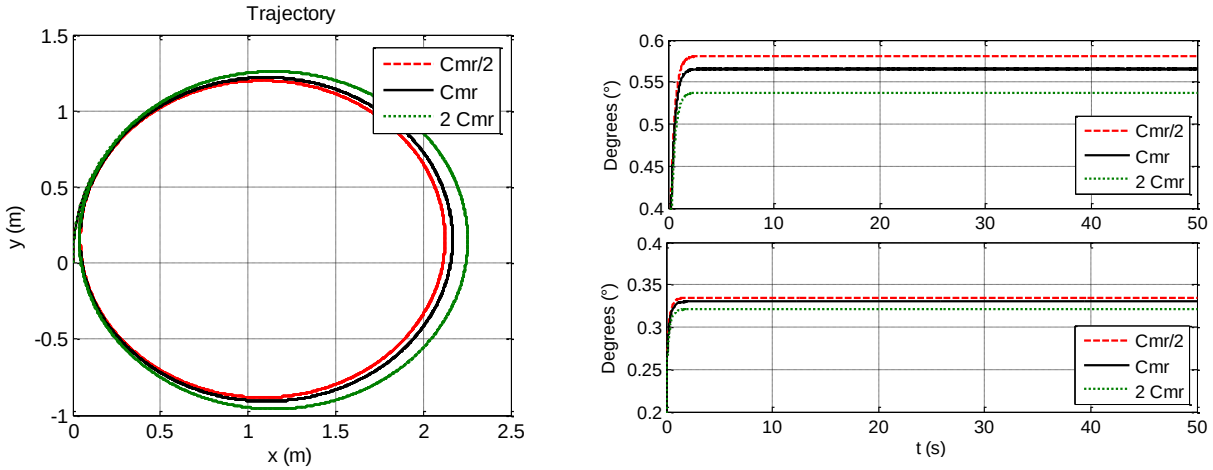

Figure 59 Effect of self-aligning torque stiffness on trajectory and slip angles in the steady-turning maneuver

The outputs of the three simulations of the slalom maneuver are shown in Figure 60. If self-aligning torque stiffness increases, the trajectory tends to become slightly tighter, also in this case it is possible to observe a small phase lag between the three trajectories. No significant effect is observed on the slip angles of the right (up) and left (down) rear wheels.

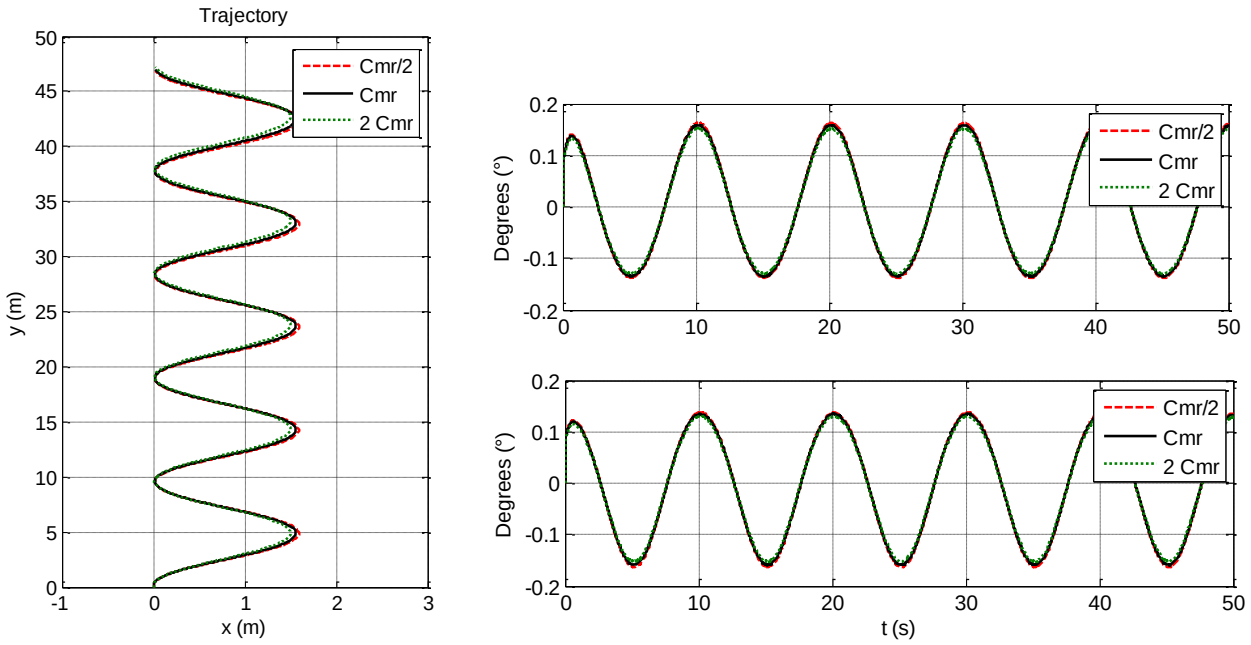

Figure 60 Effect of self-aligning torque stiffness on trajectory and slip angles in the slalom maneuver

Conclusions

The aim of the present research was focused on the identification and the improvement of the dynamic properties of the components of two-wheeled vehicles: fork, chassis, swingarm and tires. Even if these components are different and show specific properties an unified approach has been adopted, which has its theoretical basis in modal analysis.

Significant attention has been paid to the identification of static and dynamic properties of two-wheeled vehicle components, specifically motorcycles and bicycles components. One of the most important targets of this work was the development of a characterization technique that allowed not only the identification of the stiffness properties of the tested components, but made it possible also to introduce the identified stiffness properties with a lumped element approach in mathematical models and multi-body codes. The twist axis (or Mozzi axis) approach has proven to give encouraging results in terms of stiffness properties identification, both in static and dynamic conditions. In most cases the twist axis approach makes it possible both the identification of the critical stiffness property and the location of the lumped element.

The focus of research was on the dynamic properties of motorcycle components that influence the vehicle stability (weave and wobble modes) and performance. Further studies are needed to optimize other properties that affect load capability, reliability and comfort.

It is accepted that one of the best methods for carrying out this analysis is making use of numerical simulations. In the framework of this research, numerical simulations have been carried out on a motorcycle model which employed the identified stiffness properties of the enduro front fork, and on an improved bicycle model which employed the identified stiffness properties of the steel fork. A potential, future development of this work could consist in a deeper analysis of how the stiffness properties of two-

wheeled vehicle components affect the vehicle stability. This analysis could be performed on a multi-body code (there are already a lot of them, one in our research group as well), introducing in the model the structural properties identified with the experimental approach described in this thesis.

Appendix 1 – Tires rigid ring model of a tire

The following equations are used for describing the ring model discussed in the fourth section of this paper and shown in the block diagram of Figure 41. The first equation relates the side-slip angle and the side-slip rate of the contact patch ($\alpha_1, \dot{\alpha}_1$) with the input yaw angle and yaw rate ($\psi_b, \dot{\psi}_b$) and the lateral velocity of the belt ($\dot{y}_b$).

$$\sigma_c \dot{\alpha} + V\alpha = -a\dot{\psi}_b + V\psi_b - \dot{y}_b$$

The side-slip angle is associated to the side-slip force (F_y) by means of the cornering stiffness ($C_{bF\alpha}$):

$$F_y = C_{bF\alpha}\alpha$$

The third equation is associated with the lateral equilibrium of the rigid belt: the side-slip force is balanced by the stiffness $C_{yg}y_b$ and damping $K_{yg}\dot{y}_b$ forces of the carcass:

$$F_y = C_{yg}y_b + K_{yg}\dot{y}_b$$

The effects of the self-aligning torque and the diametrical mode of the tire about vertical axis are related by means of the following equation for the yaw equilibrium:

$$-C_{zz}\left(\psi_b - \psi_a\right) - K_{zz}\left(\dot{\psi}_b - \dot{\psi}_a\right) + M_z = 0$$

The last equation relates the self-aligning torque with the lateral force by means of the trail (t_0):

$$M_z = -t_0 F_y$$

The Frequency Response Function of the model is shown in the following equation:

$$FRF = \frac{(V - \omega a i)\cdot C_{bF\alpha}}{\dfrac{\omega i C_{bF\alpha}}{C_{yg} + \omega K_{yg} i} + \dfrac{\left(V - \omega a i\right)\cdot C_{bF\alpha} t_0}{C_{zz} + \omega K_{zz} i} + V + \sigma_c \omega i}$$

If the term due to the tire trail is neglected, a very small error is introduced and the FRF equation becomes:

$$FRF = \frac{(V - \omega a i)\cdot C_{bF\alpha}}{\dfrac{\omega i C_{bF\alpha}}{C_{yg} + \omega K_{yg} i} + V + \sigma_c \omega i}$$

If also the effect of tire dampings is not considered, the simplified model becomes a first order model and the FRF equation becomes:

$$FRF = \frac{(V - \omega a i)\cdot C_{bF\alpha}}{\dfrac{\omega i C_{bF\alpha}}{C_{yg}} + V + \sigma_c \omega i} a$$

Appendix 2 – Steady-state tests of motorcycle tires

The steady-state properties considered in the framework of this research are defined as lateral forces (side-slip and camber forces) and yaw torques (self-aligning and twisting torque).

In order to perform steady-state tests, the spinning of the rotating disk of the machine is controlled at an assigned speed, then either the roll motor or the side-slip motor are actuated to set the camber or side-slip angle to the assigned value. The arm configuration is held constant for about 10 s and, when the steady-state condition is reached, lateral force and torques are measured. In order to speed up the testing procedure the machine is programmed to perform the above-mentioned steps for increasing values of camber or side-slip angle from zero to the maximum values admitted by the machine (camber angle ± 55°, side-slip angle ± 10°). If camber angle is set at zero and side-slip angle is varied the curves of side-slip force and self-aligning torque are measured. The self-aligning torque is caused by the non-symmetric distribution of stresses along the contact patch and it tends to align the wheel to the direction of speed, if a perturbation takes place [1]. When the side-slip is set at zero and camber is varied the curves of camber force and twisting torque are measured. The twisting torque represents the tendency of the cambered wheel to move along a trajectory with a curvature radius smaller than the one demanded by the steady turning maneuver, it does not tend to align the wheel [1].

Figures 57-60 refer to the results of the tests carried out on the six tires. All the tires have been tested in steady state conditions with a vertical load of 1500 N. The inflation pressure of the tires ranges from 0.5 to 4 bar, the wide variations are extremely interesting because the research on the mechanics of the tires for single-track vehicles up to now has scarcely addressed the problem of the tire's behavior in the presence of large variations in inflation pressure. In every graph each force or torque component is plotted against the corresponding tire angle (side-slip or camber angle) for increasing values of inflation pressure. In order to give a quick idea of the effect of pressure, typical values of side-slip and camber angles are chosen (4° and 24° respectively), and the plots of tire forces and torques against pressure at assigned angles are represented as well.

In the front tires side-slip force increases when pressure increases and sometimes shows a flat top at pressure larger than the nominal one (e.g. in the motorcycle front tire). In rear tires, whose cross sections have larger radius of curvature, side-slip force shows a maximum at the nominal inflation pressure or just above this value.

In all the tested tires camber force reaches the maximum value when the tire is almost deflated. In this condition the deformation of the tire's carcass is large and the contact patch is wide. Hence, in the cambered wheel a large part of the tire's tread has to go away from the theoretical elliptical path when entering the contact patch, generating a very large camber force, a detailed description of camber force generation is included in [1]. If inflation pressure slightly increases, camber force maintains very large values. Only above 1-1.5 bar (depending on the tire) camber force starts decreasing monotonically, if pressure increases.

The curves of self-aligning torque against side-slip angle show again that the maximum values (in modulus) is measured when the tire is almost deflated. This result agrees with physical intuition, because, when inflation pressure is very low, contact patch is very large and stresses are able to generate very large moments. In the tires with large radius of curvature of the cross sections (e.g. 180-55-R17) small increments in inflation pressure from the minimum value do not change very much the deformation of the

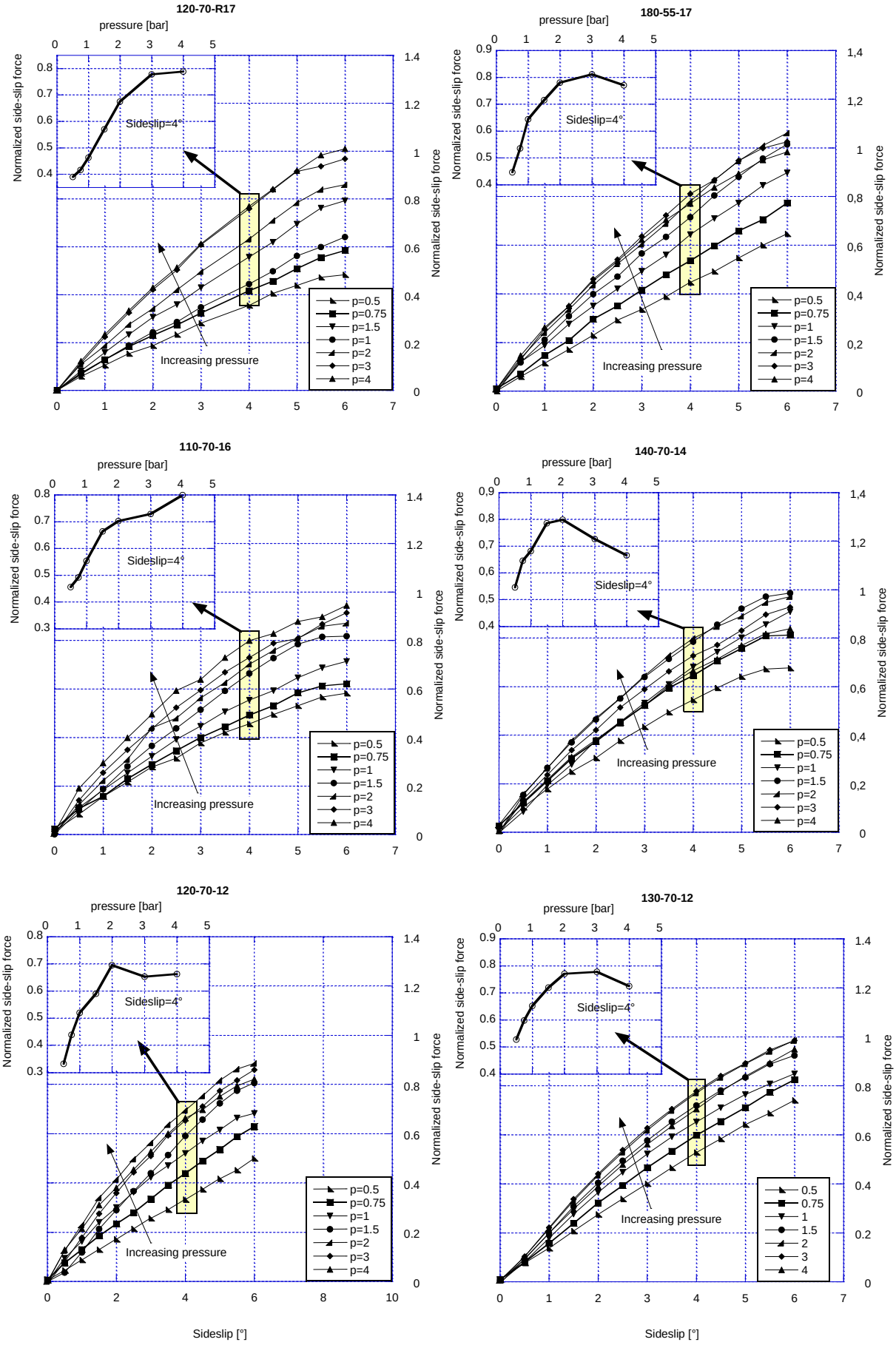

Figure 61 Normalized side-slip forces measured on the three tires sets.

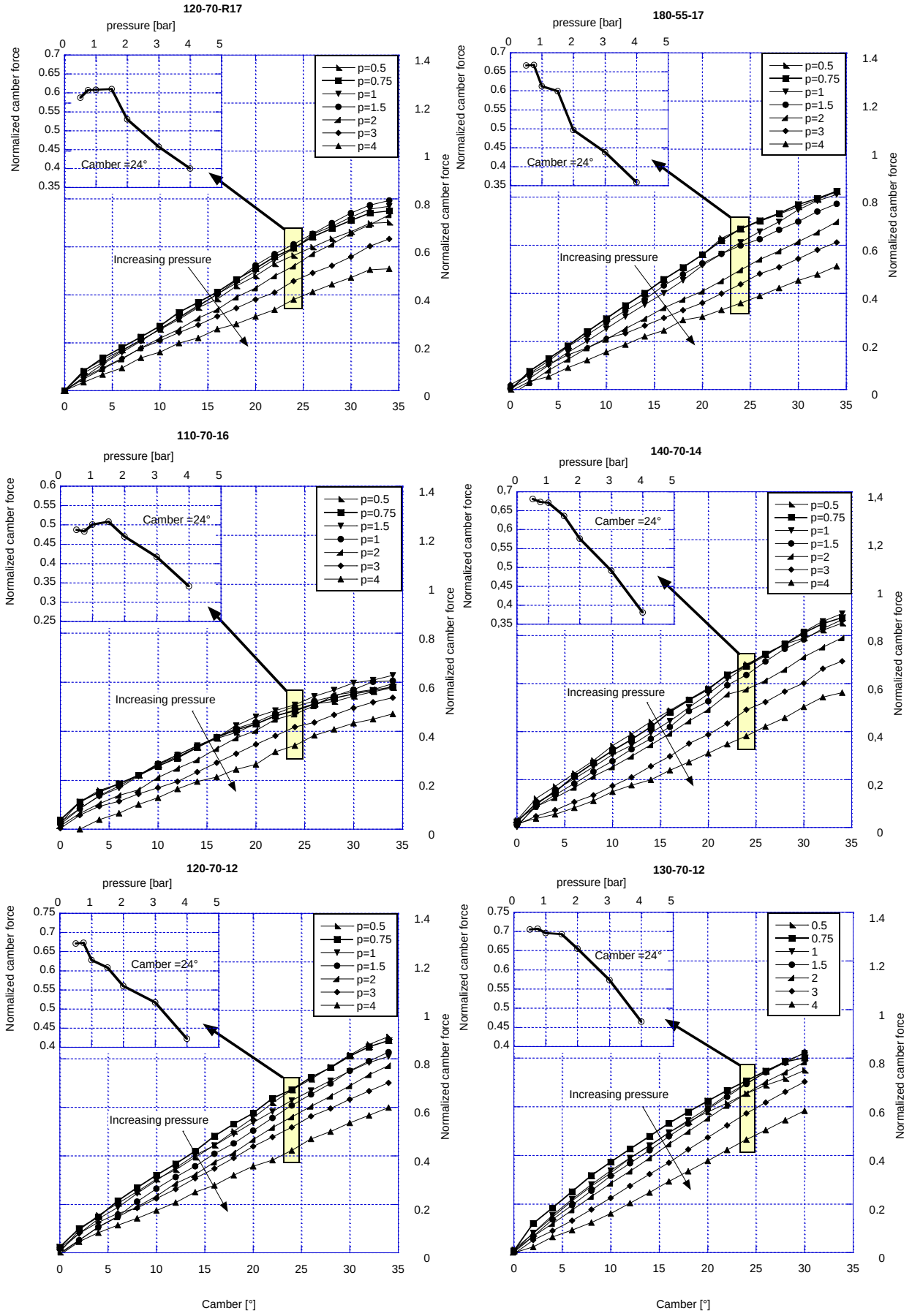

Figure 62 Normalized camber forces measured on the three tires sets.

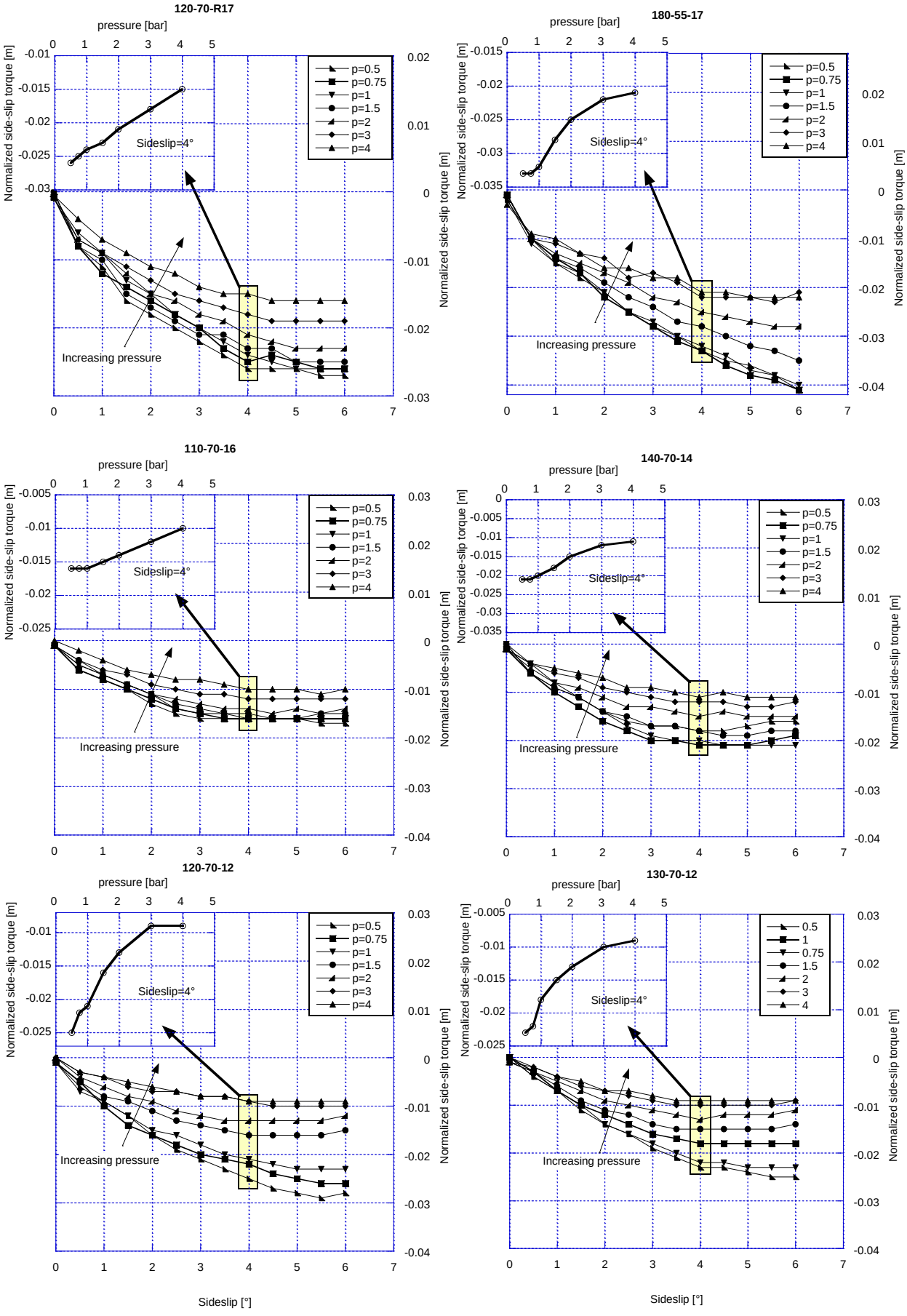

Figure 63 Normalized self-aligning torques measured on the three tires sets.

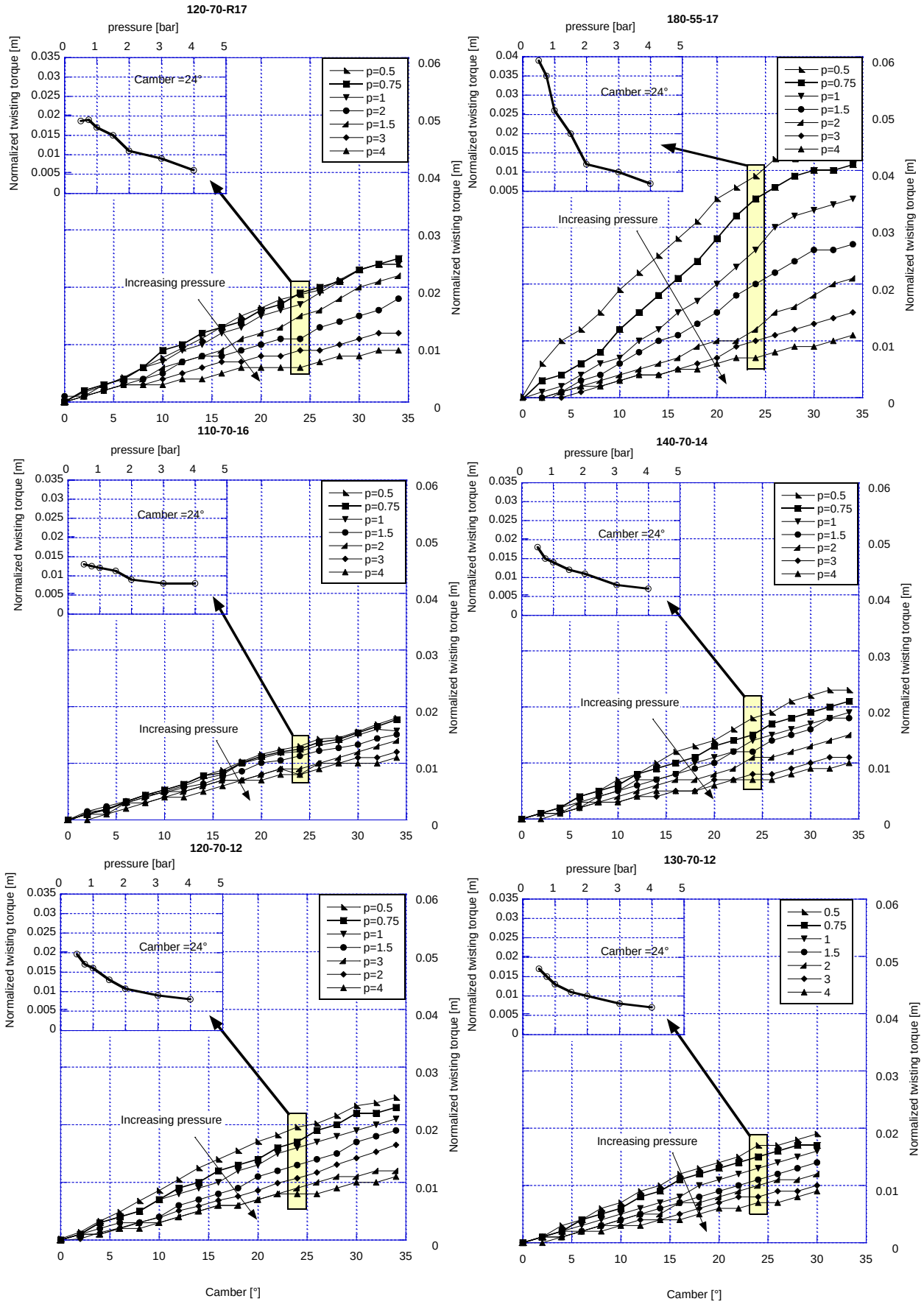

Figure 64 Normalized twisting torques measured on the three tires sets.

tire and self-aligning torque maintains large values. In all the measured tires, if inflation pressure raises above 1 bar, self-aligning torque decreases monotonically when pressure further increases. In the small scooter tires (120-70-12) variations in inflation pressure above 3 bar do not modify the self-aligning torque.

The plots of twisting torque against camber angle show that this component of the yaw torque decreases when inflation pressure increases. The phenomenon is very evident in the motorcycle rear tire. In the cambered wheel different longitudinal slips are present in the inner side (towards the centre of curvature) and in the outer side of the contact patch, these slips generate longitudinal stresses that in turn generate the twisting torque [1]. Since the contact patch becomes larger when inflation pressure lowers the moments of the longitudinal stresses with respect to the centre of the contact patch increase, generating the measured increment in the twisting torque.

Note that all tire data are reported at a normal load of 1500 N in order to have a proper comparison. However, tires have been tested also for a higher (2000 N) and a lower (1000 N) load, measuring similar trends for camber force, self-aligning torque and twisting torque. The normalized side-slip force shows a more complex behavior and in some tests at 1000 N it decreases as inflation pressure increases. This increasing/decreasing load dependent behavior was observed also for car tires in [35] and for different motorcycle tires [36].

Summarizing, when the tire is deflating the normalized side-slip force either decreases or increases depending on the specific tire and nominal load, whereas normalized camber force increases and both the normalized components of yaw torque increase in modulus. Large effect on stability and handling may result as a result of such variations.

Appendix 3 – Improved bicycle model

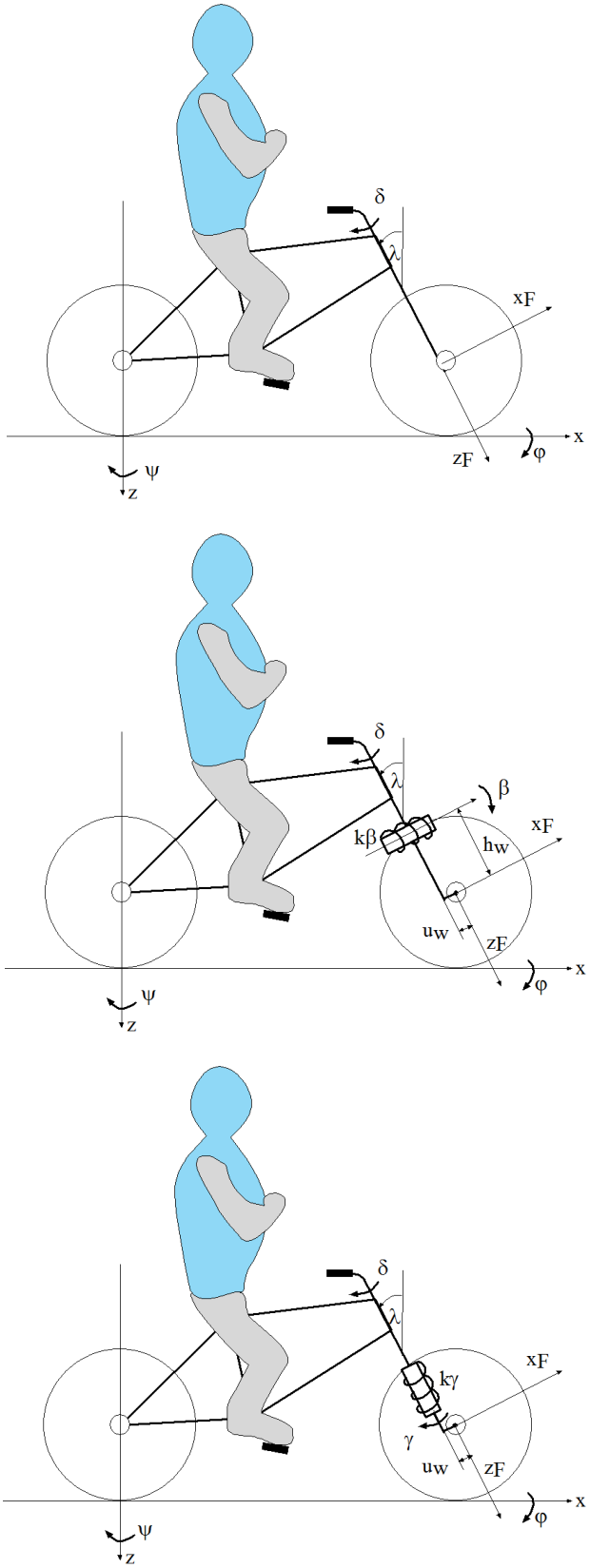

Figure 65 a) Carvallo and Whipple bicycle model; b) bicycle model with bending compliance; c) bicycle model with torsion compliance.

Figure 65 a) shows the benchmark bicycle model developed by Whipple and Carvallo at the end of the XIX century. Figure 65 b) and c) shows the bicycle models that take into account either bending or torsion compliance of the front fork. The model with bending compliance includes a revolute joint perpendicular to the steer axis that defines the bending axis and divides into two parts the front fork. A rotational spring with stiffness k_β and a rotational damper with constant c_β (not shown in Figure 65) oppose to rotation β and angular velocity $\dot{\beta}$ respectively. Constants k_β, c_β and the position of the bending axis (h_W) have been found from experimental tests. The model with torsion compliance includes a revolute joint (rotation γ) parallel to the steer axis. A rotational spring with stiffness k_γ and a rotational damper with constant c_γ (not shown) oppose to torsion rotation γ and angular velocity $\dot{\gamma}$ respectively. Forward speed v is assumed constant.

The linearized equations of the Carvallo and Whipple bicycle model derive from angular momentum balances. The first equation (roll equation) derives from the roll angular momentum balance for the whole bicycle (including the rider) about a fixed axis in the road plane that is instantaneously aligned with the line where the rear frame of the bicycle intersects the road plane (axis φ). The second equation (yaw equation) derives from the yaw angular momentum balance for the whole bicycle about a fixed vertical axis that instantaneously passes through the contact point of the rear wheel (axis ψ). The third equation (steer equation) derives from steer angular momentum balance of the front frame about the steer axis (axis δ).

The rotation of the front wheel about the bending (or torsion) axis due to the bending (or torsion) compliance generates new angular momentum components that have to be taken into account. In the following of this section the procedure for developing the bicycle model with bending compliance will be presented, similar calculations are carried out for developing the model with torsion compliance.

First the Euler's equation of the front wheel in the front wheel frame of reference (x_F, y_F, z_F) is developed:

$$ {}^{F}\begin{bmatrix} I_{Fxx} & 0 & 0 \\ 0 & I_{Fyy} & 0 \\ 0 & 0 & I_{Fzz} \end{bmatrix} {}^{F}\begin{Bmatrix} \alpha_x \\ \alpha_y \\ \alpha_z \end{Bmatrix} + {}^{F}\begin{bmatrix} 0 & -\omega_z & \omega_y \\ \omega_z & 0 & -\omega_x \\ -\omega_y & \omega_x & 0 \end{bmatrix} {}^{F}\begin{bmatrix} I_{Fxx} & 0 & 0 \\ 0 & I_{Fyy} & 0 \\ 0 & 0 & I_{Fzz} \end{bmatrix} {}^{F}\begin{Bmatrix} \omega_x \\ \omega_y - v/r_F \\ \omega_z \end{Bmatrix} = {}^{F}\begin{Bmatrix} M_x \\ M_y \\ M_z \end{Bmatrix} \quad (61) $$

The first term is due to the variation of the angular moment, the second term is the vector product between the velocity of the center mass of the wheel and the momentum of the wheel; and the third term (second member) represents the components of the moments of the external forces about the center mass of the front wheel. $I_{Fxx}=I_{Fzz}$ is the moment of inertia of front wheel about the diametrical axis, I_{Fyy} the polar moment of inertia, $-v/r_F$ is the spin velocity of front wheel, r_F the front wheel radius. $\omega_x, \omega_y, \omega_z$ are the components of angular velocity of the front wheel due to roll ($\dot{\varphi}$), yaw ($\dot{\psi}$), steer ($\dot{\delta}$) and bending velocity ($\dot{\beta}$), if second order terms are neglected, they are:

$$ \begin{Bmatrix} \omega_x \\ \omega_y \\ \omega_z \end{Bmatrix} = \begin{Bmatrix} \dot{\varphi}\cos(\lambda) - \dot{\psi}\sin(\lambda) + \dot{\beta} \\ 0 \\ \dot{\varphi}\sin(\lambda) + \dot{\psi}\cos(\lambda) + \dot{\delta} \end{Bmatrix} \quad (62) $$

$\alpha_x, \alpha_y, \alpha_z$ are the components of angular acceleration of front wheel:

$$\begin{Bmatrix}\alpha_x\\ \alpha_y\\ \alpha_z\end{Bmatrix}=\begin{Bmatrix}\ddot{\varphi}\cos(\lambda)-\ddot{\psi}\sin(\lambda)+\ddot{\beta}\\ 0\\ \ddot{\varphi}\sin(\lambda)+\ddot{\psi}\cos(\lambda)+\ddot{\delta}\end{Bmatrix} \quad (63)$$

The first of the Euler's equation (about x_F axis parallel to the bending axis) is added to the other angular momentum equations of the benchmark Carvallo and Whipple model and it is the fourth equation of the model.

However, in the roll, steer and yaw equations new terms that derive from the bending motion of the front wheel have to be added. The new terms are given by the projection of the left hand side of Euler's equations on the roll, steer and yaw axes. Bending rotation modifies the position of the centre of mass of front wheel, the new linear momentum term is:

$$P_W = -m_F h_W \dot{\beta}\hat{j} \quad (64)$$

In which m_F is the front wheel mass, h_W the distance between the bending axis and the center of mass of the wheel and $\hat{j}$ the unit vector perpendicular to the bicycle plane. The corresponding angular momentum components about roll, steer and yaw axes have been calculated. Bending rotation affects also the moments caused by gravity force of the front wheel and by the front vertical ground reaction, also these effects have been taken into account in the model.

The four equations of the model contain five unknowns. They are $\varphi,\delta,\psi,\beta$ and lateral ground force at front contact (F_{Fy}). F_{Fy} appears in the yaw, steer and front wheel equation, and this unknown is eliminated by means of the yaw equation. Finally, yaw velocity and acceleration are eliminated by means of the rolling contact lateral constraint.

The final set of equations includes three linear second order coupled equations in the variables φ,δ,β. They represent free oscillations of the system and are useful for studying uncontrolled stability (hands off the handlebar). The set of these equations is similar to the one of the Carvallo and Whipple bicycle model:

$$\left[M^B\right]\begin{Bmatrix}\ddot{\varphi}\\ \ddot{\delta}\\ \ddot{\beta}\end{Bmatrix}+v\left[C_1^B\right]\begin{Bmatrix}\dot{\varphi}\\ \dot{\delta}\\ \dot{\beta}\end{Bmatrix}+\left[C^B\right]\begin{Bmatrix}\dot{\varphi}\\ \dot{\delta}\\ \dot{\beta}\end{Bmatrix}+\left[g\left[K_0^B\right]+v^2\left[K_2^B\right]\right]\begin{Bmatrix}\varphi\\ \delta\\ \beta\end{Bmatrix}+\left[K^B\right]\begin{Bmatrix}\varphi\\ \delta\\ \beta\end{Bmatrix}=\begin{Bmatrix}0\\ 0\\ 0\end{Bmatrix} \quad (65)$$

In which $\left[M^B\right]$ is a symmetric mass matrix, $\left[C_1^B\right]$ a damping matrix that accounts for gyroscopic effects and the fourth matrix is a stiffness matrix that is the sum of two terms. Term $g\left[K_0^B\right]$ is proportional to gravity acceleration (g) and takes into account gravity terms, whereas term $v^2\left[K_2^B\right]$ is proportional to forward speed squared (v^2) and takes into account centrifugal and gyroscopic effects. These matrices have the same meaning of the corresponding matrices of the CWBM, but they have dimension 3x3 and account for the additional terms due fork bending , when they are present.

Matrices $\left[C^B\right],\left[K^B\right]$ are "true" damping and stiffness matrices and account for the stiffness and damping properties of the fork.

References

1. Cossalter, V., Motorcycle Dynamics, 2nd ed., 2007, Lulu.com.
2. Raines, M., Thorpe, T. E., 1987, An energy method for the identification of mechanisms of castor instability with particular application to motorcycles. Proceedings of Institute of Mechanical Engineers Vol 201, No D3.
3. Sharp R.S. and Alstead C.J., 1980, The influence of structural flexibilities on the straight-running stability of motorcycles, Vehicle System Dynamics 9, 327–357.
4. Cossalter, V., Lot, R., Massaro, M., 2007, The Influence of Frame Compliance and Rider Mobility on the Scooter Stability, Vehicle System Dynamics, 45(4), pp. 313–326.
5. Giles, C.G., Sharp, R.S., 1983, Static and dynamic stiffness and deflection mode measurements on a motorcycle, with particular reference to steering behaviour., proc. of IMechE Conference on Road Vehicle Handling, pp 185-192.
6. Raines, M., Thorpe, T. E., 1986, The relationship between twist axis and effective torsional stiffness of a motorcycle frame. Proceedings of Institute of Mechanical Engineers Vol 200, No D1.
7. M. Bocciolone, F. Cheli, M. Pezzola, and R. Viganò, 2005, Static and dynamic properties of a motorcycle frame: experimental and numerical approach, WIT Transactions on Modelling and Simulation, vol. 41, pp. 517-526.
8. V. Cossalter, A. Doria, R. Basso, D. Fabris, 2004, Experimental analysis of out-of plane structural vibrations of two wheeled vehicles, Shock and Vibration, 11, n. 3,4 pp. 433- 443.
9. N. M. M. Maia, J. M. Montalvao e Silva, 1997, Theoretical and Experimental Modal Analysis, John Wiley & Sons Inc, New York.
10. D. J. Ewins, 2000, Modal Testing, 2nd ed, Research Studies Press, Baldock, UK.
11. Whipple FJW. The stability of the motion of a bicycle, *Quart. Journal of Pure and Applied Mathematics* 30, 312-348, 1899.
12. Sharp RS. The stability and control of motorcycles. Journal of Mechanical Engineering Science, Vol. 13, 5, pp 316-329, 1971.
13. De Vries EJH and Pacejka HB. Motorcycle tyre measurements and models, Vehicle System Dynamics, Vol. 28 Supplement, pp 280-298, 1998.
14. Pacejka HB. Tire and Vehicle Dynamics, Butterworth and Heinemann, Oxford, 2002.
15. Besselink IJM, Schmeitz AJC and Pacejka HB. An improved Magic Formula/Swift tyre model that can handle inflation pressure changes, Vehicle System Dynamics, Vol. 48 Supplement, pp 337-352, 2010.
16. Schwab, A., L., Meijaard, J., P., Kooijman, J., D., G., Lateral dynamics of a bicycle with a passive rider model: stability and controllability, Vehicle System Dynamics, vol. 50 (8) (2012), pp. 1209-1224.
17. Sharp, R., S. On the stability and control of the bicycle, Applied Mechanics Reviews, Transactions of the ASME, vol. 61(2008), pp. 060803-1 060803-24.
18. Doria A., Tognazzo M., Cusimano G., Bulsink V., Cooke A., and Koopman B., Identification of the mechanical properties of bicycle tyres for modelling of bicycle dynamics, Vehicle System Dynamics, vol. 51(3) 2013, pp. 405–420.
19. Plöchl, M., Edelmann, J., Angrosch, B., Ott, C., On the wobble mode of a bicycle, Vehicle System Dynamics, vol.50(3) 2012, pp. 415-429.
20. Wojtowicki, J.-L., Champoux, Y., Thibault, J., Modal properties of road bikes vs ride comfort, Proceedings of IMAC-XIX: A Conference on Structural Dynamics; Kissimmee, FL; United States; 2001, Volume 1, Pages 648-652

21. Petrone N, Giubilato F., Methods for evaluating the radial structural behaviour of racing bicycle wheels, Procedia Engineering Volume 13, 2011, Pages 88-93.
22. Doria A., Formentini M., Identification of the structural modes of high performance bicycles in the perspective of wobble control, ASME Conference Proceedings, Year 2011, Volume 4: 8th International Conference on Multibody Systems,Nonlinear Dynamics, and Control, Parts A and B August 2011, Washington.
23. Tognazzo M., Modelli per la simulazione del sistema motociclo-uomo e identificazione delle proprietà biomeccaniche del pilota.
24. Marcolongo, R., 1905, Notizie Sul Discorso Matematico e Sulla vita di Giulio Mozzi, Bollettino di Bibliografia e Storia delle Scienze Matematiche 8 (1905), pp. 1–8.
25. Shabana, A., Dynamics of Multibody Systems – second edition. Cambridge University Press, Cambridge, 1997.
26. Ball, Sir, R. S., A treatise om the theory of screws, 1900, Cambridge University Press (reprinted 1999).
27. Lipkin, H., Duffy, J., 2002, Sir Robert Stawell Ball and methodologies of modern screw theory, Proceedings of Institute of Mechanical Engineers, Vol 216 Part C: Journal of Mechanical Engineering Science.
28. V.Cossalter, A. Doria, M. Massaro, L. Taraborrelli, Experimental and numerical investigation on the motorcycle front frame flexibility and its effect on stability, Mechanical System and Signal Processing (2015), http://dx.doi.org/10.1016/j.ymssp.2015.02.011
29. Cossalter, V., Doria, A., Lot, R., Ruffo, N., and Salvador, M., Dynamic properties of motorcycle and scooter tires: measurement and comparison, Vehicle System Dynamics, Vol. 39(5) (2003), pp. 329–352.
30. Meijaard, J., P., Papadopoulos, J., M., Ruina, A., Schwab, A., L., 2007, Linearized dynamics equations for the balance and steer of a bicycle : benchmark and review", Proc. R. Soc. A, vol. 463 (2007), pp. 1955-1982.
31. Klinger, F., Nusime, J., Edelmann, J., Plöchl, M., Wobble of a racing bicycle with a rider hands on and hands off the handlebar, Vehicle System Dynamics, Volume 52, Supplement 1, 2014, pp 51-68.
32. Soedel W. Vibrations of shells and plates – second edition, Marcel Dekker inc, New York, 1993.
33. Beards, C., Engineering Vibration Analysis with Application to Control Systems, Butterworth Heinemann, Oxford, UK, 1995.
34. A. Doria, L.Taraborrelli, *Out-of-plane vibrations and relaxation length of the tires for single-track vehicles*, Proceedings of the Institution of Mechanical Engineers, Part D: Journal of Automobile Engineering, DOI: 10.1177/0954407015590703
35. Higuchi, A., Pacejka, H., B., The relaxation length concept at large wheel slip and camber, Vehicle System Dynamics, Vol. 27 Supplement (1997), pp. 329–352.
36. Pacejka, H., B., Bakker, E. The Magic Formula Tire Model, Vehicle System Dynamics, v 21, n SUPPL, p 1-18, 1993.

List of captions

Figure 1 Dynamic models interrelation (case with no damping) 11
Figure 2 The *Motostiffmeter* 12
Figure 3 The arrangement of the laser sensors on the reference plate..... 13
Figure 4 Laser outputs measured during a dynamic test carried out at 5 Hz 15
Figure 5 The arrangement of the mono-axial accelerometers on the reference plate 16
Figure 6 Phase shift occurring at 67 Hz in a measurement on front fork A 17
Figure 7 Loaded end of a 2D structure with the reference plate. 18
Figure 8 Definition of Mozzi (or instantaneous screw) axis. 19
Figure 9 Impulse and frequency response of a system in time and frequency domains. 20
Figure 10 Acquisition of the FRFs matrix 22
Figure 11 The *Mototiremeter* 24
Figure 12 Frame A and Frame B 27
Figure 13 Displacements of nodes in the lateral and the torsional 28
Figure 14 Displacements of nodes in the lateral and the torsional 28
Figure 15 Frame A, front-constrained, static and dynamic twist axes 29
Figure 16 Frame B, front-constrained, static and dynamic twist axes. 30
Figure 17 Frame A, rear-constrained, static and dynamic twist axes. 31
Figure 18 Frame B, rear-constrained, static and dynamic twist axes..... 31
Figure 19 Displacements of nodes in the lateral and the torsional modes of frame , without and with the engine. 33
Figure 20 Frame C without the engine, static and modal Mozzi axes..... 33
Figure 21 Frame C with the engine, static and modal Mozzi axes. 34
Figure 22 Swing arm A and swing arm B during tests on the *Mototiremeter* 35
Figure 23 Displacements of nodes in the lateral and the torsional modes of swing-arm A. 36
Figure 24 Swing-arm A static and dynamic twist axes. 37
Figure 25 Displacements of nodes in the lateral and the torsional modes of swing-arm B. 38
Figure 26 Swing-arm B static and dynamic twist axes..... 38
Figure 27 Front fork A on the *Mototiremeter* 41
Figure 28 Twist axis for static test for the enduro fork 42
Figure 29 Evolution of twist axis position from 1 Hz (quasi-static condition) to 15 Hz, enduro fork..... 42
Figure 30 Bending and torsion axes identified on fork A with the three-accelerometers technique..... 43
Figure 31 Measured FRFs of the enduro fork without wheel in the x, y and z directions. 44
Figure 32 First modes of vibration of the enduro motorcycle's fork without (left) and with (right) the wheel. 45
Figure 33 Free vibration modes of the enduro bike, for speed from 5 to 40m/s 48
Figure 34 Twist axis for static test for the super-sport fork. 48
Figure 35 The cross sections of the six tested tires: experimental data and fitted profiles. 51
Figure 36 Experimental relaxation lengths of a motorcycle set and a scooter set of tires 52
Figure 37 Measurement points for modal analysis. 53
Figure 38 The identified modal shapes 53
Figure 39 Measured FRFs for several values of inflation pressure, 110-70-16 tire..... 54
Figure 40 Modal mass and stiffness 55

Figure 41 Block diagram of the mathematical model 57
Figure 42 Variation in contact patch sizes with pressure, tire 120-70-12 58
Figure 43 Predicted and measured relaxation lengths. 59
Figure 44 The measurement points for modal analysis 62
Figure 45 Overlays of FRFs measured on the steel bicycle: all points (left) and only fork ones (right.) 63
Figure 46 The seven common modes of the tested bicycles in the range 0-75 Hz 64
Figure 47 The mode at about 61 Hz on the steel bicycle. 65
Figure 48 The tested front forks: carbon fork with the wheel (right) and steel fork (left). 66
Figure 49 The modal shapes of the carbon fork without the wheel. 66
Figure 50 The modal shapes of the carbon fork with the wheel. 67
Figure 51 Eigenvalues of the model with bending stiffness and damping (left, h_w=0.21), and eigenvalues of CWBM (right) blue dots real parts, purple crosses imaginary parts 71
Figure 52 Eigenvalues of the model with torsion stiffness and damping, blue dots real parts, purple crosses imaginary parts. 72
Figure 53 Forces and torques of wheelchair and bicycle tires in reference conditions 74
Figure 54 Effect of forward speed on side slip force 75
Figure 55 Effect of inflation pressure on tire forces and torques 75
Figure 56 Effect of vertical load on tire forces and torques 76
Figure 57 Effect of cornering stiffness on trajectory and slip angles in the steady-turning maneuver 77
Figure 58 Effect of cornering stiffness on trajectory and slip angles in the slalom maneuver 78
Figure 59 Effect of self-aligning torque stiffness on trajectory and slip angles in the steady-turning maneuver 78
Figure 60 Effect of self-aligning torque stiffness on trajectory and slip angles in the slalom maneuver 79
Figure 61 Normalized side-slip forces measured on the three tires sets. 84
Figure 62 Normalized camber forces measured on the three tires sets. 85
Figure 63 Normalized self-aligning torques measured on the three tires sets. 86
Figure 64 Normalized twisting torques measured on the three tires sets. 87
Figure 65 a) Carvallo and Whipple bicycle model; b) bicycle model with bending compliance; c) bicycle model with torsion compliance. 89

Table 1 Advantages and disadvantages of different excitation techniques 22
Table 2 Advantages and disadvantages of different constrain methods 22
Table 3 Linear stiffness and rotational stiffness about the static twist axis 29
Table 4 Calculated values of bending and torsion stiffness. 32
Table 5 Stiffness parameters identified for frame C 34
Table 6 Modal parameters of swing-arm A. 36
Table 7 Stiffness parameters identified for swing-arm A 37
Table 8 Modal parameters of swing-arm B. 38
Table 9 Stiffness parameters identified for swing-arm B. 39
Table 10 Stiffness parameters identified of the enduro fork: the simple method employs the bending and torsion axes assumed *a priori* (Figure 28); the modal method employs the bending and torsion axes identified with dynamic tests. 42
Table 11 Modal parameters of the enduro fork without (left) and with (right) the wheel. 44

Table 12 Parameters for the lumped models of the enduro fork. 47
Table 13 Stiffness parameters identified from the static test of the super sport fork. 49
Table 14 Modal parameters of the super sport fork without (left) and with (right) the wheel. 49
Table 15 : Calculated radii of curvature 50
Table 16 Modal stiffnesses for inflation pressure of 2 bar (kN/m) 56
Table 17 Measured half length of the contact patch 58
Table 18 Modal parameters of the common modes of the tested bicycles. 63
Table 19 Modal parameters of the forks without the wheel 67
Table 20 Modal parameters of the forks with the wheel 67
Table 21 Inertial parameters for the identification of the forks' stiffness. 69

List of publications

Journals

V.Cossalter, A. Doria, E. Giolo, L. Taraborrelli, M. Massaro, *Identification of the characteristics of motorcycle and scooter tires in the presence of large variations in inflation pressure,* Vehicle System Dynamics: International Journal of Vehicle Mechanics and Mobility, DOI: 10.1080/00423114.2014.940981

V.Cossalter, A. Doria, M. Massaro, L. Taraborrelli, *Experimental and numerical investigation on the motorcycle front frame flexibility and its effect on stability*, Mechanical System and Signal Processing (2015), http://dx.doi.org/10.1016/j.ymssp.2015.02.011

A. Doria, L.Taraborrelli, *Out-of-plane vibrations and relaxation length of the tires for single-track vehicles*, Proceedings of the Institution of Mechanical Engineers, Part D: Journal of Automobile Engineering, DOI: 10.1177/0954407015590703

A. Doria, L.Taraborrelli, *The twist axis of frames with particular application to motorcycles*, Proceedings of the Institution of Mechanical Engineers, Part C: Journal of Mechanical Engineering Science, DOI: 10.1177/0954406215604862

Conferences

A. Doria, L.Taraborrelli, *On the structural vibrations of bicycles: influence of materials and construction technology on the modal properties*, Proceedings, International Cycling Safety Conference 2013, 20-21 November, Helmond, Netherlands

A. Doria, L. Taraborrelli, M. Urbani, *A modal approach for the study of the transient behavior of motorcycle and scooter tires*, Proceedings of the ASME 2014 International Design Engineering Technical Conferences & Computers and Information in Engineering Conference IDETC/CIE 2014 August 17-20, 2014, Buffalo, New York, USA.

A. Doria, L. Taraborrelli, N. Segliani, *The effect of front fork compliance on the stability of bicycles*, Proceedings of the ASME 2015 International Design Engineering Technical Conferences & Computers and Information in Engineering Conference IDETC/CIE 2015 August 2-5, 2015, Boston, Massachusetts, USA.

A. Doria, L. Taraborrelli, *The modal twist axis: a method for describing the dynamical characteristics of single track vehicles*, Proceedings of the ASME 2015 International Design Engineering Technical Conferences & Computers and Information in Engineering Conference IDETC/CIE 2015 August 2-5, 2015, Boston, Massachusetts, USA.

Contents

Abstract 3

Sommario 4

Introduction 5

Chapter 1 – Experimental equipment and methods 10

1.1 The Motostiffmeter 12

1.2 Identification of the static twist axis 13

1.3 Identification of the dynamic twist axis with actuator excitation 14

1.4 Identification of the dynamic (modal) twist axis with hammer excitation 15

1.5 Twist axis and Mozzi axis 17

1.6 Modal analysis 20

1.7 Stiffness decomposition 23

1.8 The Mototiremeter 24

1.9 Tires relaxation length 25

Chapter 2 – Identification of the structural properties of motorcycle frames in static and dynamic conditions 26

2.1 Frame A and Frame B 26

2.2 Frame C 32

Chapter 3 - Identification of the structural properties of motorcycle swing arms in static and dynamic conditions 35

3.1 Swing-arm A 36

3.2 Swing-arm B 37

Chapter 4 - Identification of the structural properties of motorcycle front forks in static and dynamic conditions 40
4.1 Fork A 42
4.2 Development of a modally tuned fork model 46
4.3 Front fork B 48
Chapter 5 – Identification of transient properties of motorcycle tires 50
5.1 Experimental tests 51
5.2 Modal analysis of tires 53
5.3 Stiffness and damping identification 54
5.4 Prediction of relaxation length 56
Chapter 6 – Identification of the static and dynamic properties of bicycles and bicycles components 61
6.1 Modal analysis of bicycles 62
6.2 Modal analysis of the carbon front fork 66
6.3 Modal analysis of the steel front fork 67
6.4 Torsional stiffness and damping identification 68
6.5 Bending stiffness and damping identification 69
6.6 Numerical simulation 71
Chapter 7 – Identification of steady-state properties of wheelchair tires 73
7.1 Experimental tests 73
7.2 Mathematical model 76
7.3 Effect of cornering stiffness 77
7.4 Effect of self-aligning torque stiffness 78
Conclusions 80
Appendix 1 – Tires rigid ring model of a tire 82
Appendix 2 – Steady-state tests of motorcycle tires 83
Appendix 3 – Improved bicycle model 89
References 92
List of captions 94
List of publications 97
Contents 98